

Adaptive optics for extreme ultraviolet lithography : actuator design and validation for deformable mirror concepts

Citation for published version (APA):

Ravensbergen, S. K. (2012). *Adaptive optics for extreme ultraviolet lithography : actuator design and validation for deformable mirror concepts*. [Phd Thesis 1 (Research TU/e / Graduation TU/e), Mechanical Engineering]. Technische Universiteit Eindhoven. <https://doi.org/10.6100/IR732113>

DOI:

[10.6100/IR732113](https://doi.org/10.6100/IR732113)

Document status and date:

Published: 01/01/2012

Document Version:

Publisher's PDF, also known as Version of Record (includes final page, issue and volume numbers)

Please check the document version of this publication:

- A submitted manuscript is the version of the article upon submission and before peer-review. There can be important differences between the submitted version and the official published version of record. People interested in the research are advised to contact the author for the final version of the publication, or visit the DOI to the publisher's website.
- The final author version and the galley proof are versions of the publication after peer review.
- The final published version features the final layout of the paper including the volume, issue and page numbers.

[Link to publication](#)

General rights

Copyright and moral rights for the publications made accessible in the public portal are retained by the authors and/or other copyright owners and it is a condition of accessing publications that users recognise and abide by the legal requirements associated with these rights.

- Users may download and print one copy of any publication from the public portal for the purpose of private study or research.
- You may not further distribute the material or use it for any profit-making activity or commercial gain
- You may freely distribute the URL identifying the publication in the public portal.

If the publication is distributed under the terms of Article 25fa of the Dutch Copyright Act, indicated by the "Taverne" license above, please follow below link for the End User Agreement:

www.tue.nl/taverne

Take down policy

If you believe that this document breaches copyright please contact us at:

openaccess@tue.nl

providing details and we will investigate your claim.

Adaptive Optics for Extreme Ultraviolet Lithography

**Actuator design and validation for deformable mirror
concepts**

This research was financially supported by the *Pieken in de Delta* program of the Dutch Ministry of Economic Affairs.

Adaptive Optics for Extreme Ultraviolet Lithography
by Simon Ravensbergen
Eindhoven: Technische Universiteit Eindhoven, 2012 - Proefschrift

A catalogue record is available from the Eindhoven University of Technology Library.
ISBN: 978-90-386-3133-2
NUR: 978

Typeset by the author using L^AT_EX 2_ε.
Cover design: BOXPress B.V., Oisterwijk, The Netherlands
Reproduction: BOXPress B.V., Oisterwijk, The Netherlands

Copyright © 2012 by S.K. Ravensbergen. All rights reserved.

**Adaptive Optics for Extreme Ultraviolet
Lithography**
**Actuator design and validation for deformable mirror
concepts**

PROEFSCHRIFT

ter verkrijging van de graad van doctor
aan de Technische Universiteit Eindhoven,
op gezag van de rector magnificus, prof.dr.ir. C.J. van Duijn,
voor een commissie aangewezen door het College voor Promoties
in het openbaar te verdedigen
op dinsdag 19 juni 2012 om 16.00 uur

door

Simon Karel Ravensbergen

geboren te Leiden

Dit proefschrift is goedgekeurd door de promotor:

prof.dr.ir. M. Steinbuch

Copromotor:

dr.ir. P.C.J.N. Rosielle

Contents

| | |
|---|-----------|
| Summary | 1 |
| 1 Introduction | 3 |
| 1.1 Adaptive Optics | 3 |
| 1.2 Lithography | 4 |
| 1.3 Optical challenges | 6 |
| 1.4 Thesis contributions and outline | 10 |
| 2 Mirror with one actuator | 11 |
| 2.1 Actuation principle | 11 |
| 2.1.1 Actuator technologies | 12 |
| 2.1.2 Deformable mirror technologies | 13 |
| 2.1.3 Actuator and deformable mirror selection | 16 |
| 2.2 Analytical mirror model | 16 |
| 2.2.1 Actuator model | 16 |
| 2.2.2 Mirror deflection optimization | 18 |
| 2.3 Thermodynamics | 19 |
| 2.3.1 Stored energy | 20 |
| 2.3.2 Conduction and time response | 20 |
| 2.3.3 Steady state heat generation and conduction | 21 |
| 2.3.4 Transient conduction | 22 |
| 2.3.5 Natural convection | 23 |
| 2.4 Realization | 24 |
| 2.4.1 Material selection | 24 |
| 2.5 Validation | 27 |
| 2.5.1 Joule heating | 27 |
| 2.5.2 Practical temperature measurement | 29 |
| 2.6 Conclusion and discussion | 31 |

| | | |
|----------|---|-----------|
| 3 | Mirror with four actuators | 33 |
| 3.1 | Realization | 33 |
| 3.2 | Validation | 38 |
| 3.2.1 | Mirror model | 38 |
| 3.2.2 | Simultaneously heating all actuators | 39 |
| 3.2.3 | Step response of a single actuator | 40 |
| 3.2.4 | Reducing thermal actuator coupling | 46 |
| 3.3 | Conclusion and discussion | 47 |
| 4 | Mirror with axial actuators | 49 |
| 4.1 | Actuation principle | 49 |
| 4.2 | Analytical mirror model | 51 |
| 4.2.1 | Thickness balance between mirror and back-plate | 51 |
| 4.2.2 | Selecting mirror and actuator dimensions | 54 |
| 4.3 | Realization | 54 |
| 4.3.1 | DM with 7 actuators | 55 |
| 4.3.2 | DM with 19 actuators | 57 |
| 4.4 | Validation | 59 |
| 4.4.1 | DM with 7 actuators | 60 |
| 4.4.2 | DM with 19 actuators | 61 |
| 4.5 | Conclusion and discussion | 67 |
| 5 | Conclusions and recommendations | 69 |
| 5.1 | Conclusions | 70 |
| 5.1.1 | Bending moment deformable mirrors | 70 |
| 5.1.2 | Deformable mirrors with axial actuators | 71 |
| 5.1.3 | Comparison | 71 |
| 5.2 | Recommendations | 72 |
| 5.2.1 | Vacuum compatibility | 72 |
| 5.2.2 | Thermal sensitivity | 72 |
| A | Material properties | 73 |
| B | Joule heating | 77 |
| C | Finite element analysis using ANSYS | 79 |
| | Bibliography | 81 |
| | Nomenclature | 87 |
| | Glossary | 89 |
| | Dankwoord | 91 |
| | Curriculum Vitae | 93 |

Summary

Adaptive Optics for Extreme Ultraviolet Lithography

In the production of integrated circuits (e.g. computer chips), optical lithography is used to transfer a pattern onto a semiconductor substrate (wafer). For lithographic systems using light in the ultraviolet band (EUV) with a 13.5 nm wavelength, only reflective optics with multi-layers can reflect that light by means of interlayer interference, but these mirrors absorb around 30% of the incident light. Depending on pattern and beam shape, there is a nonuniform light distribution over the surface of the mirrors. This causes temperature gradients and therefore local deformations, due to different thermal expansions. To improve the throughput (wafers per hour), there is a demand to increase the source power, that will increase these deformations even further. Active mirrors are a solution to correct these deformations by reshaping the surface.

This thesis addresses the challenges to accurately deform a mirror with high repeatability, meeting the requirements for implementation in a lithographic illumination machine. The main design criteria are vacuum compatibility, actuator stroke and the distance between actuators. Four different experimental mirrors, with increasing complexity, are successfully designed, realized and validated. All mirrors are equipped with thermo-mechanical actuators to either bend, or axially deform them. These actuators are free from mechanical hysteresis and therefore have a high position resolution with high reproducibility. Extensive finite element analysis is done, to maximize actuator stroke and minimize input power. All mirrors are tested and validated with interferometer surface measurements and thermocouple temperature measurements.

The first experimental mirror with one thermo-mechanical bending actuator is successfully built and tested (chapter 2). To obtain a high mirror deflection at a given inserted actuator power, aluminum is chosen as the actuator material. The mirror is made from Zerodur® like the mirrors in the first EUV lithographic demonstration machines. A mirror deformation of $4.7 \text{ nm}/^\circ\text{C}$ is achieved, where the inserted actuator power is $0.044 \text{ }^\circ\text{C}/\text{mW}$, meaning $0.21 \text{ nm}/\text{mW}$. The measured characteristic time constant

is 10 s, meaning that for a given input, 63% of the steady state stroke is reached within that time scale. All values are close to the predicted ones from the models and also meet the requirements for implementation.

To further investigate the concept and to measure the mechanical and thermal actuator coupling, an experimental mirror with four actuators is designed, developed and validated (chapter 3). It is an extension of the mirror with one actuator. In a single actuator step-response, a mirror deflection of $3.4 \text{ nm}/\text{C}$ is achieved. A design optimization is proposed and successfully tested which reduces the actuator coupling from 30% to 10%, while the mirror deflection at the same input is reduced to 55%. Actuator speed is demonstrated while simultaneously heating all actuators with 3 mW, which correspond with a mirror deformation of $33 \text{ pm}/\text{s}$. When using an adaptive mirror in an EUV lithography system, actuator strokes of $1 \text{ nm}/\text{min}$ are required. The demonstrated actuator speed of $33 \text{ pm}/\text{s} = 2 \text{ nm}/\text{min}$ meets that requirement.

The third and fourth mirror have actuators placed perpendicular to the surface (chapter 4). By placing the actuators on a thin back plate, the force loop is localized and therefore a lower actuator coupling is achieved. The results obtained from the third mirror with 7 actuators are close to the predicted values from the static and thermal models. Based on these good results, this actuation principle is implemented in a smaller deformable mirror with 19 actuators inside a 25 mm beam diameter. A linear relation between actuator power and temperature of $0.190 \text{ }^\circ\text{C}/\text{mW}$ and between power and averaged inter-actuator stroke of $0.13 \text{ nm}/\text{mW}$ is achieved. So, the successfully realized mirror deflection is $0.68 \text{ nm}/\text{C}$ and no hysteresis is observed. For both mirrors a support frame is developed, that minimizes introduced surface deformations by temperature variations.

Thermal step responses are fitted and both heating and cooling characteristic time constants are 2.5 s. The thermal actuator coupling from an energized actuator to its direct neighbor is 6.0, to their neighbors it is 1.3%. The total actuator coupling is approximated around 10%, based on the good agreement between simulated and measured inter-actuator stroke.

Finally, chapter 5 summarizes the main findings from the different deformable mirrors and compares them. Also, suggestions for future research are given for implementation into a lithographic machine.

Introduction

The field of adaptive optics (AO) is briefly introduced with its relevance for astronomy. Also, lithography is introduced and the need for a dedicated adaptive mirror system is discussed. The challenges and specifications for such a system are described. Finally, an overview of this thesis is given.

1.1 Adaptive Optics

Adaptive optics (AO) is a technology used to improve the performance of optical systems by compensating wavefront distortions [34, 63, 72]. Its first developments were made in astronomy and was first proposed by Babcock (1953) [17] and later by Linnick (1957) [46]. It became practically applicable after the advances in computer technology in the 1990s. Figure 1.1 gives the basic principle of an AO system. In astronomy, the earth atmosphere limits the resolution of ground based telescopes through its properties of turbulence, absorption and dispersion. The low resolution of the scientific image is a result of wavefront distortions that are mainly caused by turbulence. Moving air bubbles of slightly different temperature and pressure are continually changing the refractive index of the air layer above the telescope. Images are improved by compensating this effect with a deformable mirror (DM). A wavefront sensor (WFS) measures the distortions and a (real-time) control systems translates this to an optimal shape of the DM. The shape is imposed by actuators which are placed in a grid behind the mirror. In general: the more actuators, the better the shape and thus the lower the residual error in the wavefront. However with a relative low number of actuators (in the order of 10), already 90% of the distortion can be corrected [72]. Nowadays, almost all large telescopes are equipped with an AO system [35, 50].

Within adaptive optics for astronomy, there is a research branch that focuses on active mirrors for a special wavelength of light: X-ray [16, 27, 61]. X-ray wavelength is subdivided into soft X-ray (10 nm \rightarrow 100 pm, 0.124 \rightarrow 12.4 keV) and hard X-ray (100 \rightarrow 10 pm, 12 \rightarrow 120 keV). There are plans to build a space born telescope with this technology [39–42, 57].

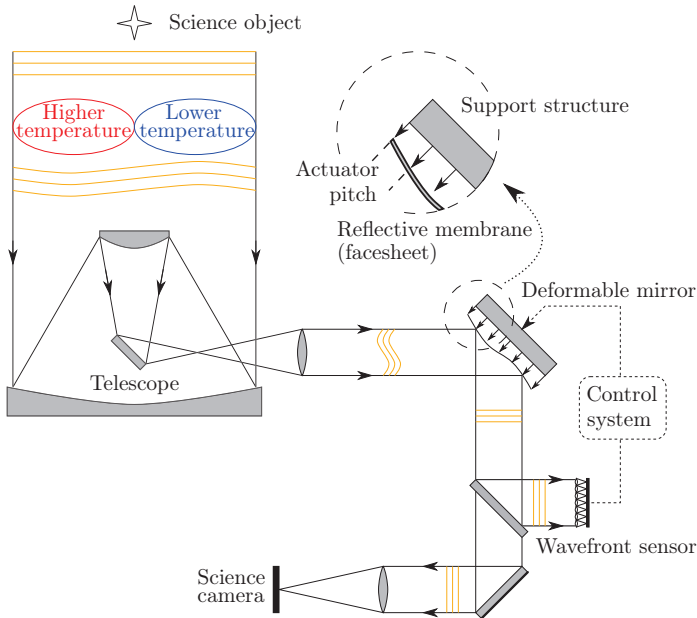


Figure 1.1 / Basic principle of an adaptive optics system. Light from a science object distorted by the earth atmosphere enters a telescope. The distortion is measured with a wavefront sensor and is compensated by a deformable mirror.

1.2 Lithography

Optical lithography is at first sight a totally different technology compared to adaptive optics for astronomy. It is a technology that has enabled mass production of integrated circuits (IC) [19, 44, 48]. Nowadays IC's are used in almost all electrical devices and equipment (e.g., computers, cell phones and other digital appliances) due to their low production cost. Growth in the semiconductor industry is characterized by Moore's law: He predicted [54] in 1965 that the number of transistors in an IC doubles approximately every two years¹. This trend has continued for more than half a century and is expected to continue until at least 2015 or 2020. The law is used by the semiconductor industry to guide long-term planning and to set targets for research and development [1].

In optical lithography (or photolithography), light transfers a geometric pattern from an image (mask) to a light sensitive chemical layer (resist) on a semiconductor substrate (silicon wafer). By far the most common method of exposure is projection printing, where an image is projected by a lens system. Projection is done by either *scanning* a

¹Although originally calculated as a doubling every year, Moore later refined the period to two years [55].

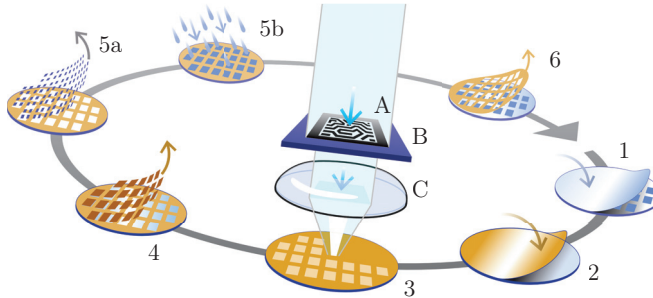


Figure 1.2 / Basic principle of optical lithography: (1) deposition = adding a new layer of silicon or other material over the wafer, (2) photoresist coating, (3) exposure = pattern the resist: an image (A) on a reticle (B) is projected onto the wafer by a lens system (C), (4) developing = leaving the chip pattern as a mask on the surface of the wafer, (5a) etching = remove or add material, (5b) implantation = dope the material with contaminants that change the conductive properties of the semiconductor, (6) ashing = removing the resist mask. The figure is a reproduction from [3].

slit of light from the mask onto the wafer or by *stepping*, where one rectangular section is exposed at a time. A hybrid *step-and-scan* approach uses a fraction of a normal stepper field and scans it in one direction. The wafer is then stepped to a new location and the scan is repeated. After exposure, a series of chemical treatments then either engraves the exposure pattern into the material underneath the photo resist, or enables material deposition in the desired pattern upon it. Figure 1.2 shows a schematic overview of the different steps. A modern semiconductor wafer will go up to 35 times [19, p. 601] through this lithographic cycle.

Optical lithography was, and will continue to be, vital in semiconductor growth and profits improvement. The smallest printable feature (resolution or Critical Dimension) is determined by the wavelength (λ) and the numerical aperture (NA) of the projection system. It is given by the Rayleigh resolution equation [44, p. 17]:

$$CD = k_1 \frac{\lambda}{NA} \quad (1.1)$$

where k_1 is an imaging process dependent scaling factor. For reduction in feature size, the wavelength progressed from blue (436 nm) to UV (365 nm) to deep-UV (248 nm) to today's (193 nm) [48]. Meanwhile the projection tool numerical aperture has risen from 0.16 (first scanner) to 0.93 for features below 100 nm. The use of water as medium between lens and wafer (immersion) enables an NA of 1.35 [56]. Next step is a further reduction of the wavelength to Extreme Ultra Violet (EUV): 13.5 nm. This wavelength is close to X-ray (below 10 nm) and it is absorbed by all materials including traditional transmissive lens materials and air. Only reflective optics (mirrors) are a practical option for beam shaping in the EUV case. These are covered with a coating with up to 100 alternating layers of Molybdenum and Silicon. Typical reflectivity is $\simeq 70\%$, the

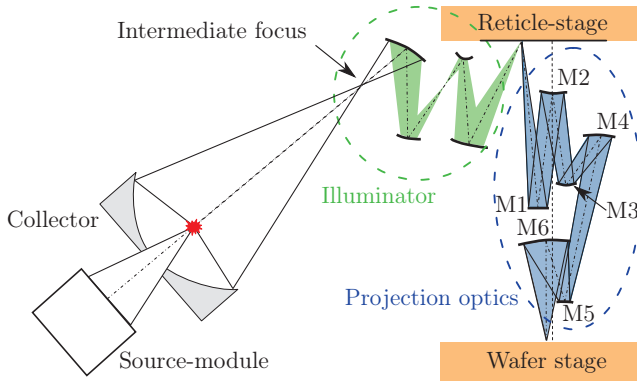


Figure 1.3 / Schematic drawing of an EUV lithography machine with its five major components [74]: source (laser and collector), illuminator (intermediate focus and shaping optics), reticle stage (with the mask), the projection optics (with its six mirrors $M1 \dots M6$) and the wafer stage.

rest of the light is absorbed and converted into heat. Resolution enhancement is also made via off-axis illumination (reducing the factor k_1) [51]. To be competitive with the immersion technology, the EUV technology has to overcome three major challenges [73]:

- resist [58]: sensitivity (dose) [49] and secondary electron exposure (resist blur) [29] are limiting the wafer throughput and resolution.
- source [76]: the power is too low to reach in acceptable time the resist dose to achieve the desired throughput. Also the intensity is fluctuating out of specification [22]. The collector lifetime is limited due to contamination by debris from the source. Trade off is made between amount of light collected and source distance [21]. Collector mirrors are water cooled to manage the heat load.
- optics [47]: contamination of mirrors, wafer and mask. Debris from the source and contaminated vacuum reduce the lifetime and increase the risk of defects. Mirrors used to transfer the pattern from mask onto wafer are kept at a constant temperature ($0.001^\circ\text{C}/\text{h}$) to minimize thermal drift [45]. These mirrors are magnetically suspended to suppress vibrations. The multilayer coating is optimized for maximal reflectivity and minimal stray light (called flare).

1.3 Optical challenges

EUV light is absorbed by air, so a large part of the lithography machine must be maintained in an ultra clean vacuum environment, including the light source, projection optics and wafer. This requires a fundamental redesign of current wafer scanner

equipment. Only a limited number of materials is suitable for use in vacuum [14], since contamination (e.g., outgassing, dust particles) must be avoided [71]. Special care must be taken in the usage of plastics, elastomer's and fluids (also lubricants) [31]. Almost all types of insulated wire, paint and tape have high outgassing rates [13]. Screws should be drilled or relieved (i.e., file off one side of the threaded area.) to prevent virtual leaks.

Mirror heating

Mirror heating will play a significant role in EUV systems [38, 68] in the near future, due to the increasing source power. This is shown below with a short calculation. In vacuum the only physical form of transporting heat is by radiation, since there are no atoms and/or molecules for the other two mechanisms: conduction and convection [53]. There is a difference in the temperature dependency of conduction and convection on one hand, and radiation on the other. For the majority of conduction applications, heat transfer is described by the Fourier's law:

$$q_x'' = -k \frac{\partial T}{\partial x}, \quad (1.2)$$

where q_x is the conducted heat flux² in the x -direction, T is the temperature and k is the thermal conductivity. Similarly, convective heat flux is:

$$q'' = \hbar (T - T_\infty), \quad (1.3)$$

where \hbar is the convective heat transfer coefficient and T_∞ is a reference temperature. In general k and h are assumed to be constant for most applications, so heat transfer rates are almost linearly proportional to temperature differences. Radiation heat transfer is proportional to differences in temperature to the fourth power:

$$q'' \propto T^4 - T_\infty^4. \quad (1.4)$$

Now, assume that an EUV mirror is cooled by radiation using a colder back structure with a perfect view-factor of 1. The radiation heat transfer per unit area reads:

$$q'' = \epsilon \sigma (T_1^4 - T_2^4) = 63.5 \text{ W/m}^2$$

with emittance $\epsilon = 0.8 [-]$, Stefan-Boltzmann constant $\sigma = 5.67 \times 10^{-8} \text{ W/m}^2\text{K}^4$, ambient temperature $T_1 = 20 + 273.15 \text{ K}$ and cooling temperature $T_2 = 5 + 273.15 \text{ K}$. In a few

²Heat flux is the flow of energy per unit time and per unit area, heat flow is energy per unit time.

years, sources will deliver an average light intensity after the mask of 10 W [22, 76]. Mirrors have a typical reflectivity a few percent below the theoretical limit of 0.72 (at $\lambda = 13.5$ nm), so the absorption factor is at least 0.28. Using this input values, the cooling limit via radiation for each mirror is approximated and shown in table 1.1. Comparing the absorption for each mirror with its radiative cooling ability, the small

Table 1.1 / Mirror radiation

| | area [m ²] | reflection [W] | absorption [W] | cooling [W] |
|----|------------------------|----------------|----------------|-------------|
| M1 | 0.070 | 7.2 | 2.8 | 4.4 |
| M2 | 0.013 | 5.2 | 2.0 | <i>0.83</i> |
| M3 | 0.0042 | 3.7 | 1.5 | <i>0.27</i> |
| M4 | 0.043 | 2.7 | 1.0 | 2.7 |
| M5 | 0.0024 | 1.9 | 0.75 | <i>0.15</i> |
| M6 | 0.027 | 1.4 | 0.54 | 1.7 |

mirrors (M2, M3 and M5) are unstable (i.e. more heat is absorbed than can be radiated). So with this boundary conditions, the mirror temperature (T_1) will increase to reach steady state at a larger temperature difference.

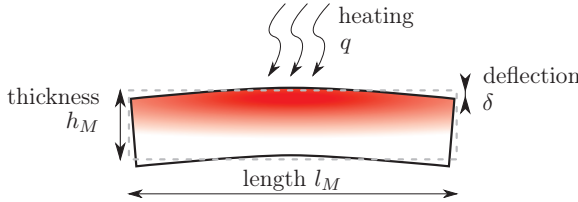


Figure 1.4 / One dimensional quilting due and uniform heat load.

Mirror quilting

Mirror heating causes a temperature difference between front and back mirror surface that is given by (1.2). For most materials this thermal gradient causes out of plane bending, since the length changes with temperature by:

$$\Delta l_M = \alpha l_0 \Delta T. \quad (1.5)$$

Here, α is the linear expansion coefficient, l_0 the initial length and ΔT the temperature difference between initial and current state. This quilting behavior is shown in figure 1.4. Based on the radius of curvature, the deflection reads:

$$\delta = \frac{l_{M,0} \cdot \Delta l_M}{8h_M} \quad (1.6)$$

Table 1.2 / Requirements of an active mirror for extreme ultraviolet lithography, formulated by ASML.

| | |
|------------------------------|---|
| actuator spacing | ≈ 20 mm (also called spatial frequency) |
| actuator stroke | 1 nm over 1 min, 5 nm over 1 h, 10 nm over lifetime (7 y) |
| mechanical actuator coupling | typically 10-15 % |
| actuator hysteresis | < 5 % at full stroke |
| environment temperature | 22 °C (295.15 K) at vacuum |
| temperature gradient | 0.001 °C/h |
| mirror suspension | magnetically levitated out of plane stiffness = 100 N/m and in plane = 1000 N/m. |

To minimize bending, EUV mirrors are made from Ultra Low Expansion (ULE) glass. This material has zero expansion around a specific temperature: the zero crossing temperature (ZCT), see appendix A for further explanation. In the ULE fabrication process, this ZCT can be tuned with an uncertainty around one degree. So globally, the mirror quilting is minimized by selecting the best ZCT based on the mirror specific heat load. Locally however, still some uncontrollable mirror deformation exist, mainly due to nonuniform light intensity over the surface. This causes local distortions on the image, and are summed toward a limitation in the resolution of the complete mirror system.

These deformations can be compensated by locally adjusting the shape of one (or more) mirrors. Such a mirror then adapts its surface to minimize the influence of the heat load. It can also be used to relax the current fabrication tolerances and adapt the manufactured shape toward the designed one. A research collaboration is formed³ to develop new Adaptive Optics technology for future lithographic EUV projection systems. This is performed in detail on:

- overall system design,
- control methodology,
- metrology and
- active mirror methodology.

The main driver in that collaboration is ASML, a Dutch company and the largest supplier in the world of photo lithography systems for the semiconductor industry. Based on their knowledge, demands on a future active EUV mirror are formulated and given in table 1.2. The actuator spacing is based on the desired spatial frequency and the total number of actuators. Actuator stroke is coupled to the deformation caused by worst case nonuniform mirror heating. The mechanical actuator coupling is common in conventional deformable mirrors for astronomy. An actuator hysteresis below 5%

³This research is supported by the Dutch Ministry of Economic Affairs and the Provinces of Noord-Brabant and Limburg in the *Pieken in de Delta* program.

is controllable with low effort on control input. The mirror environment in vacuum is maintained as constant as possible with an gradient of 1 mK/h .

1.4 Thesis contributions and outline

This thesis focuses on

accurate deformation of an EUV mirror with high repeatability, meeting the requirements for implementation in a lithographic machine.

Four different experimental mirrors, with increasing complexity, are designed, realized and validated. All take the specifications of table 1.2 into account. With these mirrors feasibility of an adaptive EUV mirror is demonstrated. Measurements are performed to check the designed specifications.

This thesis is organized as follows. In the next chapter various actuator technologies are discussed and the choice for a thermo mechanical actuator is explained. An experimental mirror with one actuator is modeled, designed and characterized. A deformable mirror with four actuators is explained in chapter 3. This mirror uses the technology and knowledge of the one actuator mirror. Here the mechanical and thermal coupling between adjacent actuators is characterized. A different implementation of a thermo mechanical actuator is introduced in chapter 4 with two mirror realizations, one with seven and one with 19 actuators. Chapter 5 reflects on the specifications and gives recommendations for further technology implementation in EUV lithography.

Mirror with one actuator

In this chapter various actuator technologies are discussed and the choice for a thermo mechanical actuator is explained. An experimental mirror with one actuator is modeled, designed and characterized. This characterization is done with both temperature measurements and interferometer surface measurements. At the end, a conclusion is given with an summary of the specifications.

2.1 Actuation principle

In general, deformable mirrors in adaptive optics are separated in segmented and continuous facesheet mirrors, see figure 2.1. Since mirrors for EUV lithography

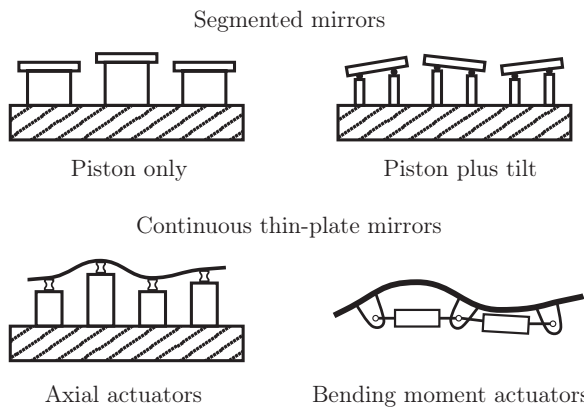


Figure 2.1 / Types of wavefront correctors, adapted from [26]

have continuous mirror surfaces with strict specifications on figure shape and surface roughness, only actuation by axial or bending moment actuators is considered. A brief description of the two principles for actuation of continuous thin-plate mirrors is given below.

- Axial actuators
 - Deformation produced by forces normal to the plate, so a reference body is needed to support and align the actuators. Unflatness and variation in actuator length are copied to the mirror surface.
 - Mirror itself can be made less sensitive to dimensional changes by matching the materials used and by a statically determined design.
 - Spatial frequency (= spacing between actuators) is limited by the stiffness combination of mirror plate, actuator and reference body.
- Bending moment actuators
 - Deformation produced by forces within the plate, so no need for a reference back structure.
 - Sensitive to dimensional changes: temperature variations and aging.
 - Can not produce all surface shapes without the use of edge actuators.
 - Spatial frequency is limited due to thickness changes in a double layer configuration: mirror as top layer with actuator zones underneath. As a rule of thumb: bending is dominant when the controlling zones are larger than the mirror thickness.
 - Spatial frequency is increased by placing the actuators at a given distance under the mirror, resulting in a larger output stroke and smaller spatial influence.

2.1.1 Actuator technologies

In precision mechatronics a large variety of actuators is available. Below, a short introduction of the major technologies is given, based on [28] and [34]. Depending on the application, the given characteristics are an advantage or a disadvantage.

- Piezoelectric
 - Suffer from drift and hysteresis (typically 5 – 10%).
 - High bandwidth: > 2 kHz possible (requiring also a high bandwidth measurement to close the loop).
 - Large voltage (≥ 100 V) control
 - Sensitive to EMI (electromagnetic interference).
- Voice coil/ reluctance
 - (Almost) linear behavior between input and output, low drift and hysteresis.
 - High efficiency in converting electrical energy into mechanical work.
 - High bandwidth: > 2 kHz possible (requiring also a high bandwidth measurement to close the loop).
 - Magnets are affected by aging.

- Electrostatic
 - High voltage control.
 - Small forces at low current consumption.
- Phase change
 - Depending on the material, the phase change is induced electrically, thermally or ultrasonic.
 - High force and stroke possible [69].
- Shape memory alloy
 - External force needed for the return stroke.
 - Combination with elasticity of the material possible.
- Magnetostrictive
 - Hysteresis and nonlinear behavior.
 - High voltage control.
 - Sensitive to EMI.
- Thermo-mechanical
 - (Almost) linear behavior between input and output, low drift and hysteresis.
 - Low bandwidth: ~ 1 Hz.
 - Thermal coupling with other components.

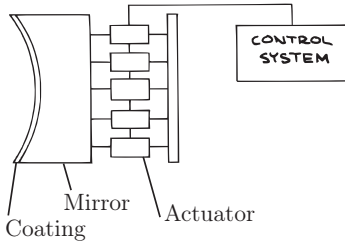
2.1.2 Deformable mirror technologies

This section gives a brief overview on DM technologies that could be applied in an EUV lithography system.

Figure 2.2 shows a selection of patents claiming deformable mirrors based on axial actuators. All sub figures are given as: US patent number, assignee name, patent title and main figure. The most relevant patent is shown in Fig. 2.2(a), where a thin back-plate is used to couple the piezoelectric actuators. As described in section 4.1, the research is continued mainly due to the age of this patent (it is filed on June 15, 1998).

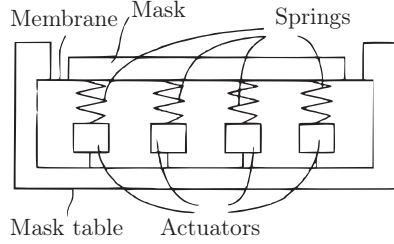
Figure 2.3 shows a selection of patents claiming deformable mirrors based on bending moment actuators. The most relevant patent is shown in Fig. 2.3(b), where also is claimed that actuators are placed between mirror posts. Since ASML is the assignee of this patent, it is decided to continue research on the feasibility and application. New features are claimed in patent NL-2004753 [64].

US5986795
 Chapman and Sweeney
 DM with piezoelectric actuators



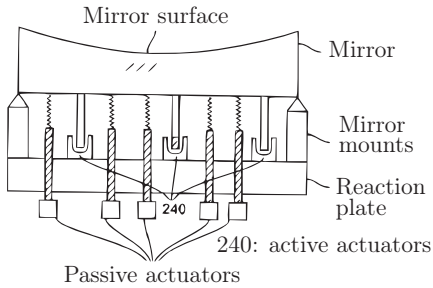
(a)

US2001 – 026358
 ASML
 Reticle or mask as membrane mirror with force actuators



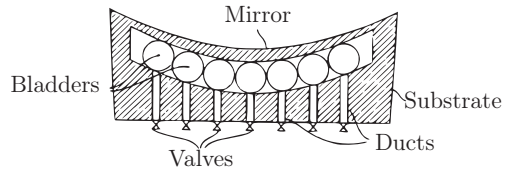
(b)

US2004 – 027632
 Nikon
 DM with active and passive actuators



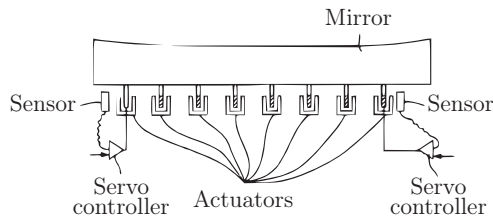
(c)

US2004 – 036940
 Nikon
 DM with air-pressure actuators



(d)

US2004 – 017623
 Nikon
 DM with voice-coil actuators



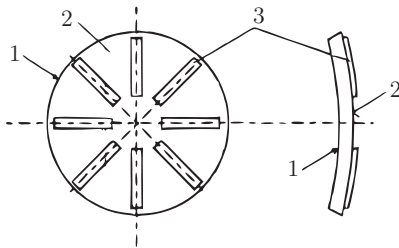
(e)

Figure 2.2 / Patent overview of deformable mirrors with axial actuators.

US2002 – 048096

Zeiss

Reticle or mask as membrane mirror with force actuators



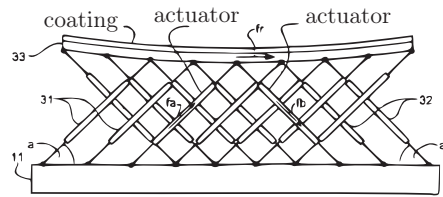
1: mirror, 2: rear side, 3: piezoelectric elements

(a)

US2002 – 011573

ASML

Various bending strategies using a back structure



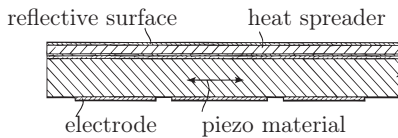
11: base plate, 31+32: actuators

(b)

US2008 – 037146

BAE Systems

Piezo actuation with heat spreader

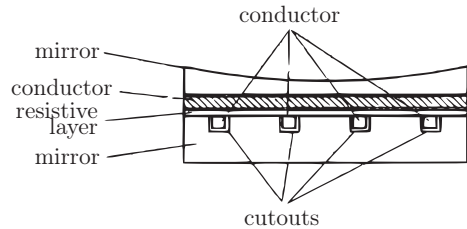


(c)

US2010 – 0201958

Zeiss

Mirror with integrated heating wires/ pads to influence the temperature



(d)

Figure 2.3 / Patent overview of deformable mirrors with bending moment actuators.

2.1.3 Actuator and deformable mirror selection

Initially, axial actuators are rejected due to the need for a support structure. Undesirably, this reference body will at least double the magnetically suspended mirror mass. The potentially larger spatial frequency of bending moment compared to axial actuators seems acceptable with respect to the specifications of table 1.2. In chapter 4, axial actuators are reconsidered using an innovative stiffness combination of mirror plate, actuator and reference body. Most technologies require wires between the actuators and a support structure. The consequence of that mechanical coupling is a undesirable reduction in vibration isolation. This holds for the piezoelectric, magnetostrictive, electrostatic and voice coil/ reluctance actuators. Actuation using shape memory alloys require a separate technology for the return stroke. Examining all above stated specifications, thermo-mechanical actuation is selected as principle due to:

- its harmonization with the active mirror requirements of 1 nm over 1 min,
- its possibility for contact-less heating using a laser,
- its possibility for low power consumption by for example, reducing the heat leakage into the mirror,
- its linear behavior and low hysteresis.

2.2 Analytical mirror model

An analytical model is derived for a single bending moment actuator to optimize mirror deflection. Investigated design variables are: actuator size, placement and material. This model enhances insight during the optimization process and enables shorter calculation times compared to Finite Element Analyzes (FEA). Promising parameter combinations are recalculated using FEA (see Fig. 2.15). The analytical model consist of a rectangular mirror section that is extended at the bottom with two posts, see figure 2.4. Between the posts a cylindrical actuator is placed. The parameters of the realized deformable mirror are given in table 2.2. The mirror deflection δ is defined as the displacement from an initial to an actuated shape, and is measured between the centers of two adjacent posts. In this model only the thermal elongation of the actuator material is taken into account.

2.2.1 Actuator model

The actuator elongation is a combination of the thermal elongation and the axial compression:

$$\Delta l_A = \alpha_A \Delta T l_0 - \frac{F l_{A,0}}{E_A A_A} \quad (2.1)$$

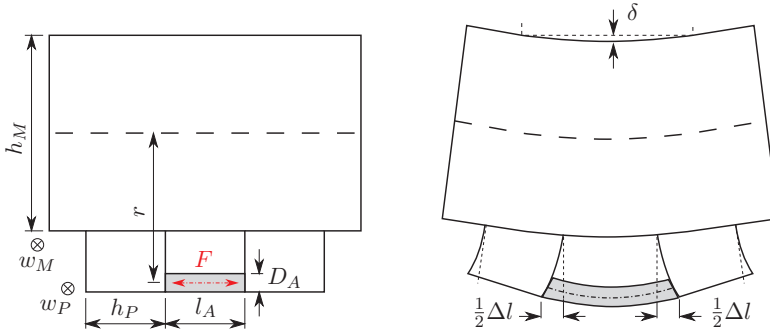


Figure 2.4 / Model of a thermo-mechanical actuator between posts, placed below a mirror. The distance between the neutral axis of the mirror and the actuator center is r . The subscript \subscript_M is assigned to the mirror, \subscript_A to the actuator and \subscript_P to the posts. The symbols used are: thickness h , width w , length l , diameter D and mirror deflection δ .

with thermal expansion coefficient α , temperature difference ΔT , force F , Young's modulus E and cross sectional area $A_A = \frac{1}{4}\pi D_A^2$. The elongation is maximal ($\Delta l_A = \alpha_A \Delta T l_0$) when no force is generated, whereas maximal force ($F_{max} = \alpha_A \Delta T \cdot E_A A_A$) is reached at $\Delta l_A = 0$. Since the displacements are small (in the order of nm) compared to the actuator and mirror dimensions (cm), a linear approximation is made. The mirror deflection due to the actuator force is defined as a linear summation of the different displacements, as shown in figure 2.5.

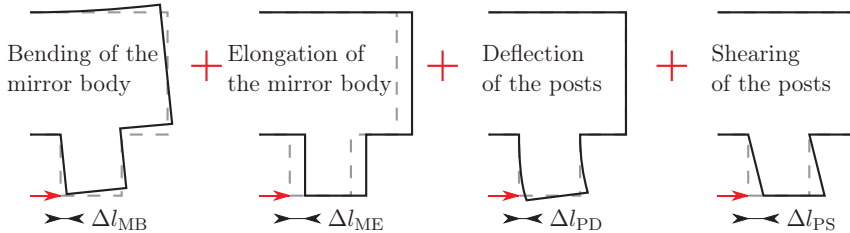


Figure 2.5 / Linear summation of the different displacements.

$$\begin{aligned}
 \Delta l_M &= 2(\Delta l_{MB} + \Delta l_{ME} + \Delta l_{PD} + \Delta l_{PS}) \\
 &= 2\left(\frac{Fr^2(l_A + h_P)}{2E_M I_M} + \frac{F(l_A + h_P)}{2E_M A_M} + \frac{F(r - h_M/2)^3}{3E_M I_P} \right. \\
 &\quad \left. + \frac{2F(1 + \nu_M)}{E_M A_P}(r - h_M/2)\right) \tag{2.2}
 \end{aligned}$$

The force is calculated from the equilibrium between actuator elongation and mirror displacement ($\Delta l_A = \Delta l_M$). Using this solution, the central deflection of the mirror can

be determined as function of the actuator force:

$$\delta = \frac{Ml^2}{2EI} = \frac{F \cdot r \left(\frac{1}{2} (l_A + h_P) \right)^2}{2E_M I_M} \quad (2.3)$$

2.2.2 Mirror deflection optimization

The relation of the deflection as function of r (distance between the neutral axis and the actuator) and h_M (mirror thickness), is given in figure 2.6. The other parameters from table 2.2 are constant. The dotted line is the optimal actuator distance r_{opt} as function of the thickness. An efficiency is derived by comparing the deflection δ at optimal position r_{opt} with the actuator placement at the bottom surface ($r = h/2$). Figure 2.7 shows this efficiency as function of the mirror thickness. An identical actuator below for example an $h = 20$ mm thick mirror at r_{opt} , gives $\sim 43\%$ more mirror deflection than placed at $r = h/2$.

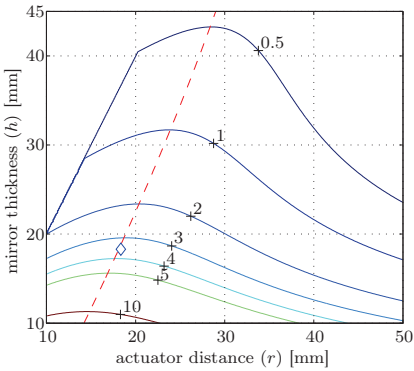


Figure 2.6 / Mirror deflection $\delta/\Delta T$ as function of the distance between actuator and neutral axis r and as function of the mirror thickness h . Also r_{opt} as function of h (dashed).

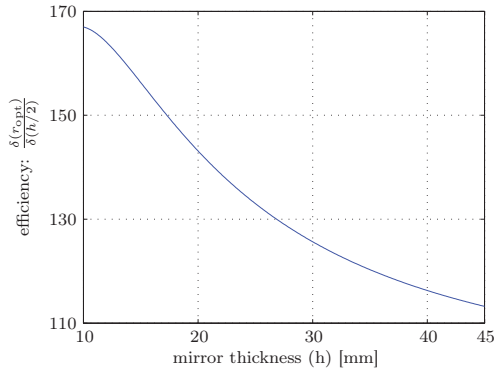


Figure 2.7 / Efficiency of optimal actuator placement (r_{opt}) with respect to a surface mount actuator as function of the mirror thickness.

Further insight is obtained by using a shape factor Υ . Both the thickness of the posts and the actuator length, are defined as the mirror thickness divided by the shape factor: $h_P = l_M = h_M/\Upsilon$. Increasing this factor results in a decrease of the actuator pitch, meaning lowering the distance between adjacent actuators. In figure 2.8 the deflection δ is plotted as function of the shape factor Υ and as function of the actuator distance r . A rise in actuator pitch increases both the mirror deflection and the optimal actuator distance.

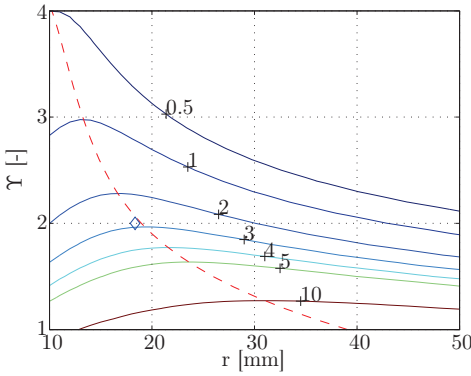


Figure 2.8 / Mirror deflection δ as function of shape factor (Υ) and as function of actuator distance (r), dotted line is r_{opt} .

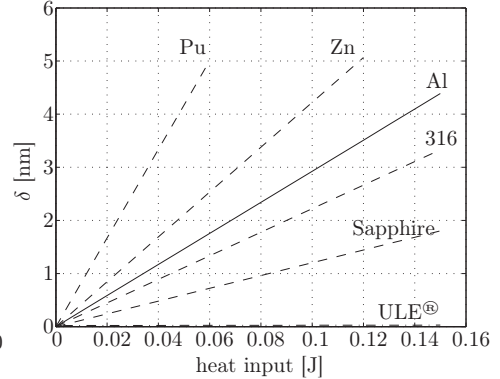


Figure 2.9 / Mirror deflection δ as function of actuator heating for different materials: plutonium (Pu), zinc (Zn), aluminum (Al), stainless steel (316), sapphire and Ultra Low Expansion[®] glass.

Materials other than aluminum are investigated to maximize the deflection of the mirror with minimal heat input. In figure 2.9 the deflection as function of inserted heat is given for different materials.

2.3 Thermodynamics

Some thermal models are derived to obtain more insight in the temperature behavior of the mirror with one actuator. The general energy equation for unsteady heat conduction in one dimension with internal heat generation reads

$$\frac{\partial^2 T(t, x)}{\partial x^2} + \frac{q'''}{k} = \frac{\rho c_p}{k} \frac{\partial T(t, x)}{\partial t} \quad (2.4)$$

Using: temperature T [K], one dimensional position x [m], heat flow rate per volume q''' [W/m^3], thermal conductivity k [$\text{W}/\text{m K}$], density ρ [kg/m^3], specific heat capacity c_p [$\text{J}/\text{kg K}$] and time t [s]. In the next subsections, these analytically solvable cases are analyzed:

1. Stored energy.
2. Conduction and time response.
3. Steady state heating: heat conduction to the mirror, heat distribution within the actuator.
4. Transient behavior of an instantaneous contact between a heated actuator and the mirror.

These cases are based on a one dimensional model that is shown in figure 2.10.

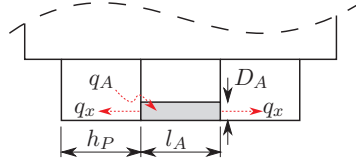


Figure 2.10 / Thermal model of the mirror with one single actuator.

2.3.1 Stored energy

The energy stored in an actuator, based on its temperature difference is given by

$$q_A = \rho_A V_A c_{p,A} \frac{dT_A}{dt}, \quad (2.5)$$

assuming complete isolation and an uniform temperature distribution. This is a derivation of (2.4), using $\frac{\partial^2 T}{\partial x^2} = 0$ and the heat per actuator volume $q''' = \frac{q_A}{V_A}$.

2.3.2 Conduction and time response

Fourier's law (eq. 1.2) defines the heat transferred from the actuator into the mirror via conduction:

$$q_x = -k_M A_P \frac{dT}{dx}. \quad (2.6)$$

To approximate for example, the temperature decrease after switching off the actuator heating, $q_x = q_A$ is solved, using (2.5). So, the energy stored in the actuator is conducted into the mirror. Assuming a constant temperature gradient inside the mirror, the x -position in the mirror where $T(t) = T_\infty$ is approximated as a constant l_M . The resulting actuator temperature behavior is:

$$T_A(t) = T_\infty + T_{A,0} \exp\left(-\frac{k_M A_P}{l_M \rho_M V_A c_{p,A}} t\right). \quad (2.7)$$

The term in the exponent is the characteristic time constant, and is defined as:

$$\tau = \rho V c_p \cdot \sum_i \frac{\Delta x_i}{k_i A_i} = \text{lumped thermal capacitance} \cdot \text{thermal resistance} \quad (2.8)$$

and the half-time as $t_{1/2} = \tau \ln 2$.

Note that the conduction model presented above, is based on perfect thermal contact between the surfaces. In reality a difficult to characterize thermal contact resistance occurs at the interfaces (e.g., due to roughness). This results in an extra insulation that increases the thermal time constant.

2.3.3 Steady state heat generation and conduction

Figure 2.11 shows a half-sided actuator in perfect thermal contact with the mirror [37, p. 47]. Here, the assumptions are made that there is no transfer of heat to the surroundings and that there is a constant depth of penetration l_M into the mirror. In

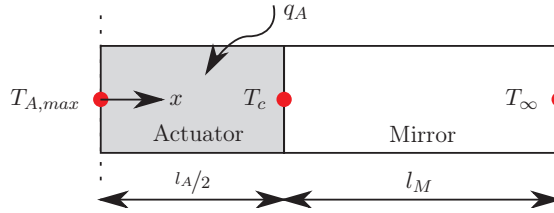


Figure 2.11 / Actuator with internal heat generation q_A , coupled to the mirror. Boundary conditions are the interface temperature T_c and ambient temperature T_∞ .

steady state the time dependency in the differential equation (2.4) is zero. The resulting relation as function of position including heat generation reads

$$\frac{d^2T(x)}{dx^2} + \frac{q_A}{k_A V_A} = 0. \quad (2.9)$$

This gives for the actuator temperature:

$$T_A(x) = \frac{q_A l_A^2}{8V_A k_A} \left(1 - \frac{x^2}{(l_A/2)^2}\right) + T_c \quad (2.10)$$

using boundaries:

$$T(x = l_A/2) = T_c \quad \text{and} \quad \left. \frac{dT}{dx} \right|_{x=0} = 0.$$

The mirror temperature is:

$$T_M = \frac{T_\infty - T_c}{l_M} (x - l_A/2) + T_c \quad (2.11)$$

with boundaries:

$$T(x = l_A/2) = T_c \quad \text{and} \quad T(x = l_A/2 + l_M) = T_\infty.$$

T_c is obtained by matching both solutions ($q_{in} = q_{out}$)

$$T_c = \frac{q_A \cdot l_A \cdot l_M}{2V_A \cdot k_M} + T_\infty.$$

The maximal temperature is reached in the center of the actuator (Fig. 2.11):

$$T_{A,max} = \frac{q_A l_A^2}{8V_A k_A} + T_c \quad (2.12)$$

2.3.4 Transient conduction

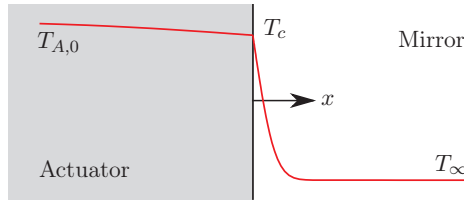


Figure 2.12 / Transient heat flow from one semi-infinite solid onto another. Boundary conditions are the initial actuator temperature $T_{A,0}$, initial mirror temperature T_∞ and a constant interface temperature T_c .

The transient behavior is analyzed by considering two semi-infinite solids (see Fig. 2.12) with different temperatures brought into contact at $t = 0$ s [37, p. 210]. By omitting internal heating, the differential equation is

$$\frac{\partial^2 T}{\partial x^2} = \frac{\rho c_p}{k} \frac{\partial T}{\partial t}. \quad (2.13)$$

A method to solve this equation is by neglecting the contact resistance and using the error-function ($\text{erf} = 1 - \text{erfc}$) [15, ch. 7.1]:

$$\text{erf}(z) = \frac{2}{\sqrt{\pi}} \int_0^z \exp(-t^2) dt$$

The temperature distribution inside the mirror reads:

$$T_M(x, t) = (T_c - T_\infty) \cdot \text{erfc} \left[\frac{x}{2} \sqrt{\frac{\rho_M c_{p,M}}{k_M t}} \right] + T_\infty \quad (2.14)$$

and inside the actuator:

$$T_A(x, t) = (T_{A,0} - T_c) \cdot \text{erf} \left[\frac{-x}{2} \sqrt{\frac{\rho_A c_{p,A}}{k_A t}} \right] + T_c. \quad (2.15)$$

$T_{A,0}$ is the initial actuator temperature, the temperature at the interface T_c

$$T_c = \frac{T_{A,0} \sqrt{k_A \rho_A c_{p,A}} + T_\infty \sqrt{k_M \rho_M c_{p,M}}}{\sqrt{k_A \rho_A c_{p,A}} + \sqrt{k_M \rho_M c_{p,M}}}$$

using $q_{in} = q_{out}$. As an example the solutions for equations (2.14) and (2.15) are shown in figure 2.13 and 2.14 respectively. Material properties of table 2.2 are used and the temperature is evaluated at $t = [1 \text{ ms}, 10 \text{ ms}, 0.1 \text{ s}, 1 \text{ s}]$. The boundary conditions are: initial actuator temperature $T_{A,0} = 23^\circ\text{C}$ and ambient temperature $T_\infty = 22^\circ\text{C}$, resulting in an interface temperature of $T_c \approx 22.91^\circ\text{C}$.

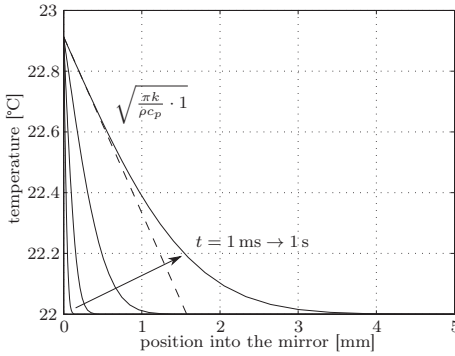


Figure 2.13 / Temperature distribution for a semi-infinite Zerodur[®] mirror for time $t = [1 \text{ ms}, 10 \text{ ms}, 0.1 \text{ s}, 1 \text{ s}]$. Dotted line is the depth of penetration $x(t = 1 \text{ s}) = 1.6 \text{ mm}$

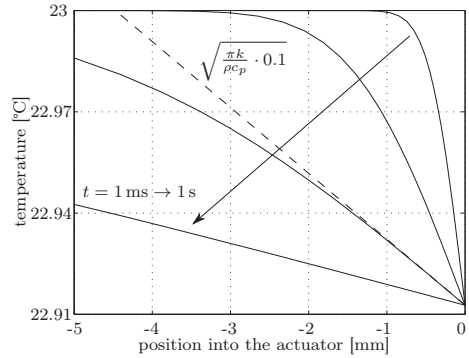


Figure 2.14 / Temperature distribution for a semi-infinite aluminum 6061 actuator for time $t = [1 \text{ ms}, 10 \text{ ms}, 0.1 \text{ s}, 1 \text{ s}]$. Dotted line is the depth of penetration $x(t = 0.1 \text{ s}) = 4.5 \text{ mm}$

2.3.5 Natural convection

In air, heat is also transferred by convection. The convection coefficient for a horizontal cylinder [37, p. 427] is approximated by:

$$\tilde{h} \approx \frac{k_{\text{air}}}{D_A} \cdot \left\{ 0.60 + \frac{0.387 \cdot \text{Ra}^{1/6}}{\left[1 + \left(\frac{0.559}{\text{Pr}} \right)^{9/16} \right]^{8/27}} \right\}^2 \quad (2.16)$$

with Rayleigh number

$$10^{-5} < \text{Ra} = \frac{g \rho_{\text{air}} c_{p,\text{air}} (T_A - T_\infty) D_A^3}{\nu_{k,\text{air}} k_{\text{air}} T_\infty} < 10^{12} \quad (\text{for gasses}). \quad (2.17)$$

The Prandtl number for air is

$$\text{Pr} = \frac{\nu_{k,\text{air}} \rho_{\text{air}} c_{p,\text{air}}}{k_{\text{air}}} \approx 0.708.$$

The other parameters at an air temperature of $T_\infty = 22^\circ\text{C}$ are listed in table 2.1. The

Table 2.1 / Natural convection parameters.

| | |
|-------------------------------|---|
| air density | $\rho_{\text{air}} = 1.177 \text{ kg/m}^3$ |
| specific heat capacity of air | $c_p = 1005.7 \text{ J/kgK}$ |
| kinematic viscosity of air | $\nu_{k,\text{air}} = 15.68 \cdot 10^{-6} \text{ m}^2/\text{s}$ |
| thermal conductivity of air | $k_f = 0.02624 \text{ W/mK}$ |
| gravitational acceleration | $g = 9.81 \text{ m/s}^2$ |

heat transferred from the actuator to the surroundings by natural convection is

$$q = \hbar \pi D_A l_A (T_A - T_\infty) \quad (2.18)$$

2.4 Realization

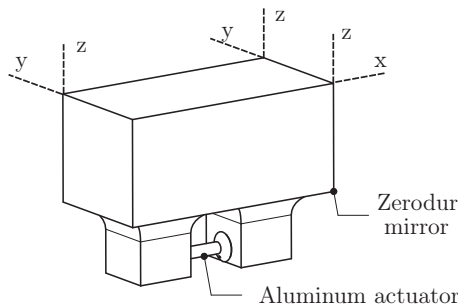


Figure 2.15 / The mirror with one actuator with $r = 18.3 \text{ mm}$ and boundary conditions that are used for finite element calculation.

2.4.1 Material selection

In figure 2.9 the mirror deflection as function of different materials is shown. Substituting ΔT given by (2.5) into equation (2.3), the following term with material properties appears:

$$\frac{\alpha}{\rho c_p}.$$

The larger this term, the larger the deflection per inserted heat. It is a product of the thermal sensitivity (α/k) with the volumetric thermal distribution ($k/\rho c_p$). The first determines how sensitive the material is to thermal gradients, the latter how fast a body adapts to a new temperature in terms of characteristic time, see (2.8). For this application α/k should be small, since large internal stresses due to applied thermal gradient are undesired. For a fast actuator response $k/\rho c_p$ should be large. Based on these parameters aluminum is chosen as actuator material, because:

1. its volumetric thermal distribution is almost two times higher,
2. its thermal sensitivity is two times lower (compared to zinc) and,
3. its good availability and machinability.

Based on the specifications given in table 1.2 a shape factor of $\Upsilon = 2$ is chosen. This enables an actuator spacing of 20 mm with a realistic mirror thickness of $h \approx 20$ mm. Various dimensions are simulated using finite elements (FEA). Figure 2.15 shows the realized mirror and also the boundary conditions used, the dimensions are shown in Fig. 2.18. The thickness is $h_m = 18.3$ mm and the actuator is placed at maximal deflection $r_{\text{opt}} \approx 18.35$ mm (shown as a diamond in Fig. 2.6 and 2.8). Outer dimensions are $40 \times 20 \times 30$ mm. An overview of all dimensions is given in table 2.2. Mirror deflection in FEA is $\delta = 4.0$ nm/c. The Zerodur[®] mirror is shown in Fig. 2.16, the aluminum 6061 actuator in figure 2.17.

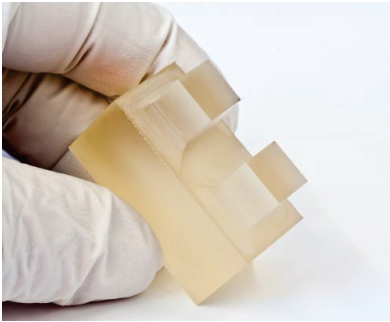


Figure 2.16 / Experimental mirror.

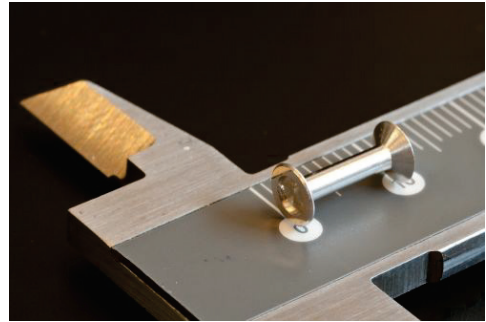


Figure 2.17 / Experimental actuator.

Parts are made in a close fit (at room temperature 20°C) with $\sim 4 \pm 2$ μm play and glued with Araldite[®] 2020 from Huntsman. The geometry of the glue chamber is shown in figure 2.18(c). Glue is injected from the side via a glue-gate. By using a needle with a smaller diameter ($\text{\O}0.3$ mm) the air escapes through the same opening. Advantage of this method is the direct contact between aluminum and glass, prescribing the actuator position. This contact is preloaded by the shrinkage of the glue inside the chamber.

Table 2.2 / Parameters and material properties of the mirror with one actuator.

| | | | |
|----------|--------------------------------|---|-----------------------|
| Mirror | material | Zerodur [®] | |
| | thickness | $h_M = 18.3 \text{ mm}$ | |
| Post | width | $w_M = 20 \text{ mm}$ | |
| | Young's modulus | $E_M = 91 \text{ GPa}$ | |
| | density | $\rho_M = 2530 \text{ kg/m}^3$ | |
| | Poisson's ratio | $\nu_M = 0.24$ | |
| | thermal expansion coefficient | $\alpha_M = 0.05 \text{ } \mu\text{m/m}\cdot\text{K}$ | |
| | thermal conductivity | $k_M = 1.64 \text{ W/m}\cdot\text{K}$ | |
| | specific heat capacity | $c_{p,M} = 821 \text{ J/kg}\cdot\text{K}$ | |
| | shape factor | $\Upsilon = 2$ | |
| | Actuator | same material as mirror | |
| | | width | $w_P = 10 \text{ mm}$ |
| Actuator | thickness | $h_P = 10 \text{ mm}$ | |
| | distance to mirror center-line | $r = 18.3 \text{ mm}$ | |
| | material | aluminum 6061 | |
| | length | $l_A = 10 \text{ mm}$ | |
| | diameter | $D_A = 2 \text{ mm}$ | |
| | volume | $V_A = 50 \cdot 10^{-9} \text{ m}^3$ | |
| | Young's modulus | $E_A = 70 \text{ GPa}$ | |
| | density | $\rho_A = 2700 \text{ kg/m}^3$ | |
| | Poisson's ratio | $\nu_A = 0.33$ | |
| | thermal expansion coefficient | $\alpha_A = 23.6 \text{ } \mu\text{m/m}\cdot\text{K}$ | |
| | thermal conductivity | $k_A = 154 \text{ W/m}\cdot\text{K}$ | |
| | specific heat capacity | $c_{p,A} = 896 \text{ J/kg}\cdot\text{K}$ | |
| | ambient temperature | $T_\infty = 22 \text{ }^\circ\text{C}$ | |

Actuator stiffness is approximated by

$$c_A \approx \frac{E_A A_A}{l_A} = \frac{70 \cdot 10^9 \cdot \frac{1}{4} \pi (2 \cdot 10^{-3})^2}{10 \cdot 10^{-3}} = 22 \cdot 10^6 \text{ N/m.} \quad (2.19)$$

The stiffness of the glue layer ($2 \cdot 5 \text{ } \mu\text{m}$) is

$$c_{\text{glue}} \approx \frac{1 \cdot 10^9 \cdot 9.6 \cdot 10^{-6}}{1 \cdot 10^{-5}} = 960 \cdot 10^6 \text{ N/m,} \quad (2.20)$$

so the glue layer is approximately 40 times stiffer and therefore the displacement of the actuator will dominate the mirror deformation.

A surface measurement is obtained before and after gluing (Fig. 2.19(a) and 2.19(c)) with a Zygo[®] VeriFire[™] interferometer. Some cross sections over the surface are analyzed and given in figure 2.19(b) and 2.19(d). A relative surface map (Fig. 2.19(e) and 2.19(f)) is calculated by importing the data in Matlab[®]. A mirror deflection of $\delta = 2.8 \pm 0.4 \text{ nm}$ is measured. Possible explanations are

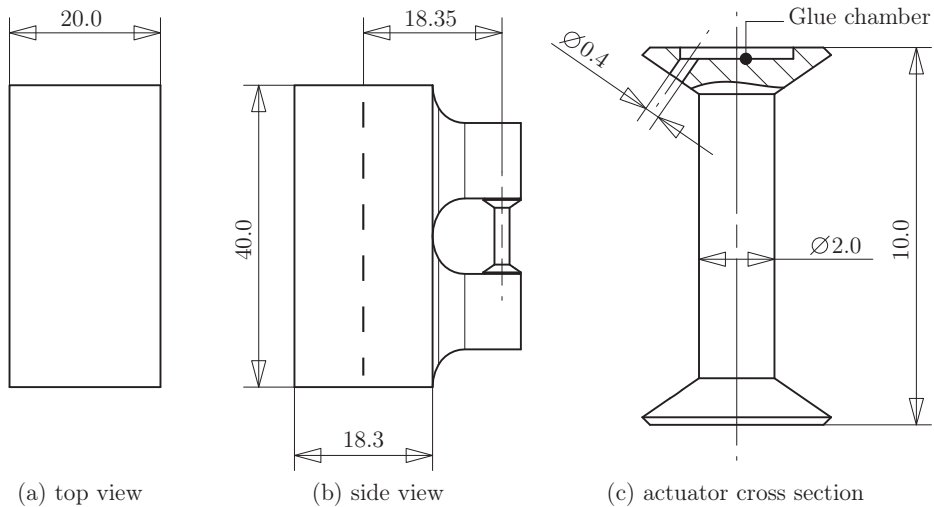


Figure 2.18 / Main dimensions of the deformable mirror with one actuator.

- glue shrinkage inside the glue layer,
- different measurement temperatures,
- temperature difference during assembly,
- non-steady temperature during curing (half shear strength is after 24h).

Since this deflection is in the negative direction, it can be compensated by pre-heating the actuator to flatten the mirror to the shape of Fig. 2.19(a).

2.5 Validation

To characterize the mirror with one actuator, the front surface is measured with a Zygo[®] interferometer at different actuator temperatures. Mechanical and thermal hysteresis is investigated and various temperature step responses are measured.

2.5.1 Joule heating

A simple method to heat the actuator is by resistance wire (see also appendix B). Enamelled wire (26 windings of a Cu-Ni alloy) is used, with a diameter of $\text{Ø}0.1$ mm and a total resistance of $12.5 \pm 0.2 \Omega$, see Fig. 2.20. A linear relation between mirror deflection and inserted heat is $0.21 \pm 0.01 \text{ nm/mW}$, shown as fit in figure 2.21.

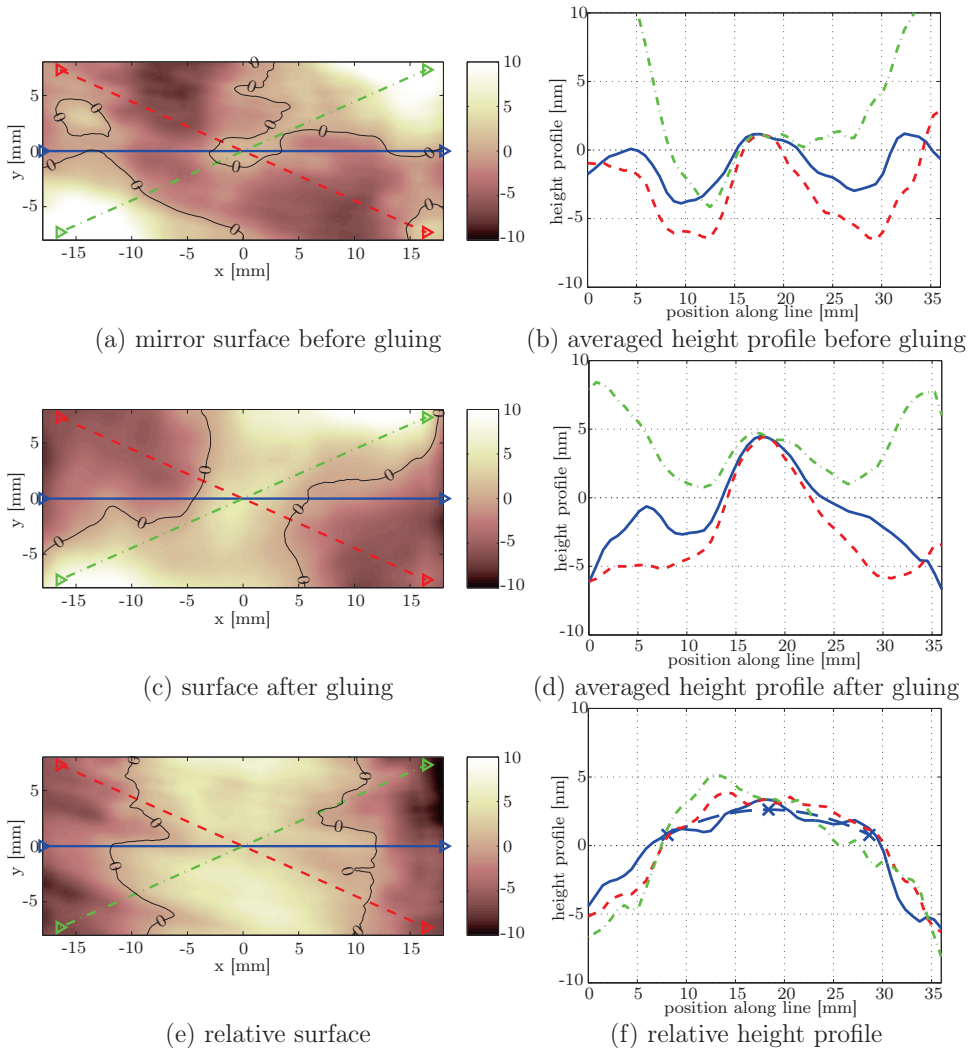


Figure 2.19 / Mirror front surface data obtained with a Zygo® interferometer: (a) before gluing the actuator, (c) after gluing and (e) relative (meaning fig(c) - fig(a)). Averaged cross sections: (b) before gluing, (d) after gluing and (f) relative. In (f) also the second order fit is shown with a mirror deflection of $\delta = 2.8 \pm 0.4$ nm.

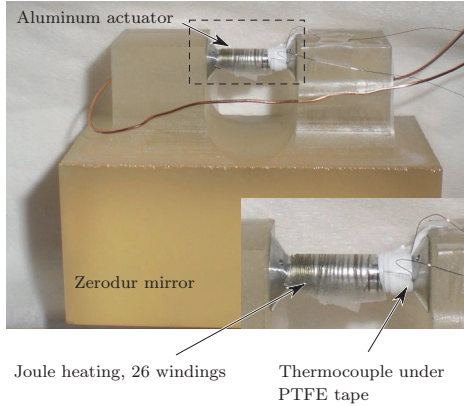


Figure 2.20 / Joule heating with resistance wire and a fine gage thermocouple.

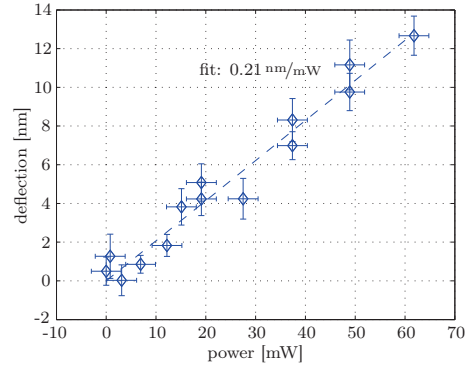


Figure 2.21 / Mirror deflection as function of inserted actuator power including measurement uncertainties. The linear fit is: 0.21 ± 0.01 nm/mW.

2.5.2 Practical temperature measurement

The actuator temperature is measured with a fine gage (≤ 0.075 mm) thermocouple to minimize the heat leakage through the sensor [23, 52]. The emf generated at the junction is measured with a USB-temp measurement module from MEASUREMENT COMPUTING [2]. This is an 8 channel 24 bit analog digital converter (Sigma Delta). The measurement accuracy of the two on-board cold junction compensator's ($\simeq 0.5^\circ\text{C}$) is increased with a thin film platinum sensor (Pt100) as a separate cold junction. Setup used is shown in figure 2.24. The platinum sensor is connected in a four-wire configuration to exclude errors due to differences in wire resistances. Since the reference junction is at some temperature other than 0°C the thermocouple reference table [4] cannot be used directly.

The compensation procedure is as follows [23, p. 117]:

1. Measure the emf across terminals.
2. Measure the reference temperature at the terminals by some independent means (Pt100).
3. Convert the reference temperature into an equivalent emf using the tables.
4. Add the measured emf to the equivalent emf to give a total emf.
5. Convert the total emf to a temperature using the tables. This is the temperature of the thermoelectric junction (the tip).

In figures 2.22 and 2.23 a measurement set of simultaneous surface shape and the temperature data is shown. A good relation between temperature and relative deflection

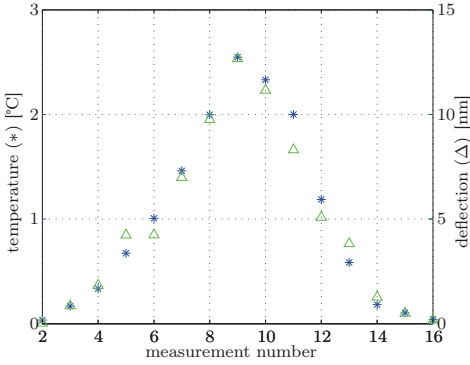


Figure 2.22 / Mirror deflection and actuator temperature, assuming steady state behavior on each measuring point.

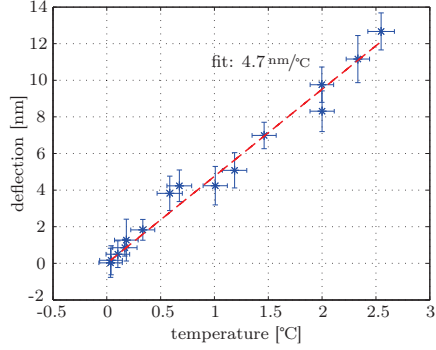


Figure 2.23 / Mirror deflection as function of actuator temperature including measurement uncertainties. A linear fit gives $4.7 \pm 0.2 \text{ nm}/^\circ\text{C}$.

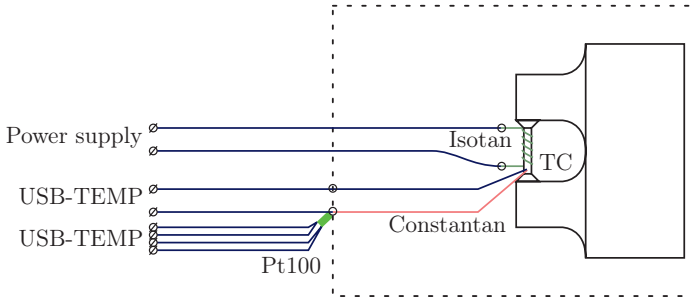


Figure 2.24 / Temperature measurement setup using a thermocouple (TC) and a separate cold junction compensation with a Pt100.

is observed with low hysteresis and linear behavior: $4.7 \pm 0.2 \text{ nm}/^\circ\text{C}$. From this set of measurements also the characteristic time constant is estimated:

$$\tau \approx 10 \text{ s}, \quad t_{1/2} \approx 7 \text{ s} \quad (2.21)$$

Relative mirror surfaces of measurement numbers 7,9 and 16 are shown in figure 2.25. This set of measurement results can be compared with the analytical model, using the dimensions and material properties of 2.2. The deflection with equation (2.3) is $\delta = 3.6 \text{ nm}/^\circ\text{C}$. The time constant (eq. 2.8, using $l_M = 15 \text{ mm}$) is

$$\tau = 11 \text{ s}, \quad t_{1/2} = 7.7 \text{ s}.$$

Actuator energy is $0.12 \text{ J}/^\circ\text{C}$, using (2.5). As an indication for the actuator power, the

time constant $\tau = 11$ s and deflection $\delta = 3.6$ nm/°C is used for a temperature rise of $\Delta T = 1$ °C:

$$q_A \approx 3 \text{ mW/nm}$$

2.6 Conclusion and discussion

An experimental mirror with one single actuator is modeled, realized and tested. Presented results are obtained from different measurements performed in the thermally controlled optical measurement room at TNO Delft. Various finite element analyzes are done. Results are summarized in table 2.3.

Table 2.3 / Specifications experimental mirror with one actuator.

| | |
|--|--|
| mirror material | Zerodur® |
| actuator material | aluminum 6061 |
| mirror deformation (fit) | $\delta = 4.7 \pm 0.2$ nm/°C (0.21 ± 0.01 nm/mW) |
| joule heating (fit) | 0.044 ± 0.002 °C/mW |
| time constant (fit) | $\tau \approx 10$ s ($t_{1/2} \approx 7$ s) |
| mirror deformation (FEA) | $\delta = 4.0$ nm/°C |
| mirror stress (FEA) | $\sigma_{\text{Von Mises}} < 2$ MPa (at actuator - mirror interface) |
| time constant (FEA) | $\tau \approx 13$ s ($t_{1/2} \approx 9$ s) |
| characteristic heating (thermal model) | $q \approx 3$ mW/nm |

Considering the mirror deformation, the fitted value ($\delta = 4.7 \pm 0.2$ nm/°C) is a bit higher compared to FEA ($\delta = 4.0$ nm/°C, section 2.4.1) and analytical ($\delta = 3.6$ nm/°C, Fig. 2.6). The difference of the last value is partially explained by differences in geometry. For example, the actuator stiffness with glue chambers is $c_{A,\text{FEA}} = 24 \cdot 10^6$ N/m, almost 10% higher than the analytical one (eq. 2.19: $22 \cdot 10^6$ N/m). Same is true for geometrical differences of the mirror. Furthermore, the difference between FEA and analytical could be attributed to the fact that a first order analytical model is used, that neglects the shearing of the mirror body. Differences between FEA and measured displacement and time constants are due to manufacturing tolerances, variations in material properties and measurement uncertainties. Note also that the time constant from FEA is approximated based on a coarse approximation of the natural convection coefficient (equation 2.18).

Reconsidering the active mirror requirements stated in table 1.2, the realized mirror with one actuator performs well within the specifications. Actuator spacing of 20 mm is possible, with a mirror deflection of 10 nm. With a characteristic timescale of 10 s the power consumption in a vacuum environment is in the order of 3 mW/nm per actuator, so 63% of the measured value with convection. Intrinsic to the thermo-mechanical

technology, hysteresis is negligible. There is a linear correlation between actuator temperature and mirror deflection. Absence of electromagnetic interference exclude the interaction with the mirror suspension.

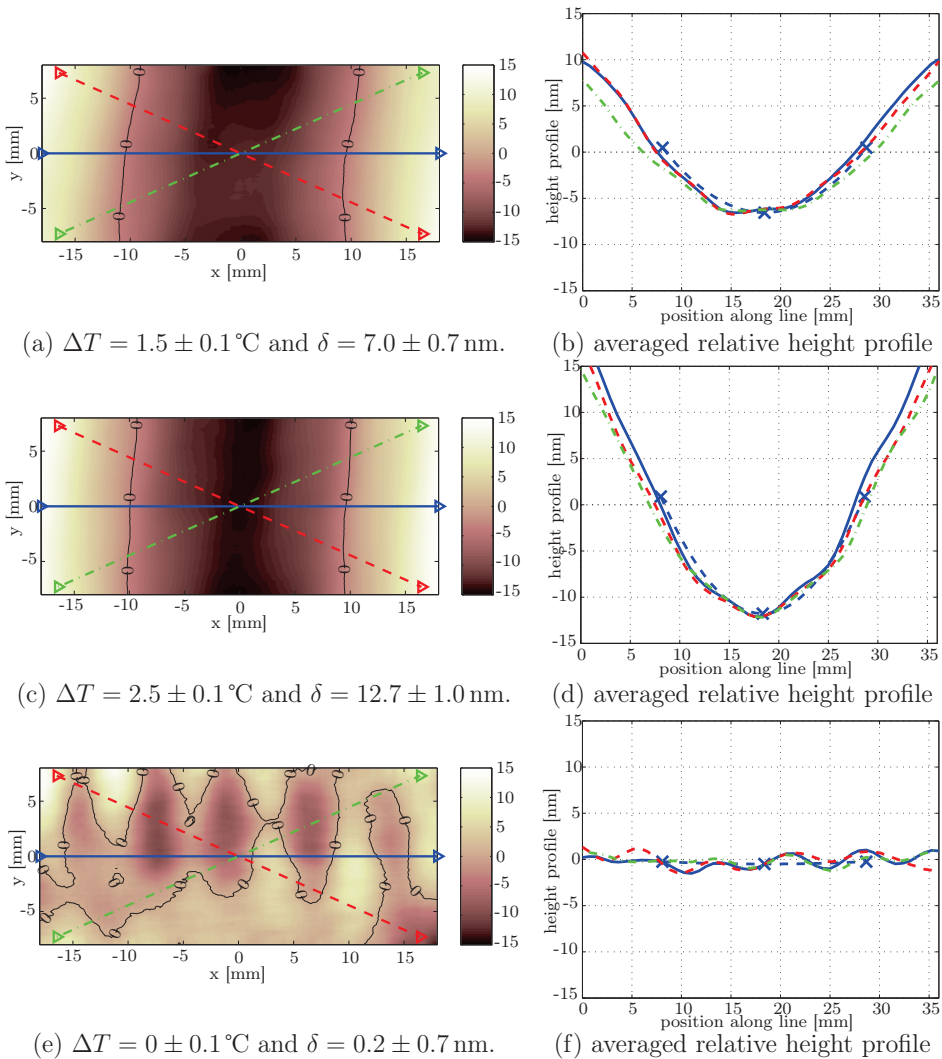


Figure 2.25 / Relative mirror front surface data obtained with a Zygo[®] interferometer: (a) measurement 7, (c) 9 and (e) 16 (referring to Fig. 2.22) with corresponding averaged height profiles (b), (d) and (f).

Mirror with four actuators

In this chapter the realization and validation of an experimental deformable mirror with four actuators is discussed. Its geometry is an extension of the mirror with one bending moment actuator from chapter 2. The experimental mirror, as discussed in this chapter, is used to further investigate the concept and to measure the mechanical and thermal actuator coupling. To approach the sizes of current EUV mirrors inside a lithography projection system, this geometry can be extended toward larger mirrors with more actuators.

3.1 Realization

Compared to the mirror with one actuator, the same optimal distance between the neutral axis of the mirror and the actuator center is used ($r = 18.35$ mm). Figure 3.1 shows the major dimensions and the actuator numbering. The actuators are placed in a square grid with an actuator pitch of $p_A = 20$ mm. When making a full grid, four actuators are connected to one mirror post.

Zerodur[®] is used as mirror material. Starting from a $40 \times 40 \times 30$ mm block, the grooves are made by conventional glass grinding. The front surface is extensively polished toward a 21 nm peak to valley ($\lambda/25$) and 4 nm rms, see Fig. 3.4(a). All major edges have a 0.2 mm chamfer, to avoid chipping.

The actuators are made from aluminum 6082, having a thermal conductivity of $k_A \approx 170$ W/mK. Figure 3.2 shows the actuator with its main dimensions. The glue chamber is redesigned compared to the first mirror (Fig. 2.18c) to reduce air inclusion. All actuators are glued simultaneously by inserting the glue with a needle via the glue-gate. Inside air escapes through the same opening around the needle. Dowel pins are used during curing of the glue, to prescribe the distance between actuator and groove (Araldite 2020, half shear strength after 24 hours).

Actuator heating is done using resistance wire ($13.8 \pm 0.2 \Omega$ each, see figure 3.3) and cooling passively by convection. Type T thermocouples (copper-constantan) with $50 \mu\text{m}$ diameter are used for temperature measurement. The dots in figure 3.1(b) correspond

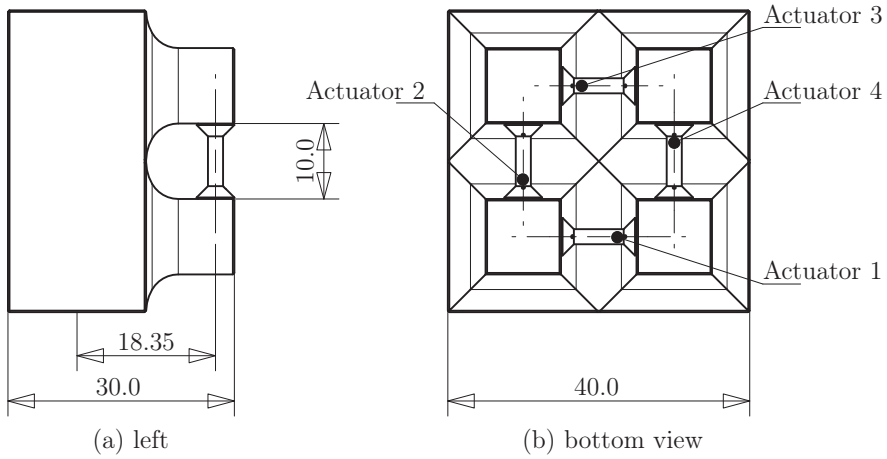


Figure 3.1 / Main dimensions of the deformable mirror with four actuators. Dot locations of the actuator numbering correspond with the locations of the thermocouple tips (drawing scale 1:1).

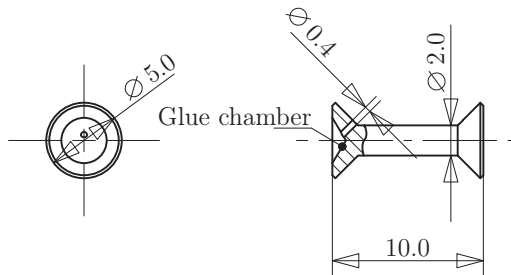


Figure 3.2 / Main dimensions of the actuator with a break-out section view of the glue chamber (drawing scale 2:1).

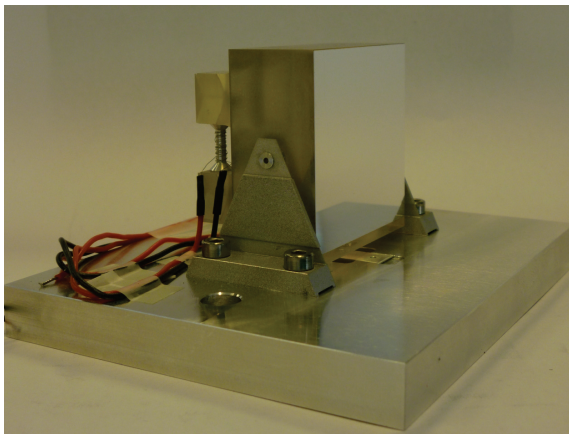


Figure 3.3 / The deformable mirror with four actuators.

to the locations of the thermocouple tips. The transition from constantan to copper wire, is made by a copper connector. Its temperature is measured with a four wire platinum resistance thermometer (Pt100) to enable a cold junction compensation (the method is described in sec. 2.5.2).

Figure 3.4 shows surface measurements that are made with a Zygo[®] VeriFire[™] interferometer. These are further analyzed using MATLAB[®]: the raw Zygo data is linearly mapped on a rectangular grid using `griddata` and averaged with `imfilter` over 12×12 pixels ($\approx 0.5 \times 0.5$ mm). Also the piston, tip and tilt components of each data-set are removed, using singular value decomposition. Height values in the color bars are in nm, the x and y values are absolute mirror positions. The data is cropped a few mm to remove the edge. A solid contour-line indicates the surface intersection at $z = 0$. Four surface cross-sections are made over the solid, dashed, dash-dotted and dotted lines. These are shown in the figures (b), (d), and (f). There, the horizontal axis is the position along the line, where the direction is indicated with triangles in the figures to the left.

Figure 3.4(a) shows the surface after polishing with a peak to valley of 21 nm (4 nm rms) within a 36 mm pupil. Conventionally, similar surfaces are polished on a turn table by centrally pushing on the back-side of the optical component. Due to the varying thickness this results in ≥ 70 nm peak to valley. By symmetrically loading the mirror on the four posts, the in figure 3.4(a) shown surface shape is obtained.

Figure 3.4(c) shows the surface after the glue is fully cured. A 36 nm peak to valley with 10 nm rms is measured. The somewhat convex shape is best seen in the cross-section (d). Most likely, this deformation is caused by either glue shrinkage, different measurement and/or curing temperatures or a combination of those. Both measurements are done 7 days apart.

By subtracting the surface of Fig. 3.4(c) with (a), a relative surface is obtained, shown in Fig. 3.4(e) and (f). An almost symmetrical deformation is visible, meaning that the contour-line is circular and the cross-sections overlap. From this, it can be concluded that the deformation is identical for each actuator. The corresponding mirror deflection is calculated using a second order fit through the $y = 0$ cross section (solid line). The deflection is 7.5 ± 0.8 nm and is indicated with crosses in Fig. 3.4(f). The 0.8 nm error is the root mean square (rms) fitting error. Left and right crosses correspond with the locations of actuator number 4 and 2 respectively. The mirror center is at the middle cross. The mirror surface could be flattened toward the state before gluing, by heating all actuators to 1.6°C. This is discussed in section 3.2.2.

A thermally optimized mounting is designed (see figure 3.5) to use the mirror on a breadboard. The design focuses on:

- realizing a determined mounting on all six free body motions,

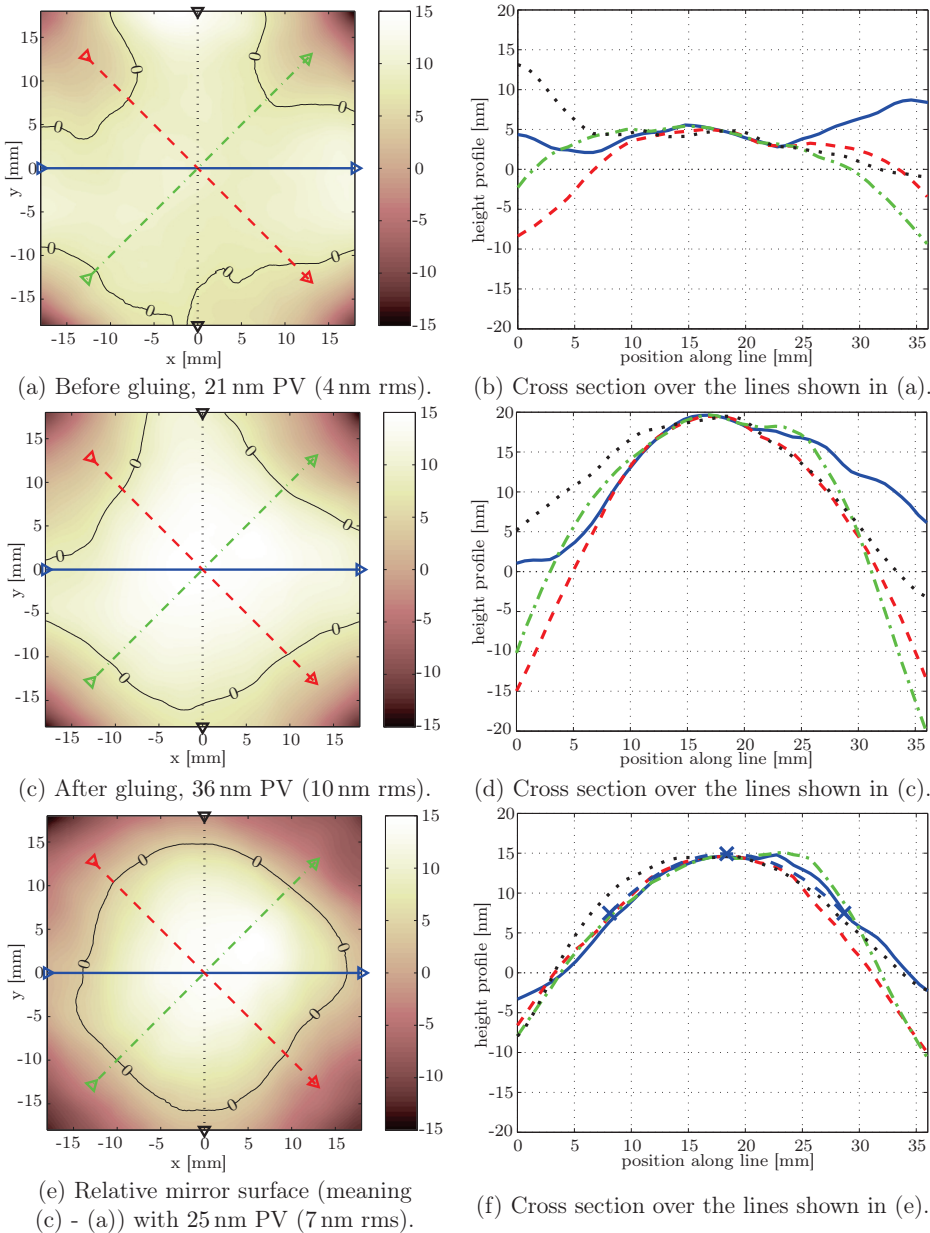


Figure 3.4 / Mirror front surface data obtained with a Zygo[®] interferometer: (a) before gluing the actuators, (c) after gluing and (e) relative (meaning (c) - (a)). Peak to valley (PV) and rms values are in a 36 mm circular pupil. On the right, corresponding averaged cross sections (b,d,f) with in the last also a second order fit of the mirror deflection $\delta = 7.5 \pm 0.8$ nm.

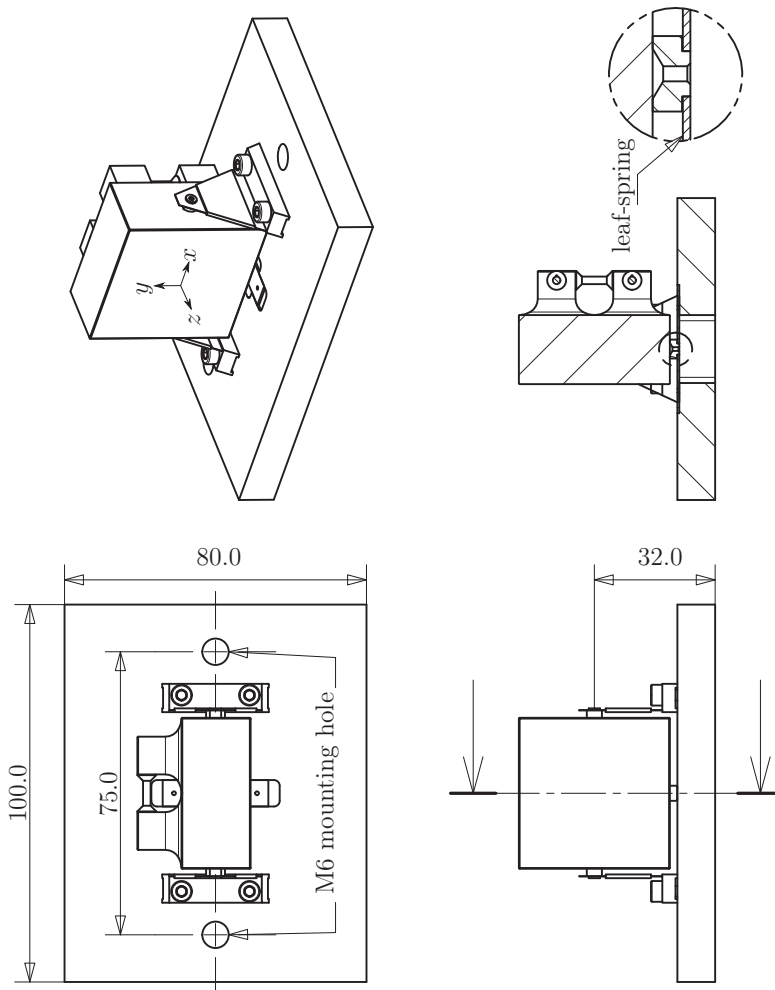


Figure 3.5 / The mounting of the deformable mirror with four actuators. (drawing scale 1:2)

- minimizing mirror tip and tilt due to temperature variations, and
- reduction of the introduced mounting forces by symmetrical mounting.

This is achieved by using A-shaped leaf-springs, with a thinned part of 0.1 mm, to fix the mirror in four directions (y , z and rotations around y and z). The other remaining two (x and rotation around x) are prescribed by a leaf-spring at the bottom of the mirror. Resulting surface deformation caused by a temperature difference between the mounting frame and the mirror are in the order of $0.1 \text{ nm}/^\circ\text{C}$ peak to valley. Mirror rotation around the x-axis is in the order of $2 \text{ nm}/^\circ\text{C}$ peak to valley. And y-axis rotation is negligible (below $0.1 \text{ nm}/^\circ\text{C}$). The first natural frequency is 1.1 kHz.

The sequence to assemble the mirror is first glue the fixations pins on the A-shaped leaf-springs. Then the bottom leaf-spring (with the lower fixation pin connected to it) is aligned and glued inside the pocket of the base-plate. The mirror is temporary placed on dowel-pins (with 2 mm diameter) and aligned above the bottom leaf-spring. Then the A-shaped leaf-springs are mounted onto the base. By simultaneously gluing all three fixation pins onto the mirror, the influence of the glue shrinkage is minimized. Finally the dowel pins are removed from underneath the mirror.

3.2 Validation

The measurements discussed in this section, are used to validate both theory and finite element simulations. They are also used to prove the concept of deforming a mirror with thermo-mechanical bending actuators.

All measurements are performed at room temperature and under normal pressure. Main reason is the availability of the Zygo interferometer in a thermally controlled room, that is dedicated for measuring optical components. Note that the actuator input powers used here, are an order higher when compared to the power needed to drive the mirror in vacuum.

3.2.1 Mirror model

The finite element analysis (FEA) software Ansys[®] is used for both structural and (transient) thermal models. A more detailed description of a model buildup is given in appendix C, the material properties used are given in appendix A. The surface deflection is calculated with the static structural solver with either measured actuator temperatures as input or material temperatures from a thermal solution.

To compare the measurement results with the thermal models, approximations of the convection coefficient $h(T)$ are used [37]. The mirror is modeled as a rectangular block

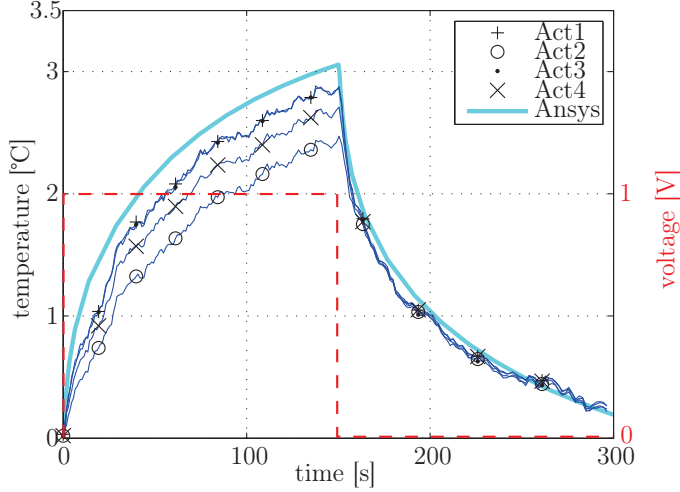


Figure 3.6 / Relative temperature measurement for heating all actuators with 72mW, (1 V). Heating is switched on at $t = 0$ s and off at $t = 150$ s. Data is sampled with 1Hz. The Ansys result (transient thermal) is based on the same heat input.

of $40 \times 40 \times 30$ mm:

$$\bar{h} \approx 0.6 \frac{k_{\text{air}}}{L} \text{Ra}^{1/4}, \quad (3.1)$$

using a thermal conductivity $k_{\text{air}} = 0.02624 \text{ W/m}\cdot\text{K}$ and a characteristic length $L = 40$ mm. The Rayleigh number is given by:

$$10^4 < \text{Ra} = \frac{g \rho_{\text{air}} c_{p,\text{air}} (T_M - T_\infty) L^3}{\nu_{k,\text{air}} k_{\text{air}} T_\infty} < 10^9, \quad (3.2)$$

using

$$\begin{aligned} \rho_{\text{air}} &= 1.177 \text{ kg/m}^3 & c_{p,\text{air}} &= 1005.7 \text{ J/kg}\cdot\text{K} \\ \nu_{k,\text{air}} &= 15.68 \times 10^{-6} \text{ m}^2/\text{s} & g &= 9.81 \text{ m/s}^2 \end{aligned}$$

and a mirror temperature T_M and an ambient temperature T_∞ . The actuators are approximated as cylinders with $\text{Ø}3$ mm diameter. Their corresponding convection coefficients are calculated using the equations given in section 2.3.5.

3.2.2 Simultaneously heating all actuators

Temperatures are obtained with the commercial data acquisition module USB-TEMP from MEASUREMENT COMPUTING [2]. The sampling frequency is approximately 1 Hz.

In MATLAB® the measured temperature is cold junction compensated and compared with the Ansys results.

Figure 3.6 shows the relative temperature response of simultaneously heating all actuators with 72 mW (1 V). On the right vertical axis the input voltage is visible. The response of actuator #1 and 3 are in this case almost similar, actuator #4 differs 0.2°C and actuator 2 0.45°C at $t = 150$ s. There are several explanations for this behavior. It could be a difference in thermal contact between thermocouple tip and actuator. Also, there is a 0.2Ω difference in electrical resistance of the heating coils. And there is a variation in thermal contact between the coil and the actuator. In Ansys a perfect thermal contact is assumed between heating coil and actuator. It is therefore plausible that the simulated temperature is a few percent higher compared to the measured one. However, this could also be caused by differences in material properties.

At $t \approx 115 \pm 5$ s a mirror surface measurement is done. The corresponding measured temperatures are:

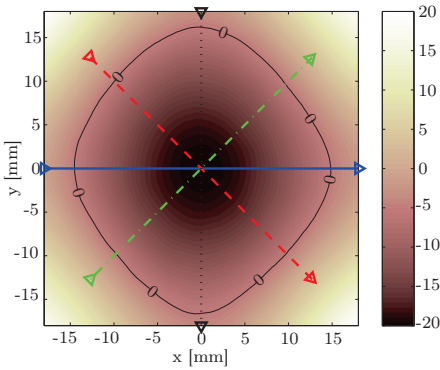
$$T_{\text{act1}} = 2.64^\circ\text{C} \quad T_{\text{act2}} = 2.19^\circ\text{C} \quad T_{\text{act3}} = 2.64^\circ\text{C} \quad T_{\text{act4}} = 2.46^\circ\text{C} \quad (3.3)$$

Figure 3.7(a) shows the relative surface at $t \approx 115$ s. This is a top view of the mirror, so the center $[x, y]$ of actuator #1 is at $[0, -10]$, #2 at $[10, 0]$, #3 at $[0, 10]$ and #4 at $[-10, 0]$. The height values in the color-bar are in nm and the intersection at $z = 0$ is drawn as solid contour-line. The fitted mirror deflection is $\delta = 11.7 \pm 1$ nm. As described in section 2.5 and 4.4.2, there is a linear relation between actuator temperature and mirror deflection. Averaging the above measured temperatures, a resulting deflection of $\delta = 4.7 \text{ nm}/^\circ\text{C}$ is obtained.

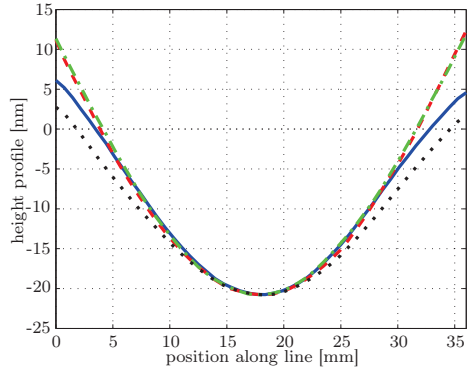
Using the relative temperatures of (3.3) as input for a steady state structural analysis in Ansys results in figure 3.7(c). Calculated mirror deflection is $\delta = 11.7 \pm 1$ nm. Subtracting this surface from the measured one gives 3.7(e) and indicates the mismatch between FEA and measurement. It is difficult to state repeatability, since this is a combination of a lot of factors, such as: uncertainties in material properties, temperature drift and measurement uncertainty and low spatial frequency position uncertainty of the interferometer. While taking the surface measurements, a relation is observed between number of fringes on the interferometer picture and that low spatial uncertainty. This is best seen by subtracting various steady state reference measurements at room temperature. This uncertainty is in the order of 1 nm (for an example, see figure 2.25(e)).

3.2.3 Step response of a single actuator

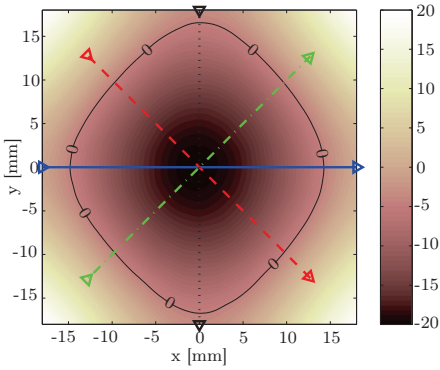
To further characterize the variations between actuators, they are successively heated with 1.2 V (104 mW). The temperature step responses are shown in figure 3.8. As already shown in Fig. 3.6, the relation between heat input and measured temperature



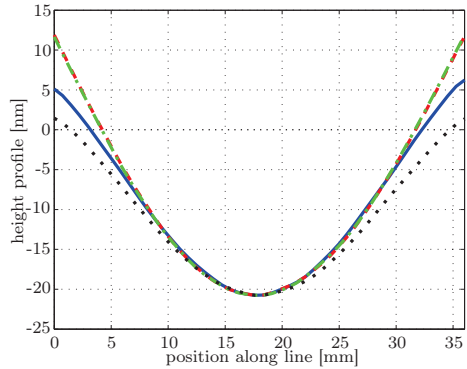
(a) Relative surface with all actuators at 72 mW (1 V).



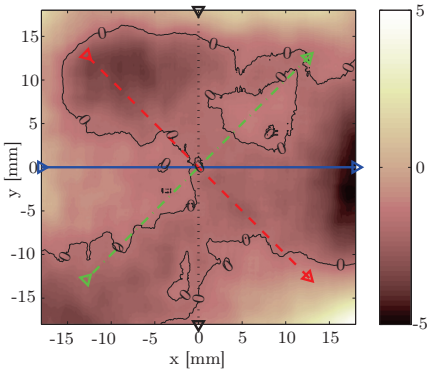
(b) Cross section over the lines shown in (a), mirror deflection is $\delta = 11.7 \pm 1$ nm.



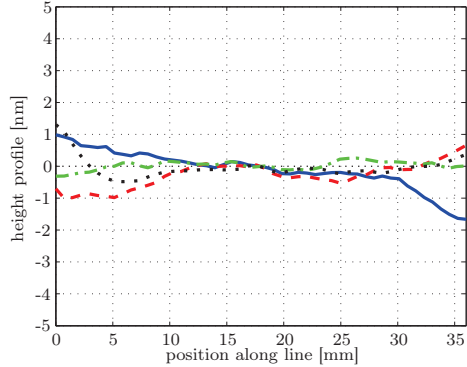
(c) Ansys surface at actuator temperatures given in (3.3).



(d) Cross section over the lines shown in (c), mirror deflection is $\delta = 11.7 \pm 1$ nm.



(e) Difference between Ansys FEA data and the Zygo measurement: (a) - (c).



(f) Cross section over the lines shown in (e).

Figure 3.7 / Comparison between Zygo measurement (a) and Ansys FEA surface data (c), while heating all actuators with 72 mW. The difference is given in (e) and the surface cross sections are shown to the right.

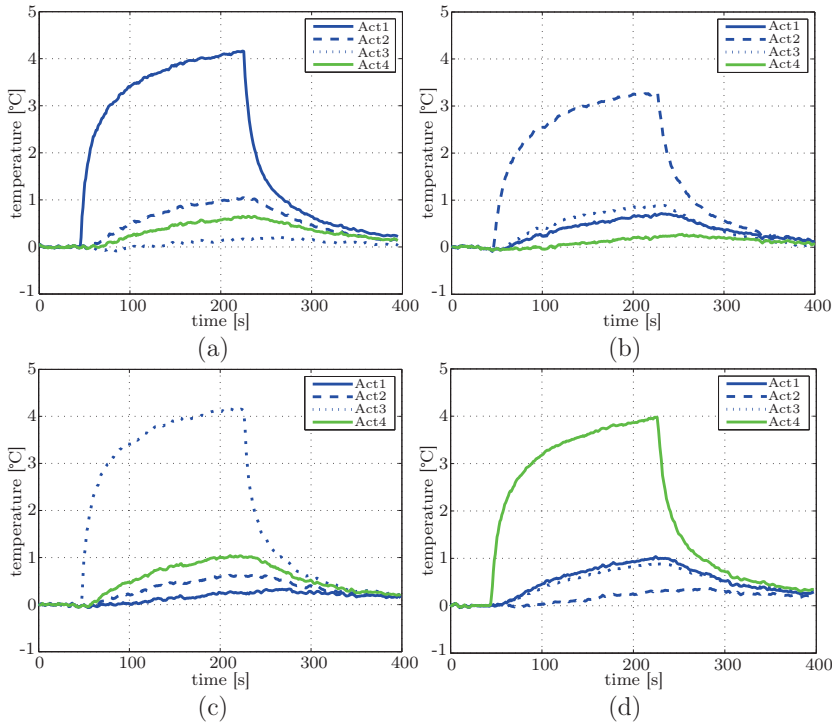


Figure 3.8 / Relative temperature step responses (starting from room temperature) for heating successively a single actuator on 104 mW (1.2 V) (a) actuator #1, (b) actuator #2, (c) actuator #3 and (d) actuator #4. Data sampled with 1 Hz.

are similar for actuator 1 and 3. Maximal values are: 4.14°C for actuator #1, 3.24°C for #2, 4.11°C for #3 and 3.93°C for #4. Figure 3.8 also shows the thermal coupling between the actuators. Heating actuator 1, result in a coupling to actuator #2 of 25%, to #3 of 3.8% and to #4 of 15%. As shown above in section 3.2.2, there is some difference in input \rightarrow output relation, but not all is explained with that. Another influence is the location of the thermocouple tip. This is analyzed in more detail using the next measurement.

Figure 3.9 shows a step response of heating actuator #4 with 165 mW. At $t = 20 \pm 5$ s and at $t = 90 \pm 5$ s a Zygo surface measurement is done, as indicated with arrows below the time-axis. This figure again shows the thermal coupling from the heated actuator to its neighbors. Looking at the FEA result for actuators #1 and 3 at $t = 125$ s, a temperature difference of 0.21°C is observed. In this simulation, the temperature probes are placed at the same locations as indicated in figure 3.1(b). Probes are also placed at the other ends of the actuators. For all, a gradient within actuators number 1 and 3 is observed. The simulated peak temperature for both actuators at the end close to the heated actuator #4 is 0.21°C higher compared to the other end, meaning

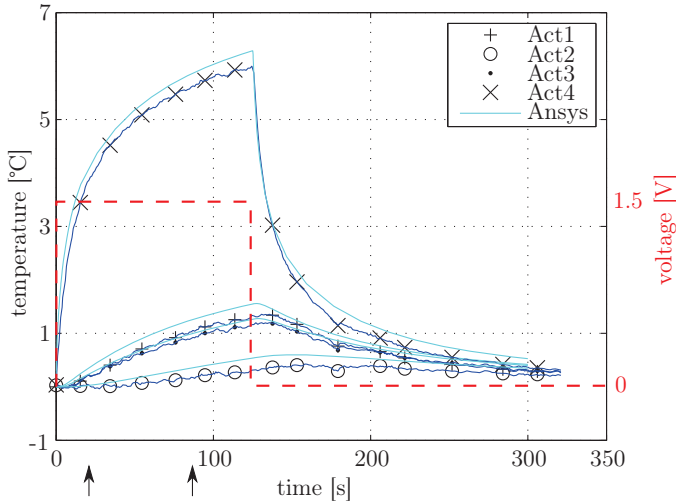


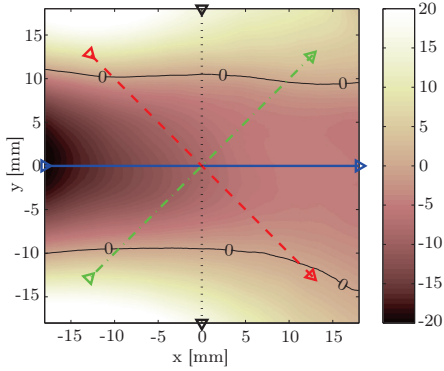
Figure 3.9 / Step response measurement for heating actuator #4 with 165 mW (1.5 V). Also the Ansys results are shown. The arrows below the time axis indicate the surface measurements given in 3.10(a,b) at $t = 20$ s and 3.10(c,d) at $t = 90$ s.

that there is a temperature gradient within actuator #1 and 3. This corresponds with the measurements shown in Fig. 3.8 and 3.9. In the measurement, the difference peak temperature (at $t = 125$ s) is 0.14°C and the corresponding actuator coupling is 21% for #1, 5% for #2 and 19% for #3.

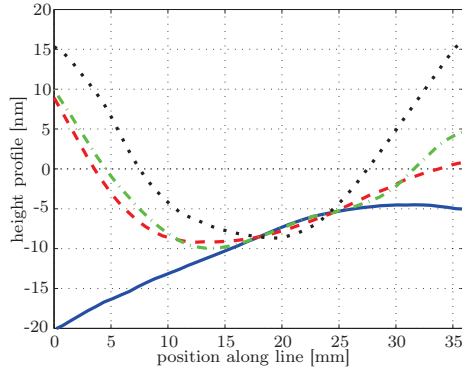
An explanation for this observation is that the actuator acts as a thermal bridge (or short-cut) between two mirror posts of different temperature. Therefore, the temperature at each end is prescribed by the mirror, having a higher thermal capacity.

The relative surface at $t \approx 20$ s is given in figure 3.10(a), with the cross section lines in (b). A deflection of $\delta = 14.7 \pm 0.7$ nm is measured at a temperature of $\Delta T(t \approx 20 \text{ s}) = 3.86 \pm 0.05^\circ\text{C}$. Figure 3.10(c) shows the surface at $t \approx 90$ s, where the deflection is $\delta = 19.2 \pm 1.0$ nm at temperature $\Delta T(t \approx 90 \text{ s}) = 5.66 \pm 0.05^\circ\text{C}$, so $\delta \approx 3.4$ nm/ $^\circ\text{C}$. The surface minimum is shifted toward the mirror center, mainly due to the thermal actuator coupling. Same behavior is observed in FEA, as shown in figure 3.11. In this simulation the 165 mW heat input is used and also the convection is taken into account.

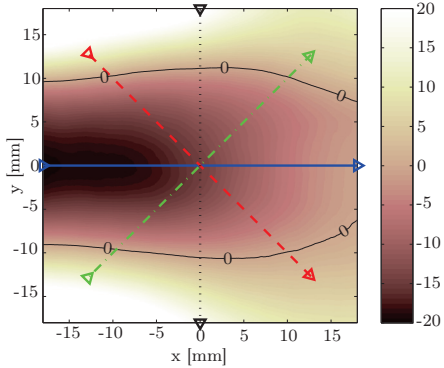
There is an uncertainty of $5 \rightarrow 10$ s between the Zygo and the FEA results. This is caused by the measurement methods: the temperature data is collected at another computer than the laser interferometer data. Furthermore, the raw Zygo data is selected by the VeriFire™ interferometer software out of three measurements within ≈ 5 s, where each measurement takes ≈ 1 s. This may be a cause for mismatch in absolute value between Zygo and FEA.



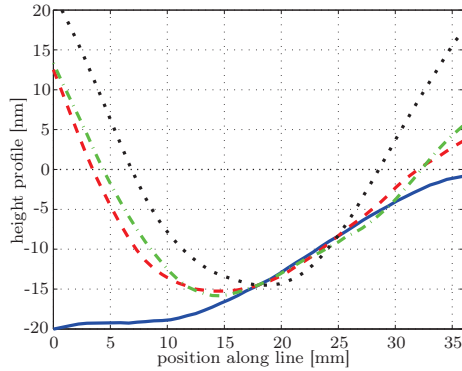
(a) $\Delta T = 3.86 \pm 0.05^\circ\text{C}$ and $\delta = 14.7 \pm 0.7 \text{ nm}$.



(b) averaged relative height profile



(c) $\Delta T = 5.66 \pm 0.05^\circ\text{C}$ and $\delta = 19.2 \pm 1.0 \text{ nm}$.



(d) averaged relative height profile

Figure 3.10 / Zygo interferometer surface data of a step response while heating actuator #4 with 165 mW. Surface (a) is at $t \approx 20 \text{ s}$ and (c) at $t \approx 90 \text{ s}$. In (b) and (d), surface cross-sections are shown, corresponding thermal response is shown in Fig. 3.9.

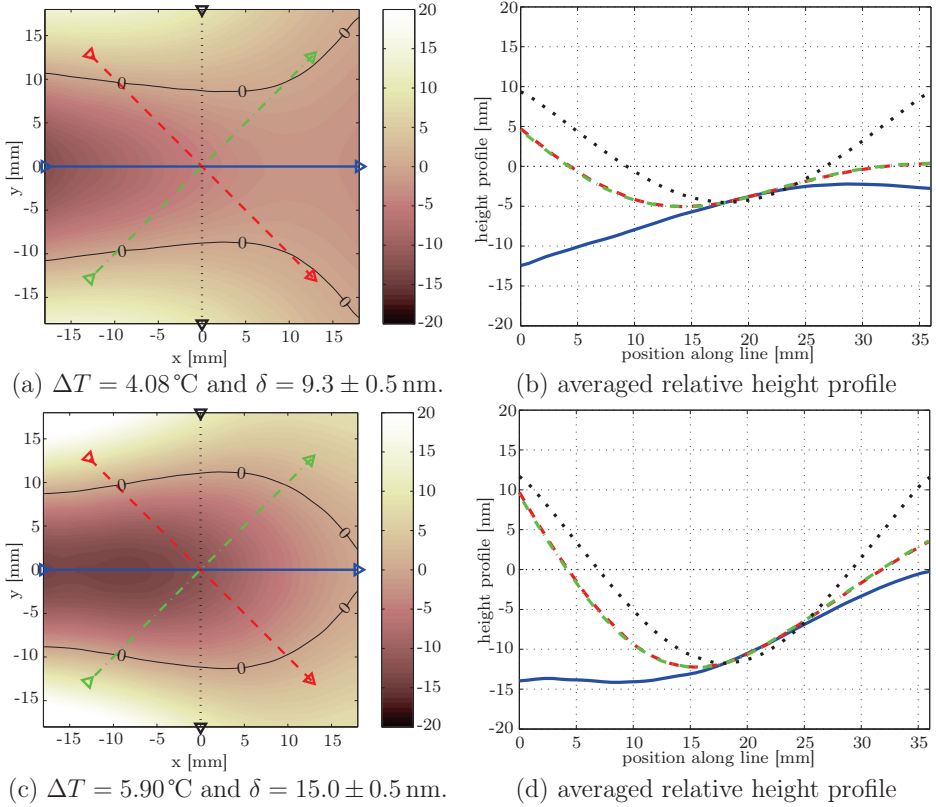


Figure 3.11 / Surface data of an Ansys structural combined with a transient simulation. A 165 mW heat input at actuator #4 is simulated and also the convection is taken into account. Surface (a) is calculated at $t = 20$ s and (c) at $t = 90$ s. Corresponding thermal response is shown in Fig. 3.9.

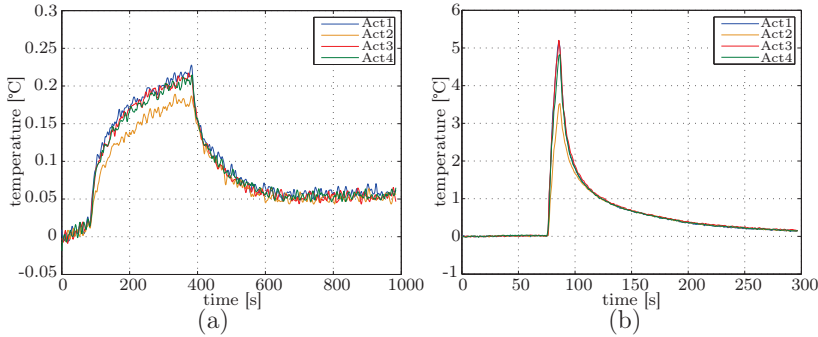


Figure 3.12 / Temperature step responses while heating all actuators simultaneously: (a) relative actuator at heating all actuators with 3 mW (0.2 V) for 5 min. (b) Shows the relative temperature at heating all actuators with 0.3 W (2 V) for 10 s. All data is sampled at 1 Hz and filtered with a 2nd order low-pass filter at a 1/8 Hz cut-off frequency.

Actuator speed

The following two measurements characterize the thermal time response of the mirror. Figure 3.12 shows the step responses at two inputs: (a) 3 mW and (b) 300 mW. The difference in start and end temperature in Fig. 3.12(a) is caused by thermal drift between cold junction and thermal couple. This measurement was performed at a normal workplace. But, that drift of $\approx \frac{0.05}{10} \text{ }^\circ\text{C}/\text{min}$ is low enough to distinguish the temperature change. To characterize the thermal time response, the first 10 samples of both data sets are linearly fitted.

A linear fit over heating all actuators with 3 mW, gives: $7 \times 10^{-3} \text{ }^\circ\text{C}/\text{s}$. When using the determined mirror deflection of $4.7 \text{ nm}/^\circ\text{C}$ an actuator speed of $33 \text{ } \mu\text{m}/\text{s}$ is demonstrated. The linear fit for heating the actuators with 0.3 W gives $0.7 \text{ }^\circ\text{C}/\text{s}$, thus $3.3 \text{ nm}/\text{s}$. For the 0.3 W response, the characteristic cooling time is $\tau = 5 \text{ s}$.

3.2.4 Reducing thermal actuator coupling

To reduce the thermal actuator coupling, the absolute thermal resistance between the actuators could be enlarged. Using the realized zerodur mirror, the path length between the actuators is extended by grinding small grooves into the mirror posts. This is shown in figure 3.13, where a Buehler[®] metal bonded diamond wafering blade is used with a diameter of 102 mm and a thickness of 0.3 mm. Results show a reduced actuator coupling from 25% to 10%, where the mirror deflection reduces to 55% compared to the version without grooves.

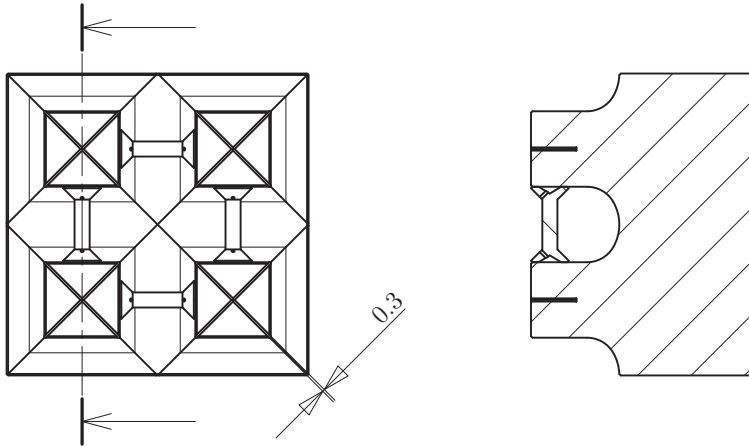


Figure 3.13 / The 2x2 mirror (scale 1:1)

3.3 Conclusion and discussion

An experimental mirror with four bending moment actuators is modeled, realized and validated. Its specifications are summarized in table 3.1. This mirror is an extension of the mirror with one actuator (see chapter 2). Glue chamber is slightly changed to reduce air inclusion. Joule heating coils are applied with a resistance of $13.8 \pm 0.2 \Omega$. A thermally optimized mounting is realized with minimal thermal drift in tip ($2 \text{ nm}/^\circ\text{C}$) and tilt (below $0.1 \text{ nm}/^\circ\text{C}$). Surface deformation caused by temperature variations between mirror and mounting are below $0.1 \text{ nm}/^\circ\text{C}$ peak to valley.

Mirror surface is measured at simultaneously heating all actuators. A deflection of 11.7 nm is measured while heating with 72 mW each. Corresponding average actuator temperature is 2.5°C . Actuator speeds are demonstrated while simultaneously heating all actuators with 3 mW and 0.3 W . They respectively are $33 \text{ pm}/\text{s}$ and $3.3 \text{ nm}/\text{s}$.

In a single actuator step-response, a mirror deflection of $3.4 \text{ nm}/^\circ\text{C}$ is measured, with a thermal actuator coupling of 30%. A design optimization is proposed and tested which reduces the coupling to 10%, while the mirror deflection at the same actuator input is reduced to 55%.

Table 3.1 / Specifications of the experimental mirror with four actuators.

| | |
|--------------------------|---|
| mirror material | zerodur [®] |
| actuator material | aluminum 6082 |
| mirror deflection | $3.4 \text{ nm}/^\circ\text{C}$ |
| resistance heating coils | $13.8 \pm 0.2 \Omega$ |
| demonstrated deflections | $\delta = 33 \text{ pm}/\text{s}$ and $3.3 \text{ nm}/\text{s}$ |
| actuator coupling | $\approx 30\%$, 10% after modification, see section 3.2.4 |

When using an adaptive mirror in an EUV lithography system, actuator strokes of $1 \text{ nm}/\text{min}$ are required (see table 1.2). The demonstrated actuator speed of $33 \text{ pm}/\text{s} = 2 \text{ nm}/\text{min}$ meets that requirement. In vacuum, the actuator input powers will be even lower, since there is no convective heat transport.

For this experimental mirror, the actuators are heated with resistance coils and cooled via convection. In vacuum, contact less heating could be done with a laser. With a dedicated radiative plate cooler, actuation in both directions relative to the environment temperature is possible.

Mirror with axial actuators

This chapter describes the deformation of an EUV mirror with thermo-mechanical actuators placed perpendicular to the surface. Some design models are discussed, and two deformable mirrors (DM) are modeled, realized and validated: one with seven and one with 19 actuators.

4.1 Actuation principle

In most conventional deformable mirrors, the actuators are placed perpendicular to the mirror surface. Mainly three different actuator technologies are used:

- micro machined electro static actuators:
 - Boston Micromachines Corporation [7], with application [59],
 - Iris AO [8],
 - Alpao [9],
 - Flexible Optical B.V. (Okotech) [10],
- stacked piezo ceramic actuators:
 - Cilas [11], with applications [24, 41, 67],
 - Xinetics [12], part of the Northrop Grumman group, with application [62],
- reluctance actuators:
 - Eindhoven University of Technology and TNO [32, 33].

A thin reflective facesheet is connected to an actuator grid. This introduces out of plane forces or displacements to reshape the mirror surface. The grid is supported by a stiff back-structure, normally a few orders stiffer compared to the facesheet. Main advantages of this type of DM's compared to bending moment mirrors (as discussed in ch. 2 and 3), is higher spatial frequency (meaning more actuators per surface area) and a symmetrical actuator influence function with more design freedom in actuator coupling.

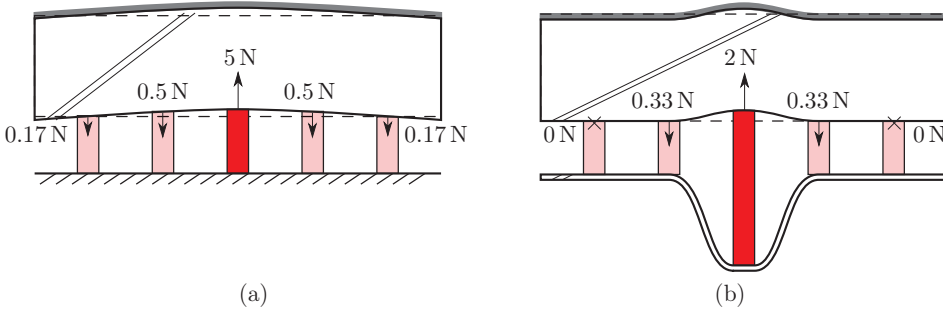


Figure 4.1 / Comparison between a mirror on (a) an infinite stiff back-structure, and (b) a flexible back-plate. Both are a schematic cross section of an FEA result, so the central actuator has 6 direct neighbors.

There are some challenges when using such a conventional grid of actuators under an EUV mirror: the back-structure and the actuator stiffness. A significantly stiffer back-structure is needed to obtain the desired spatial resolution of 20 mm in combination with the desired stroke of 10 nm. Since this support structure is part of the mirror, it also needs to be isolated from its surroundings, and therefore is undesirably a substantial part of the (in this case: magnetically levitated) mirror mass. The limitations of the actuator stiffness are described below, with an example.

Assume an infinitely stiff back-structure and an $h_M = 20$ mm thick ULE mirror. In conventional DM's the mechanical actuator coupling is around 10%, meaning that adjacent actuators displace with 0.1 times the displacement of an energized actuator (for discussion see section 4.2.2). This requires in this case an actuator stiffness above $5 \cdot 10^9$ N/m, using the analytical mirror model described in section 4.2.1. Theoretically, a piezo actuator with that stiffness is 16 mm in diameter and has a length of 1 mm. (Young's modulus is 27 GPa, based on the power actuator product range of PI [6].) This actuator stiffness is the result of the flexural rigidity of the mirror in combination with the actuator pitch (20 mm).

Using actuators comparable to those in the mirrors of chapters 2 and 3 (with a stiffness in the order of $2 \cdot 10^7$ N/m), results in a surface deformation given in figure 4.1(a). This figure is a cross section of a 3D Finite Element Analysis (FEA), where the central actuator in a hexagonal grid has 6 direct neighbors. Equilibrium of the vertical forces is given by $5 \text{ N} \approx 6 \times 0.5 \text{ N} + 12 \times 0.17 \text{ N}$. A high actuator coupling is observed: neighbors displace with 0.6 times the displacement of the central actuator, using zero displacement at the outer actuators as boundary condition.

By using a more flexible back-structure compared to the mirror, the force loop is limited to the neighboring actuators. This result in a local influence of a single actuator as shown in figure 4.1(b). Equilibrium of the vertical forces is given by $2 \text{ N} \approx 6 \times 0.33 \text{ N}$. A drawback of this geometry is the large displacement of the back-structure. So, only

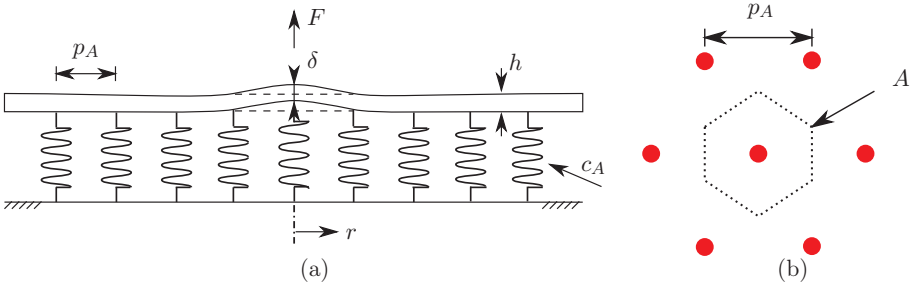


Figure 4.2 / (a) A model of a simply supported facesheet with discrete actuators. (b) Area covered by each actuator, based on a hexagonal configuration.

a percentage of the actuator displacement is used for deforming the mirror surface. On the other hand, this can be used to measure the surface deformation with a lower accuracy on the back-structure, and obtain the mirror surface by a conversion.

After a patent search, patent number US-5986795 has been found, claiming almost the same features including a flexible back-structure and axial actuators. This back-structure can have a constant thickness or a variable thickness, matching the stiffness of the reflecting mirror. Also the correction of EUV light for lithographic purposes is claimed. However, it is decided to continue research on the feasibility and applicability, mainly due to the age of this patent (it is filed on June 15, 1998).

4.2 Analytical mirror model

In this section an analytical thin plate model [70] is derived to support the design process. Also some design considerations are explained for choosing the ratio between mirror and back-plate thickness [26] and choosing the actuator dimensions [25].

4.2.1 Thickness balance between mirror and back-plate

To analyze the relation between actuator stiffness and out of plane stiffness of a plate, an analytical plate model is derived, based on [60].

Assume a facesheet (with thickness h) placed on discrete actuators with a given pitch p_A and stiffness c_A , see Fig 4.2(a). Each actuator covers a given plate area A , as shown for a hexagonal configuration in Fig 4.2(b). The plate theory assumes isotropic material, a constant thickness and small out of plane displacements ($< 0.5h$) based on flexural deformation.

The deflection $\delta(r, \phi)$ of a plate on an elastic foundation with load F , is described by

the biharmonic plate equation [70, p. 260]:

$$\nabla^4 \delta(r, \phi) = \frac{F(r, \phi) - \kappa \delta(r, \phi)}{\mathcal{D}}. \quad (4.1)$$

Using the biharmonic operator ($\nabla^4 = \nabla^2 \nabla^2$, the Laplacian ∇^2 squared) in polar coordinates and using axial symmetry ($\delta(r, \phi) = \delta(r)$) with a central load $F(r = 0)$, the above equation becomes

$$\left(\frac{d^2}{dr^2} + \frac{1}{r} \frac{d}{dr} \right) \left(\frac{d^2 \delta}{dr^2} + \frac{1}{r} \frac{d\delta}{dr} \right) = \frac{F(r) - \kappa \delta(r)}{\mathcal{D}}. \quad (4.2)$$

The flexural rigidity of the plate is given by

$$\mathcal{D} = \frac{Eh^3}{12(1 - \nu^2)}, \quad (4.3)$$

with the Young's modulus E and Poisson's ratio ν . The foundation modulus is approximated by

$$\kappa \simeq \frac{c_A}{A} = \frac{c_A}{\frac{1}{2} \sqrt{3} p_A^2}. \quad (4.4)$$

By introducing the notation

$$\frac{\kappa}{\mathcal{D}} = \frac{1}{\xi^4}, \quad x = \frac{r}{\xi} \quad (4.5)$$

the solution of (4.2), using the Kelvin function [15] (kei) is

$$\delta(r) = \frac{-F\xi^2}{2\pi\mathcal{D}} \text{kei}(x). \quad (4.6)$$

Within MATLAB[®] the Kelvin function can be calculated as:

$$\text{kei}(x) = \frac{\pi}{2} \Im \left\{ \text{bessely} \left(0, x e^{\frac{\pi}{4} i} \right) \right\} - \frac{\pi}{2} \Re \left\{ \text{besselj} \left(0, x e^{\frac{\pi}{4} i} \right) \right\}. \quad (4.7)$$

The maximal deflection under load F and the combined stiffness reads:

$$\delta_{max} = \frac{F\xi^2}{8\mathcal{D}}, \quad c_{\text{plate+act}} = \frac{F}{\delta_{max}} = \frac{8\mathcal{D}}{\xi^2} = 8\sqrt{\kappa\mathcal{D}}. \quad (4.8)$$

The actuator coupling η is defined as the ratio of the faceplate deflection at an immediately adjacent actuator, to the peak deflection of an energized actuator [34]:

$$\eta = \frac{\delta(r = \pm p_A)}{\delta(r = 0)}. \quad (4.9)$$

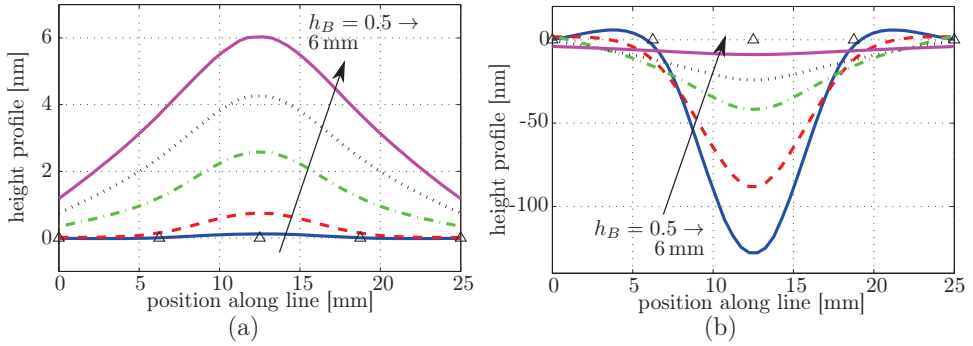


Figure 4.3 / FEA cross sections for different back-plate thicknesses: $h_B = 0.5, 1, 2, 3$ and 6 mm. In (a) the mirror and in (b) the back-plate response.

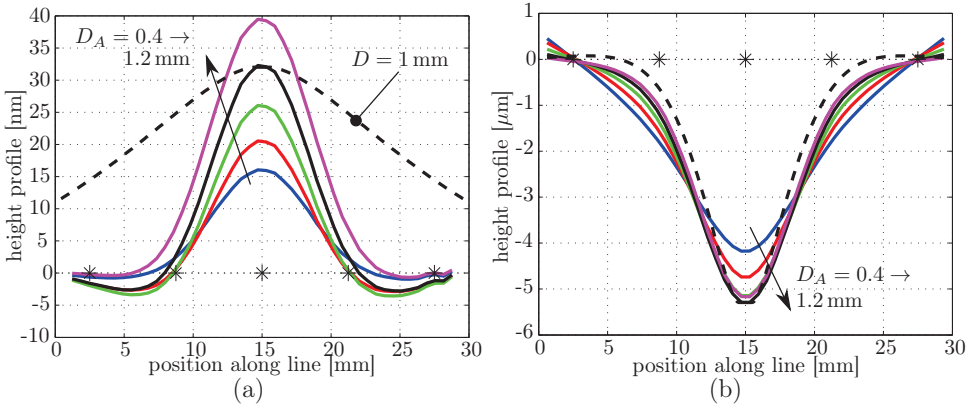


Figure 4.4 / FEA cross sections for different actuator diameters: $D_A = 0.4, 0.6, 0.8, 1$ and 1.2 mm. In (a) the mirror and in (b) the back-plate response.

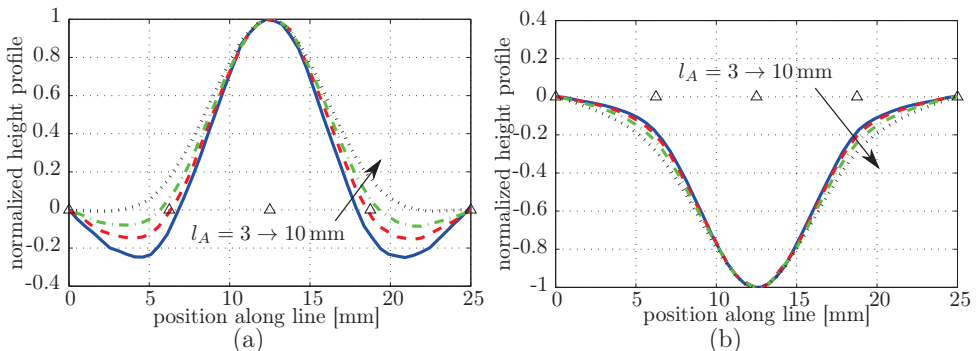


Figure 4.5 / Normalized FEA cross sections for different actuator lengths: $l_A = 3, 4, 6$ and 10 mm. In (a) the mirror and in (b) the back-plate response.

4.2.2 Selecting mirror and actuator dimensions

In this subsection the design considerations are explained using the deformable mirror with 19 actuators as an example. To use this mirror in an optical setup, 19 actuators are placed inside the beam diameter of 25 mm.

Based on the model described in the previous subsection and based on the availability of mirrors, the thickness is chosen as $h_M = 6$ mm. The back-plate thickness is varied between $h_B = 0.5 \rightarrow 6$ mm and the surface responses are calculated using Finite Element Analyzes (FEA, see also appendix C). In a structural solver these parameters are used: Fused Silica as mirror and back-plate material (see appendix A), aluminum 6082 as actuator material, actuator diameter $D_A = 1$ mm and actuator length $l_A = 6$ mm. In all cases the temperature of the central actuator is set to $T_A = 23^\circ\text{C}$, with an ambient temperature of $T_\infty = 22^\circ\text{C}$. In figure 4.3(a) different cross sections of the mirror surface are shown for back-plate thicknesses between $h_B = 0.5 \rightarrow 6$ mm. In Fig. 4.3(b) the back-plate responses are shown. With increasing back-plate thickness, the responses become more similar, where at the same time the actuator coupling increases. The actuator coupling is $\eta \approx 10\%$ at the combination of $h_M = 6$ mm and $h_B = 1$ mm, resulting in an optimal actuator influence function [34, p. 187-192].

Also the actuator dimensions are analyzed using FEA. In figure 4.4 the actuator diameter is varied between $D_A = 0.6 \rightarrow 1.2$ mm. In the figure also the analytical solution ($D_A = 1$ mm) is shown with a dashed line, using (4.6). For all simulations, the heat flow into the actuator is constant. Natural convection coefficients of mirror, back-plate and actuators are calculated using the equations given in section 2.3.5. By comparing the different influence functions, an actuator diameter of $D_A = 1$ mm is chosen as an optimum of actuator response and actuator coupling.

In figure 4.5 the actuator length is varied. Again, using a constant heat flow into the actuator. All height profiles are normalized for better comparison. Altering the actuator length result in a different coupling between mirror and back-plate, changing the shape of the influence function. A length of $l_A = 6$ mm is chosen.

In conclusion, the shape of the influence function is mainly dependent on the thickness ratio between mirror and back-plate. Fine tuning is done with actuator diameter and length.

4.3 Realization

To investigate the actuation principle, a first experimental deformable mirror is realized using available optics. Seven actuators are equipped with joule heating coils and thermocouples. Based on its good results a second DM is realized with 19 actuators

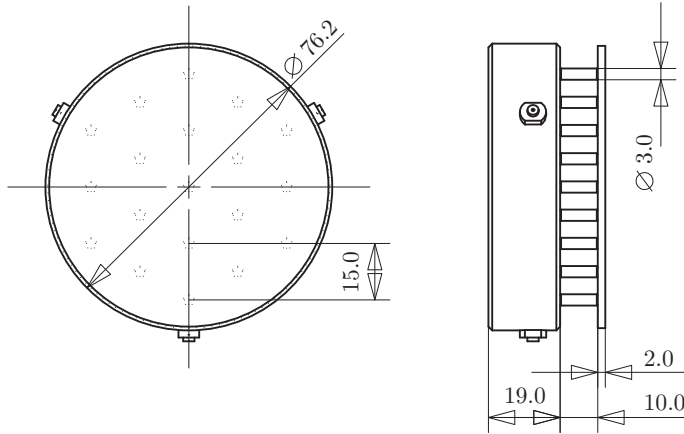


Figure 4.6 / Mirror with 7 actuators and 12 passive rods, thus 19 in total (drawing scale 1:2).

and five thermocouples.

4.3.1 DM with 7 actuators

For the mirror a commercial precision fused silica optical flat from Edmund Optics Ltd.[™] is used. Its surface accuracy is $\lambda/4$, and it is coated with enhanced aluminum. Diameter is $D_M = 76.2\text{ mm}$ (3") and thickness $h_M = 19.1\text{ mm}$. Based on that mirror the back-plate and actuator dimensions are chosen according to the method of the previous section. As back-plate a $h_B = 2\text{ mm}$ thick fused silica window is used with a diameter of $D_B = 75\text{ mm}$ from UQG-optics[™]. Aluminum 6082 actuators are used with length $l_A = 10\text{ mm}$ and diameter $D_A = 3\text{ mm}$ in an actuator pitch of $p_A = 15\text{ mm}$. The dimensions are shown in figure 4.6. The outer ring of actuators are passive, meaning that no joule heating coils are attached.

Figure 4.7 shows the mirror with its connectors and base structure. The assembly is made by first gluing the actuator rods to the mirror using a jig. The joule heating coils are pre-wound on a dummy and placed on the glued rods. Then the thermocouple leads are fixed on the mirror with the tip in contact with the aluminum rods, using heat conducting paste to seal that contact. For the joule heating coils a D-SUB-15 connector is used. The seven thermocouples are connected via dedicated copper terminals to exclude the material transition error. The temperature of the cold junction is measured independently using a platinum sensor (Pt100). The mirror is connected to the base structure via three aluminum fixation pins. To minimize the influence of glue shrinkage, the pin is first glued axially onto the mirror and then into an integrated 1 mm thick leaf spring of the base structure. After testing the joule heating and the thermocouple

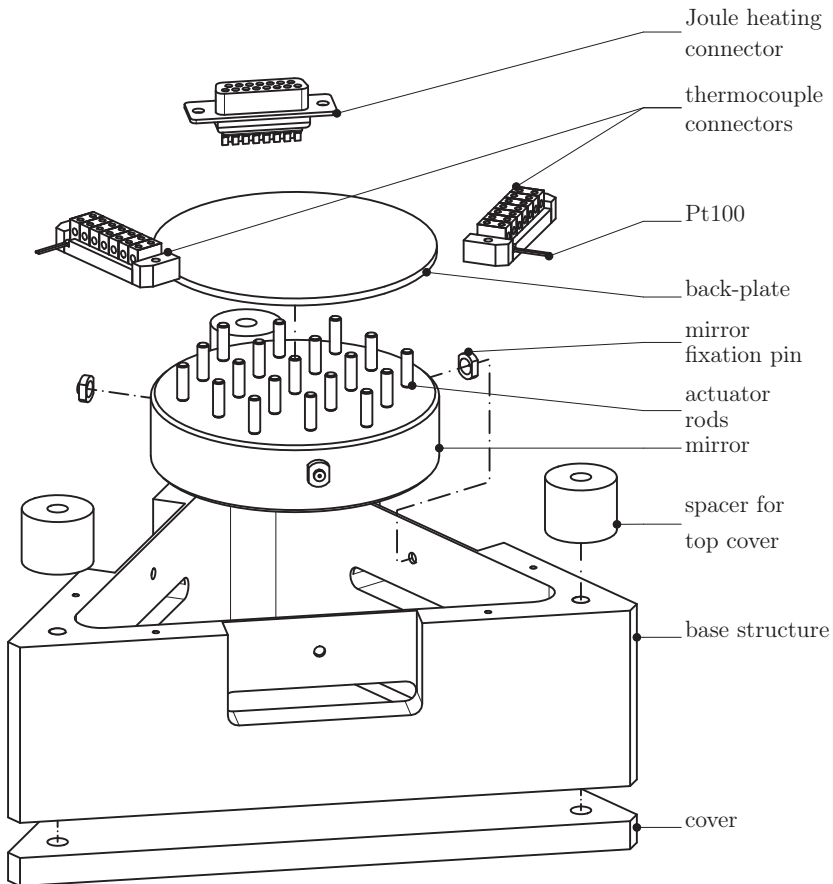


Figure 4.7 / Exploded view of the deformable mirror with 7 actuators and 12 passive rods. The base structure is an equilateral triangle with sides of 170 mm and the total height of the assembly, including covers is 80 mm (drawing scale 1:2).

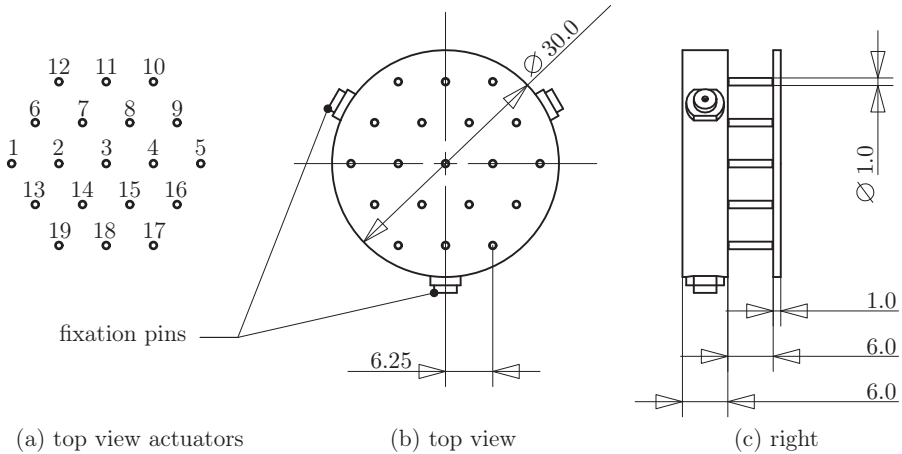


Figure 4.8 / Mirror with 19 actuators. Actuators #1 → 5 are equipped with thermocouples (drawing scale 1:1).

connections, the back-plate is glued onto the actuator rods. When not in use and during transport, the mirror is protected with two cover plates.

4.3.2 DM with 19 actuators

Based on the promising results of the DM with 7 actuators, a DM with 19 actuators is built. The previous concept is scaled to a smaller aperture (25 mm) to fit into the realized optical setup.

The dimensions are shown in figure 4.8. Mirror diameter is $D_M = 30$ mm and the thickness $h_M = 6$ mm. It is a commercial Fused Silica mirror from CVI Melles Griot™. The actuator pitch is $p_A = 6.25$ mm with length $l_A = 6$ mm and diameter $D_A = 1$ mm (aluminum 6082). A matching base-plate thickness of $h_B = 1$ mm is calculated, as explained in section 4.2.2.

Before gluing the mirror surface has a measured surface accuracy of $\lambda/90$ (6 nm Peak to Valley) within the 25 mm aperture, see figure 4.9(a). This figure shows a piston, tip and tilt corrected laser interferometer surface. The height values in the color-bar are in nm and the intersection at $z = 0$ is drawn as contour-line. The horizontal and vertical axis are the absolute positions on the surface in mm. The data is cropped 3 mm to exclude the edge. Through the surface, three cross sections are made at the lines: solid (from left to right), dashed (top→bottom) and dash-dotted (bottom→top). These are shown in the figure 4.9(b). The horizontal axis is the corresponding position along the section line. Also the actuator locations are shown with triangles.

The surface shape after gluing is shown in figure 4.9(c) with a PV of 23 nm (4 nm rms).

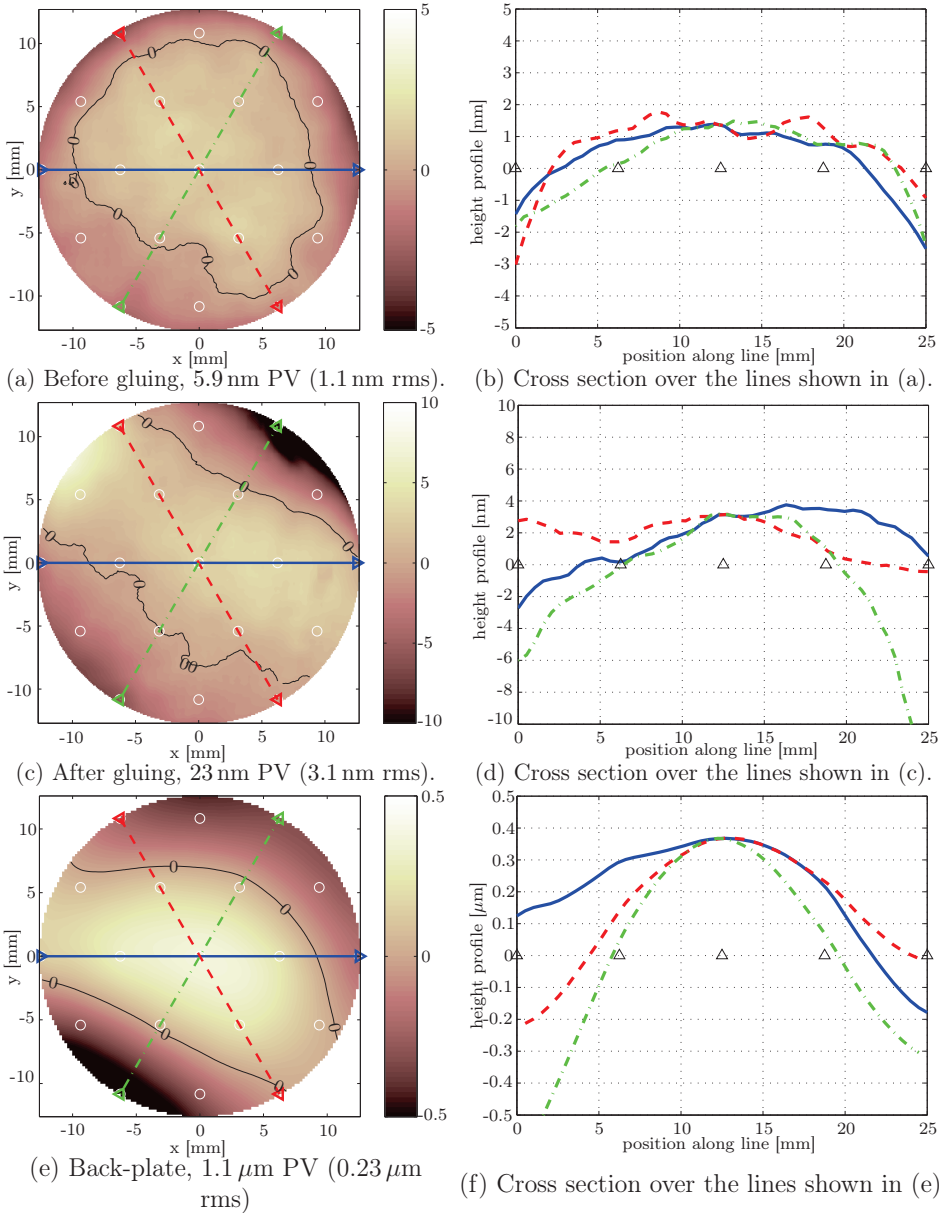


Figure 4.9 / Mirror front surface data obtained with a Zygo[®] interferometer: (a) before gluing the actuators, (c) after gluing. In (e) the back-plate surface is shown in μm . Peak to valley (PV) and rms values are in a 25 mm circular pupil. On the right, corresponding averaged cross sections (b,d and f).

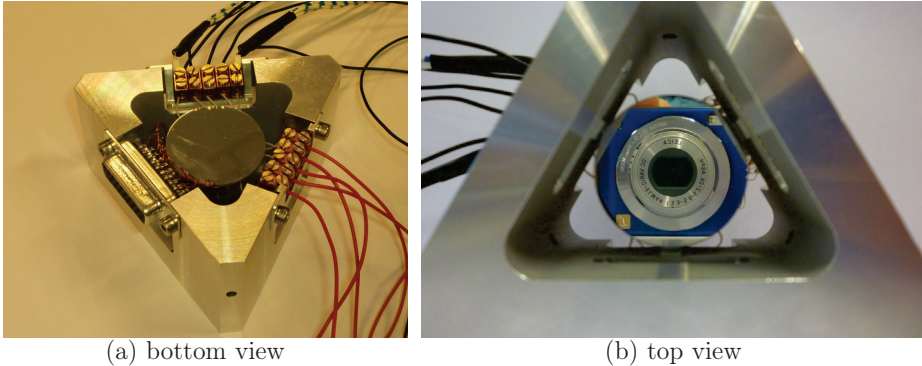


Figure 4.10 / Mirror with 19 actuators. In (a) the back-plate, the joule heating connector, the copper thermocouple connectors and two Pt100 sensors (close to the top of the picture) for the cold junction compensation. In (b) the mirror inside its enclosure.

Possible reasons for the difference with the initial surface besides glue shrinkage and actuator length are different measurement and curing temperatures. Corresponding back-plate shape is shown in figure 4.9(e) with a PV of almost $1\ \mu\text{m}$ ($0.23\ \mu\text{m rms}$). To improve the results on the optical setup, some flattening can be performed. A straightforward method to do this is by multiplying the pseudo-inverse of a measured influence matrix with the reverse of this surface. This gives the actuator inputs that result in a best flat.

Thermocouples are attached to the actuators #1 to 5. These are fine gauge copper-constantan (Type-T) wires with a diameter of $75\ \mu\text{m}$. All 19 actuators are equipped with joule heating coils: 20 turns of Isotan[®] copper-nickel (44% Ni) wire with $100\ \mu\text{m}$ diameter. The transition from joule heating wire to copper enameled wire is made close to the aluminum actuator via laser spot welding. The joule heating connector on the DM is a D-Sub-26 (high density). Measured resistance between the connector pins of the joule heating coils is $5.7 \pm 0.1\ \Omega$.

Figure 4.10(a) shows a realized partially connected deformable mirror. In the center the coated back-plate is visible, at the lower left the joule heating connector. At the top, the copper connector for the five constantan thermocouple leads with two thin film Platinum 100 sensors. To the right, the connector for the five copper leads is visible. The top view in figure 4.10(b) shows the mirror inside its enclosure.

4.4 Validation

Since the DM with 7 actuators is used to prove the concept, only a few measurement results are discussed. Main focus in the discussion is on the results of the mirror with

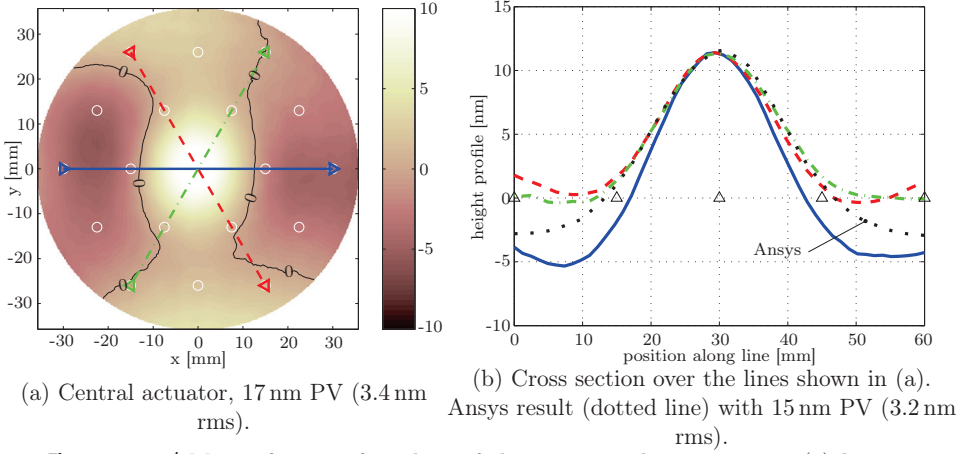


Figure 4.11 / Mirror front surface data of the mirror with 7 actuators: (a) heating the central actuator with 645 mW (3 V), Peak to valley (PV) and rms values are in a 70 mm circular pupil. On the right the corresponding averaged cross section (b).

19 actuators.

The surfaces are measured with a Zygo[®] interferometer and are further analyzed using MATLAB[®]. The raw Zygo data is linearly mapped on a rectangular grid using `griddata` and averaged with `imfilter` over 12×12 pixels ($\approx 0.5 \times 0.5$ mm). The data is also compensated for piston, tip and tilt using singular value decomposition. Peak to valley (PV) values are taken from that data set, the root mean square (rms) values are calculated via

$$z_{\text{rms}} = \sqrt{\frac{1}{n} (z_1 + z_2 + \dots + z_n)}, \quad (4.10)$$

where n is the total amount of measured points z . The averaged inter-actuator stroke $\bar{\delta}$ is defined as the difference between the energized actuator and the average of its adjacent actuators. Using the actuator numbering of figure 4.8(a) and energizing actuator #3, it reads:

$$\bar{\delta}_{\text{act}3} = \delta_{\text{act}3} - 1/6 \cdot \sum_{i=2,4,7,8,14,15} \delta_{\text{act} i} \quad (4.11)$$

4.4.1 DM with 7 actuators

Figure 4.11 shows the relative surface of heating the central actuator with 645 mW (3.03 V). Corresponding temperature difference is 24.3°C. A peak to valley of 17 nm (3.4 nm rms) is measured, with an averaged inter-actuator stroke of 11 nm (eq. 4.11).

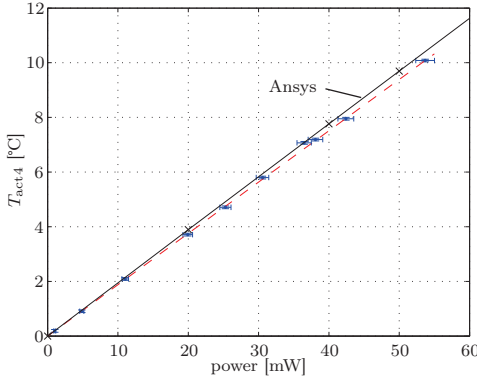


Figure 4.12 / Steady state actuator temperature (DM with 19 actuators) as function of the heat input. Fitted relation is: $T_{\text{act}4} = 0.19 \cdot P_{\text{act}4}$, the Ansys relation is $T_{\text{act}4} = 0.194 \cdot P_{\text{act}4}$

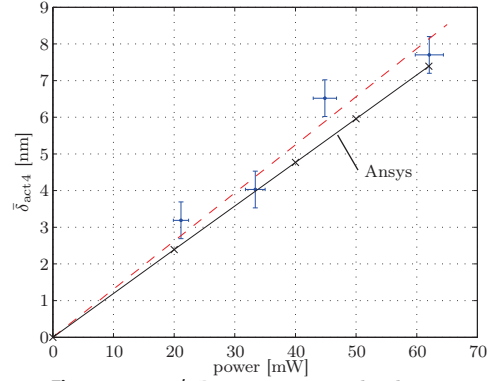


Figure 4.13 / Inter-actuator displacement as function of the heat input. Fitted relation is: $\bar{\delta}_{\text{act}4} = 0.13 \cdot P_{\text{act}4}$, the Ansys relation is $\bar{\delta}_{\text{act}4} = 0.119 \cdot P_{\text{act}4}$.

Fitting the heating response with

$$T_A(t) = c_1 (2 - \exp(t/\tau_1) - \exp(t/\tau_2)), \quad (4.12)$$

results in the characteristic heating constants $\tau_1 = 12.9\text{ s}$ and $\tau_2 = 650\text{ s}$. Fitting the convection cooling gives $\tau_1 = 7.7\text{ s}$ and $\tau_2 = 25\text{ s}$. These give an indication of the actuator speed.

4.4.2 DM with 19 actuators

Figure 4.12 shows the measured steady state temperature of actuator #4 versus inserted power. Steady state is reached $\approx 50\text{ s}$ after switching on the joule heating. Measurement uncertainties are:

$$T_{\text{act}4} \pm 0.05^\circ\text{C} \quad V_{\text{act}4} \pm 0.005\text{ V} \quad R_{\text{act}4} \pm 0.1\ \Omega, \quad (4.13)$$

these are recalculated to a power uncertainty as:

$$\Delta P = \sqrt{|\Delta V|^2 \left(2 \frac{V}{R}\right)^2 + |\Delta R|^2 \left(\frac{V^2}{R^2}\right)^2}.$$

Also a fit is shown (dashed line) with $0.190 \pm 0.005^\circ\text{C}/\text{mW}$. The solid line is the FEA result obtained with Ansys: $0.194^\circ\text{C}/\text{mW}$. In figure 4.13 the inter-actuator stroke (eq. 4.11) at four different input powers on actuator #4 is shown. The fitted relation (dashed line)

is $0.13 \pm 0.02 \text{ nm/mW}$, the FEA relation (solid line) is 0.119 nm/mW . For this measurement set, also the heating and cooling temperature responses are fitted using (4.12). The characteristic heating time constants are $\tau_1 = 2.6 \pm 0.2 \text{ s}$ and $\tau_2 = 8.5 \pm 0.2 \text{ s}$, and for cooling: $\tau_1 = 2.3 \pm 0.1 \text{ s}$ and $\tau_2 = 9.0 \pm 0.2 \text{ s}$.

Figure 4.14(a) shows the relative mirror surface when heating the central actuator (#3) with 62 mW (0.60 V). In this piston, tip and tilt corrected image, the heights are in nm. The drawn contour-line is the intersection at $z = 0 \text{ mm}$. An almost symmetrical influence function is observed with 11.5 nm peak to valley (PV) and an averaged inter-actuator stroke of $\bar{\delta}_{\text{act}3} = 6.9 \text{ nm}$ (eq. 4.11). A perfect symmetrical influence function would result in an circular contour-line. Figure 4.14(b) shows three cross-sections over the lines shown in (a): solid (from left→right), dashed (top→bottom) and dash-dotted (bottom→top). The measured actuator coupling is $\eta = 30\%$, using as boundary zero deflection at the outer actuators (add 1 nm of piston to the whole surface). This coupling is a combination of the mechanical and the thermal coupling.

In figure 4.14(c and d) the FEA result is shown, with the same heat input: 7.1 nm PV and 6.1 nm averaged inter-actuator stroke. The actuator coupling is $\eta = 9\%$, assuming zero deflection at the outer actuators. The influence function is symmetrical since the contour-line in (c) is circular and the cross-sections in (d) are identical.

Figure 4.14(e) shows the measured relative (solid line) and simulated (dashed line) temperature as function of time. At $t \approx 0 \text{ s}$ a reference surface measurement is done. The actuator temperatures between $t = 0 \text{ s}$ and $t = 25 \text{ s}$ are averaged and used as initial condition. The joule heating is switched on at $t = 30 \text{ s}$ and switched off at $t = 90 \text{ s}$. Another surface measurement is done at $t \approx 85 \pm 3 \text{ s}$. Temperatures at the measurement are $T_{\text{act}3} = 11.88 \pm 0.05 \text{ }^\circ\text{C}$, $T_{\text{act}2} \approx T_{\text{act}4} = 0.71 \pm 0.05 \text{ }^\circ\text{C}$ and $T_{\text{act}1} \approx T_{\text{act}5} = 0.16 \pm 0.05 \text{ }^\circ\text{C}$. Fitting the actuator heating using (4.12) gives $\tau_1 = 4.2 \text{ s}$ and $\tau_2 = 450 \text{ s}$. The cooling gives $\tau_1 = 2.6 \text{ s}$ and $\tau_2 = 9.2 \text{ s}$.

Figure 4.15 shows the mirror surface while heating an edge actuator (#1) with 62 mW (0.60 V). Analyzing the data is somewhat different due to the piston, tip and tilt compensation. The raw Zygo data contains $150 \mu\text{m}$ piston, $10 \mu\text{m}$ peak to valley tip and $20 \mu\text{m}$ PV tilt. Also the tilt component introduced by the actuator is compensated. The calculated peak to valley is 15.0 nm and the averaged inter-actuator stroke is $\bar{\delta}_{\text{act}1} = 11.4 \text{ nm}$. A clearer view is shown in the FEA result of Fig. 4.15(c and d) where the raw data is shown. Resulting in a 18.1 nm PV and 13.3 nm averaged inter-actuator stroke. Fig. 4.15(e) shows the measured relative and simulated temperature. Surface measurement is done at $t \approx 80 \text{ s} \pm 3 \text{ s}$. Temperatures at the measurement are $T_{\text{act}1} = 12.45 \pm 0.05 \text{ }^\circ\text{C}$, $T_{\text{act}2} = 0.88 \pm 0.05 \text{ }^\circ\text{C}$, $T_{\text{act}3} = 0.12 \pm 0.05 \text{ }^\circ\text{C}$ and $T_{\text{act}4} \approx T_{\text{act}5} = 0 \pm 0.05 \text{ }^\circ\text{C}$. Fitting the actuator heating using (4.12) gives $\tau_1 = 3.0 \text{ s}$ and $\tau_2 = 12 \text{ s}$. The cooling gives $\tau_1 = 2.8 \text{ s}$ and $\tau_2 = 13 \text{ s}$.

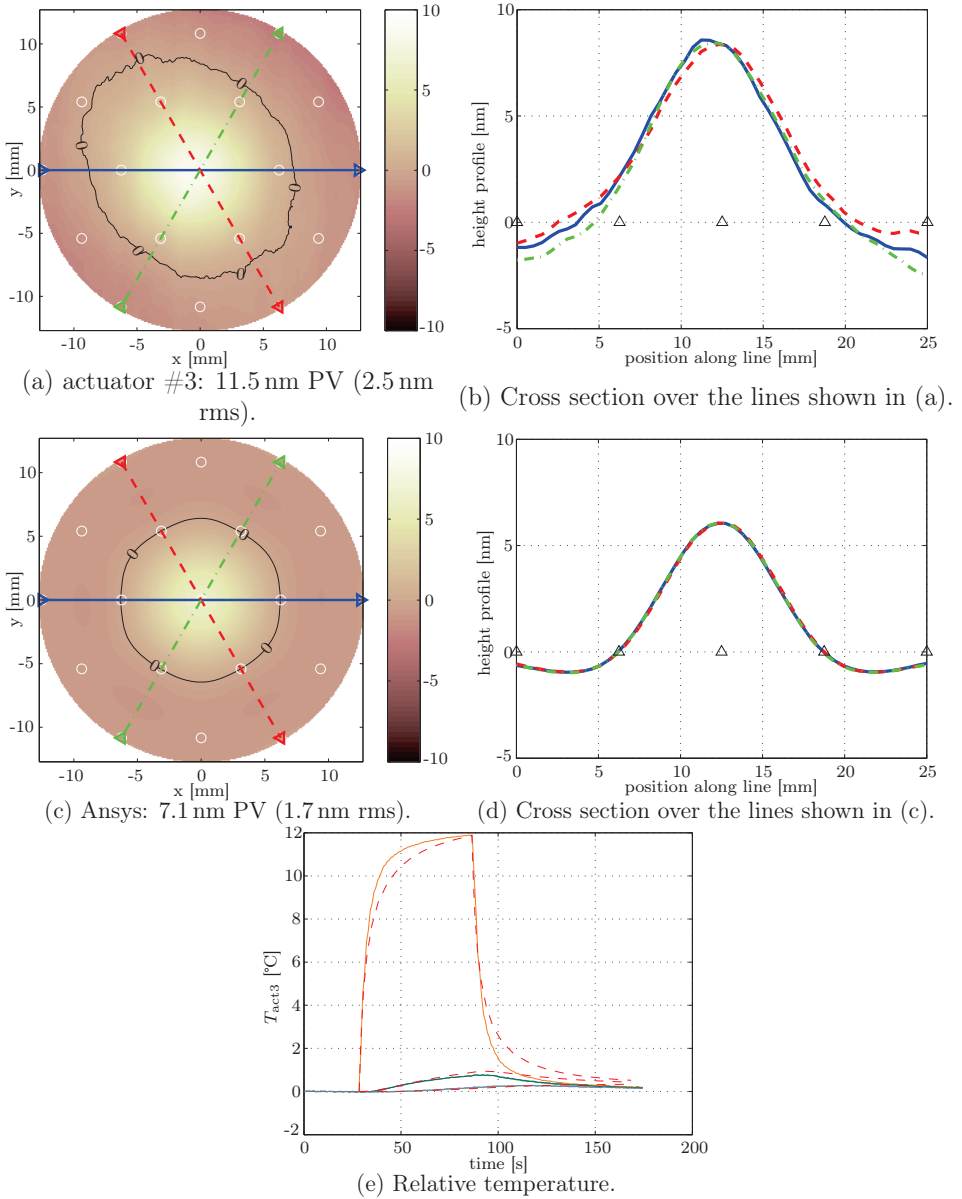


Figure 4.14 / Relative surfaces with cross sections of a Zygo measurement and an Ansys simulation while heating actuator #3 with 62 mW (0.60 V)

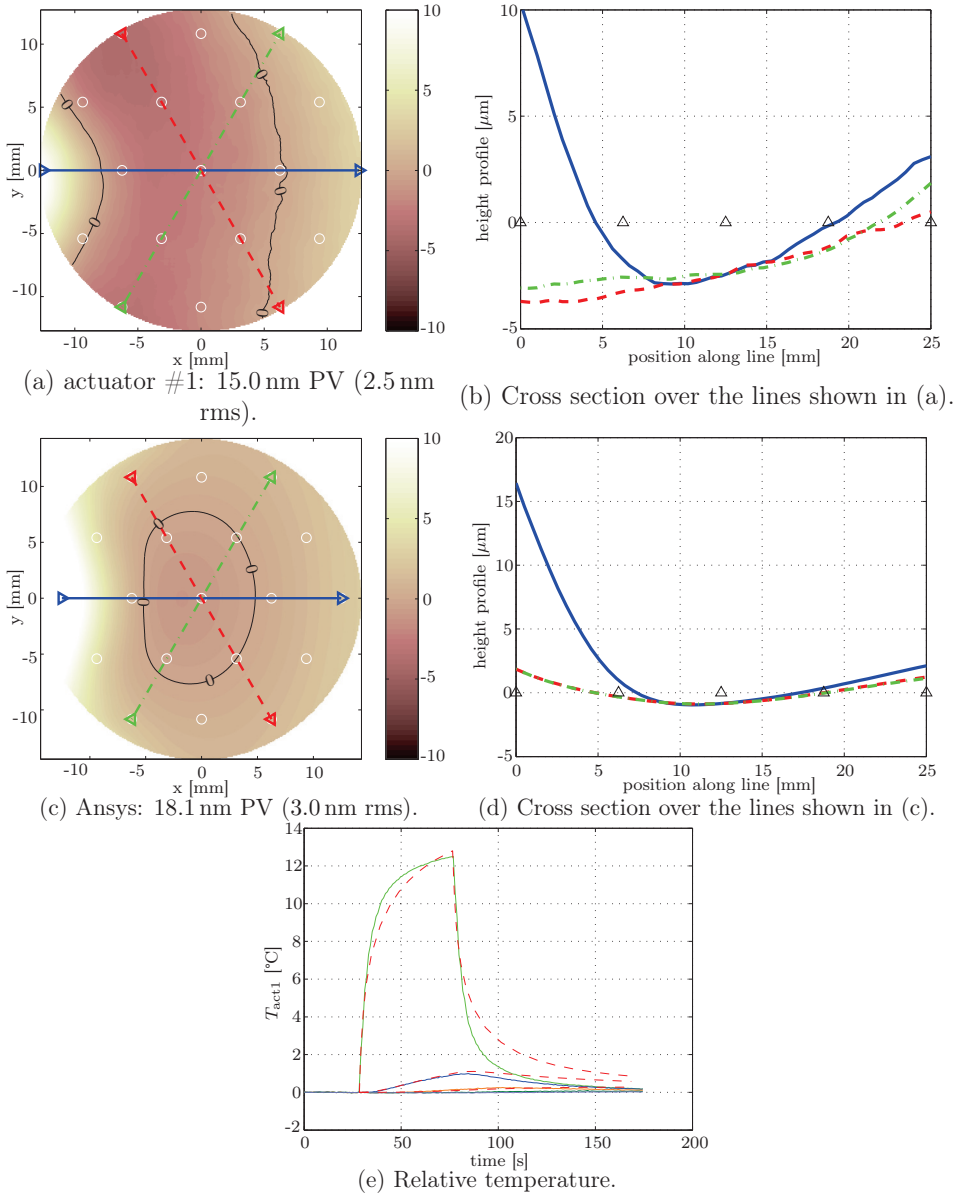


Figure 4.15 / Relative surfaces with cross sections of a Zygo measurement and an Ansys simulation while heating actuator #1 with 62 mW (0.60 V)

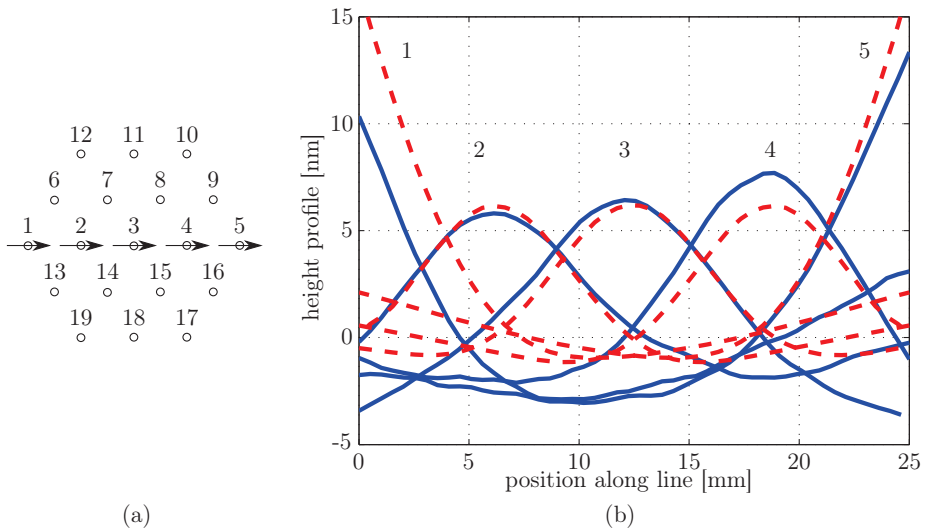


Figure 4.16 / Comparison of the cross sections between measurement (solid line) and Ansys (dashed line). From left to right: actuator 1, 2, 3, 4 and 5.

Figure 4.16(b) shows the cross sections over actuator #1, 2, 3, 4 and 5 with a solid line, the dashed line is the Ansys result. Actuators #2 and 4 differ ca. 1 nm from FEA. The large difference of actuators #1 and 5 is mainly due to the tip-tilt correction on the raw Zygo data, as discussed earlier. The central actuator #3, differs 2 nm from FEA. Corresponding positive direction is shown in Fig. 4.16(a).

Figure 4.17 shows the measured influence functions for all actuators and shows that they are all functional. The figure is a combination of three times one hour measuring in the thermally controlled room, followed by approximately two weeks to complete the data processing.

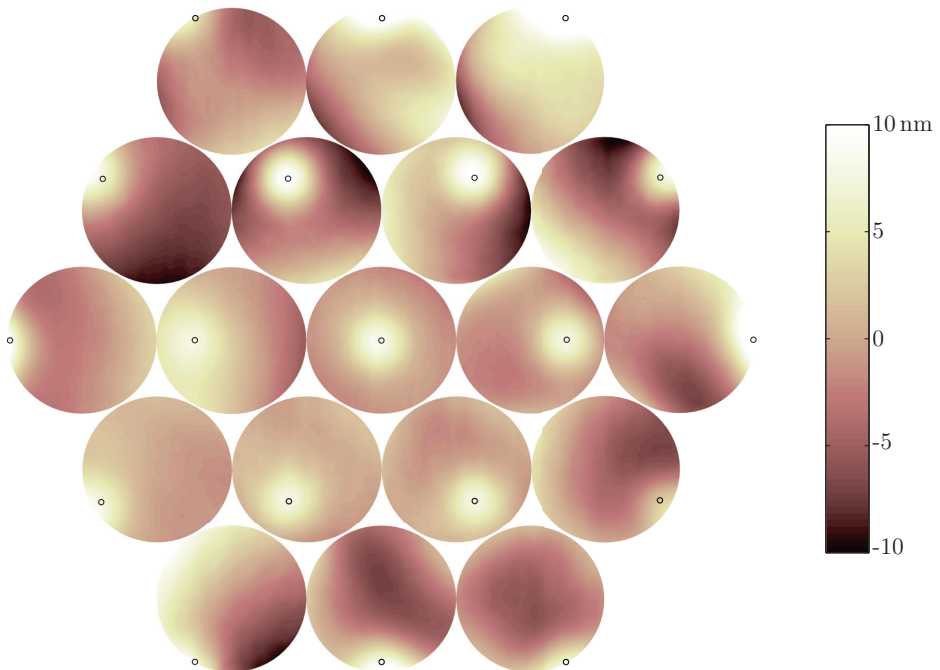


Figure 4.17 / Measured influences, each surface is downsized and placed on the location of the corresponding actuator in the grid shown in Fig. 4.16(a).

Table 4.1 / Specifications deformable mirror with 7 actuators, dimensions in mm. Material properties are given in Appendix A.

| | | |
|------------------------|---|---|
| mirror | material thickness diameter | fused silica $h_M = 19.1$ $D_M = 76.3$ |
| back-plate | material thickness diameter | fused silica $h_B = 2.0$ $D_B = 75.0$ |
| actuator | material length diameter pitch | aluminum 6082 $l_A = 10.0$ $D_A = 3.0$ $p_A = 15.0$ |
| central actuator (fit) | mirror deflection inter-actuator stroke joule heating | 17 nm at 645 mW 11 nm at 645 mW $0.040 \pm 0.002 \text{ } ^\circ\text{C}/\text{mW}$ |

4.5 Conclusion and discussion

Two experimental mirrors are modeled, realized and tested. One with 7 and one with 19 actuators. Since the first one is used as concept demonstrator, the latter one is described and measured in more detail. Resulting specifications are summarized in tables 4.1 and 4.2.

The results obtained from the DM with 7 actuators, show a mirror deflection of 17 nm at 645 mW inserted actuator heat and an inter-actuator stroke of 11 nm. So, this actuation principle works and therefore it is implemented in a smaller deformable mirror with 19 actuators inside a 25 mm beam diameter.

A linear relation between actuator power and temperature (Fig. 4.12: $0.190 \pm 0.005 \text{ } ^\circ\text{C}/\text{mW}$) and between power and averaged inter-actuator stroke (Fig. 4.13: $0.13 \pm 0.02 \text{ nm}/\text{mW}$) is validated. So, the successfully realized mirror deflection is $0.68 \text{ nm}/^\circ\text{C}$ and no hysteresis is observed.

Thermal step responses are fitted and both heating and cooling characteristic time constants are around 2.5 s. The thermal actuator coupling from actuator #3 to #2 and 4 is $6.0 \pm 0.1\%$, and to #1 and 5 it is $1.3 \pm 0.1\%$.

Comparing the mechanical actuator coupling, there is a large difference between the measurement (30%) and FEA (9%). A contribution to this difference is that the coupling is based on absolute values: the ratio between adjacent and energized actuator. So, for example, a piston component will alter that coupling. However, the difference of the inter-actuator stroke is small between measurement (6.9 nm) and simulation (6.1 nm).

Reconsidering the active mirror requirements stated in table 1.2, the desired actuator stroke (10 nm) with an actuator pitch of 20 mm and an inter-actuator coupling of 10 –

Table 4.2 / Specifications deformable mirror with 19 actuators, dimensions in mm.
Material properties are given in Appendix A.

| | | |
|-----------------------|--|--|
| mirror | material thickness diameter | fused silica $h_M = 6.0$ $D_M = 30.0$ |
| back-plate | material thickness diameter | fused silica $h_B = 1.0$ $D_B = 30.0$ |
| actuator | material length diameter pitch | aluminum 6082 $l_A = 6.0$ $D_A = 1.0$ $p_A = 6.25$ |
| actuator #4 (fit) | inter-actuator stroke joule heating heating time constants cooling time constants | $0.13 \pm 0.02 \text{ nm/mW}$ ($0.68 \pm 0.05 \text{ nm/}^\circ\text{C}$) $0.190 \pm 0.005 \text{ }^\circ\text{C/mW}$ $\tau_1 = 2.6 \pm 0.2 \text{ s}$ $\tau_2 = 8.5 \pm 0.2 \text{ s}$ $\tau_1 = 2.3 \pm 0.1 \text{ s}$ $\tau_2 = 9.0 \pm 0.2 \text{ s}$ |
| central actuator (#3) | actuator coupling | $\eta = 30\%$ |
| FEA | actuator coupling inter-actuator stroke joule heating | $\eta = 9\%$ 0.119 nm/mW ($0.61 \text{ nm/}^\circ\text{C}$) $0.194 \text{ }^\circ\text{C/mW}$ |

15% is feasible with the deformable mirror technology described in this chapter. Based on the design strategy derived in section 4.2.2, the design is scalable toward other combinations of actuator pitch and mirror thickness. This scaling is validated with the downscaling from the 76.3 mm mirror diameter, to the 30 mm mirror.

Conclusions and recommendations

In the production of integrated circuits (e.g. computer chips), optical lithography is used to transfer a pattern onto a semiconductor substrate (wafer). For lithographic systems using light in the ultraviolet band (EUV) with a 13.5 nm wavelength, only reflective optics with multi-layers can reflect that light by means of interlayer interference, but these mirrors absorb around 30% of the incident light. Depending on pattern and beam shape, there is a nonuniform light distribution over the surface of the mirrors. This causes temperature gradients and therefore local deformations, due to thermal expansions. To improve the throughput (wafers per hour), there is a demand to increase the source power, that will increase these deformations even further. Active mirrors are a solution to correct for these deformations by reshaping the surface. A research collaboration is formed to examine this technique in detail on: overall system design, control methodology, metrology and active mirror design.

This thesis presents the design and validation of two deformable mirror concepts in four experimental mirrors that are suitable for extreme ultraviolet lithography. Accurate deformation with high repeatability is demonstrated, meeting the requirements for implementation. The specifications for the projection mirrors are derived, based on simulations and measurements on current EUV systems. These are formulated by the semiconductor industry and form the basis for this research. Preferably, the concepts are applicable to current mirrors with little effort and only small adaptations. The desired spatial frequency, determined by the actuator spacing, is 20 mm. These actuators should deform the surface by 1 nm over 1 min, 5 nm over 1 h and 10 nm over the lifetime (7y), with a hysteresis below 5% at full stroke. Typical desired actuator coupling is 10 – 15%, meaning that an adjacent actuator translates with that percentage of the energized one. In conventional deformable mirrors, this coupling results in the desired optical performance (influence function) and control performance. Since the illumination is done in vacuum, (potential) compatibility is required. Each projection mirror is magnetically suspended, so the added stiffness from base to mirror (e.g. by wires) should be minimized. It should be at least be below 100 N/m (perpendicular to the surface) and below 1000 N/m in plane.

5.1 Conclusions

Two different deformable mirror concepts are investigated, both using thermo-mechanical actuators. In one, the actuators are placed in a bending moment configuration and in the other, they are placed perpendicular to the surface to axially deform it. Four deformable mirrors are successfully designed, realized and validated.

Actuation by thermo-mechanical actuators is chosen over other actuation principles due to its low hysteresis and creep, high force to volume ratio, possibility for contact-less control using radiation and/or laser heating.

5.1.1 Bending moment deformable mirrors

An advantage of bending moment actuators is that they are integrated as an additional layer on the back-side of a mirror, so there is no need for a reference structure. In this application, the actuators are placed between posts. A model is derived to optimize the spatial frequency by investigating the effect of actuator placement (e.g. the distance from mirror neutral axis to actuator). Its outcome is, that an optimal balance between deformation and spatial frequency exists, given a mirror thickness.

Based on the modeling results, a first experimental mirror with one bending actuator is successfully built and tested. To obtain large mirror deflection at a given inserted actuator power, aluminum is chosen as the actuator material. The mirror is made from Zerodur[®] like the mirrors in the first EUV lithographic demonstration machines. A mirror deformation of $4.7 \text{ nm}/^\circ\text{C}$ is achieved, where the inserted actuator power is $0.044 \text{ }^\circ\text{C}/\text{mW}$, meaning $0.21 \text{ nm}/\text{mW}$. The measurements are obtained in a thermally controlled room; in vacuum the actuator input power will be 40% lower, since there is no convective heat transport. The shape and amplitude of the mirror are measured and agree with the prediction from the analytical model. The measured characteristic time constant is 10 s, meaning that for a given input, 63% of the steady state stroke is reached within that time scale. All values are close to the predicted ones from the models and meet the requirements for implementation.

To further investigate the concept and to measure the mechanical and thermal actuator coupling, an experimental mirror with four actuators is designed, realized and validated. It is an extension of the mirror with one actuator. To approach the sizes of current EUV mirrors inside a lithography projection system, this geometry can be extended toward larger mirrors with more actuators. An optimized mounting is realized with minimal thermal drift and low surface deformation caused by temperature variations between mirror and mounting.

In a single actuator step-response, a mirror deflection of $3.4 \text{ nm}/^\circ\text{C}$ is achieved. This value is lower compared to the mirror with one actuator, since the deformed mirror surface

is larger. A design optimization is proposed and successfully tested which reduces the actuator coupling from 30% to 10%. However, the mirror deflection at the same input is reduced to 55%.

Actuator speed is demonstrated while simultaneously heating all actuators with 3 mW, which correspond with a mirror deformation of 33 nm/s. When using an adaptive mirror in an EUV lithography system, actuator strokes of 1 nm/min are required. The demonstrated actuator speed of 33 nm/s = 2 nm/min meets that requirement.

5.1.2 Deformable mirrors with axial actuators

In conventional deformable mirrors with axial actuators, a stiff back structure is used to support and align the actuators. The stiffness ratio between mirror plate, actuators and back structure determines the spatial frequency. However, compared to the mirror thickness, this application requires a small stroke at a high spatial frequency. By placing the actuators on a thin back plate, the force loop is localized and therefore a lower actuator coupling is achieved.

Two experimental mirrors are successfully modeled, realized and tested. The results obtained from the first mirror with 7 actuators are close to the predicted values from the static and thermal models. Based on these good results, this actuation principle is implemented in a smaller deformable mirror with 19 actuators inside a 25 mm beam diameter. A linear relation between actuator power and temperature of 0.190 °C/mW and between power and averaged inter-actuator stroke of 0.13 nm/mW is achieved. So, the successfully realized mirror deflection is 0.68 nm/°C and no hysteresis is observed. For both mirrors a support frame is developed, that minimizes introduced surface deformations by temperature variations.

Thermal step responses are fitted and both heating and cooling characteristic time constants are 2.5 s. The thermal actuator coupling from an energized actuator to its direct neighbor is $6.0 \pm 0.1\%$, to their neighbors it is $1.3 \pm 0.1\%$. Based on the good agreement between simulated and measured inter-actuator stroke, the total actuator coupling is approximated around 10%.

5.1.3 Comparison

Both mirror concepts meet the requirements for implementation into a lithography machine. Actuator speeds correspond well to the desired 1 nm per min. The actuator spacing (spatial frequency) in combination with a desired mirror deflection is demonstrated successfully. The actuators in a bending moment configuration, result in a larger deflection (3.4 nm/°C) compared to the axial placed ones (0.68 nm/°C). This 80% lower deflection is also seen in the transmission ratio mirror deflection : actuator

elongation. In the bending configuration this ratio is 1 : 30, where for the axial placed actuators it is 1 : 100. Meaning, that in terms of actuator efficiency, mirror bending performs better compared to axial deformation. But, in terms of manufacturability and production costs, axial actuators are preferable to bending actuators. Another advantage of the deformable mirror with axial actuators is the correlation between mirror surface and back-plate. By measuring the deformation of the back-plate using for example conductive sensors, the internal ratio of 1 : 100 increases system performance.

5.2 Recommendations

5.2.1 Vacuum compatibility

For all experimental mirrors built, the actuators are heated with resistance coils and cooled via convection. In vacuum, contact less heating could be done with a laser. Small beam collectors on each actuator can improve the heating efficiency. With a dedicated radiative plate cooler, actuation in both directions relative to the environment temperature is possible. Heat transport by radiation is sufficient to transport the few milliwatts that are needed for each actuator. Another possibility is conductive heat transport using thermal straps with a low stiffness.

In the experimental mirrors, the actuators are connected to the mirror with epoxy. A vacuum compatible alternative is optical contact bonding (ansprengen). This is a glueless process whereby two closely conformal surfaces are joined together, being held by intermolecular forces.

5.2.2 Thermal sensitivity

Making the existing EUV mirrors adaptive using actuators, increases the sensitivity to temperature variations. For example, the shape of a mirror with bending moment actuators is dependent on the temperature. So it is recommended to tune the temperature at glue-curing to the temperature at operation. A deformable mirror with axial actuators is made less sensitive by choosing the same material for both mirror and back plate. The thermal sensitivity and actuator stroke can be tuned by selecting actuator materials other than aluminum.

APPENDIX A

Material properties

Quite some effort is done [18, 30, 36, 65] for a correct measurement of the thermal expansion of ultra low expansion glass (ULE[®]). The thermal expansion coefficient of ULE [20, 75] around its zero crossing temperature (ZCT) is approximated by a linear temperature dependence [43]:

$$\alpha_{\text{ULE}}(T) = a(T - ZCT) \quad (\text{A.1})$$

with $a = 1.5 \cdot 10^{-9} 1/\text{K}^2$. After integrating $dL = \alpha_{\text{ULE}}(T)l_0dT$, the relative elongation reads:

$$\frac{\Delta l}{l_0} = \frac{a}{2}(T - ZCT)^2 - \frac{a}{2}(ZCT - T_{\text{ref}})^2 \quad (\text{A.2})$$

with reference temperature T_{ref} . In figure A.1 the relative elongation is given for different zero crossing temperatures. For all finite element calculations presented in this thesis a constant thermal expansion of

$$\alpha_{\text{ULE}} = 30 \times 10^{-9} 1/\text{K} \quad (\text{A.3})$$

is used, based on the Corning specifications [5]. This value is a guaranteed maximum within a temperature range of 5 °C to 35 °C with a 95% confidence level. Table A.1 gives the properties of a variety of materials used in this thesis.

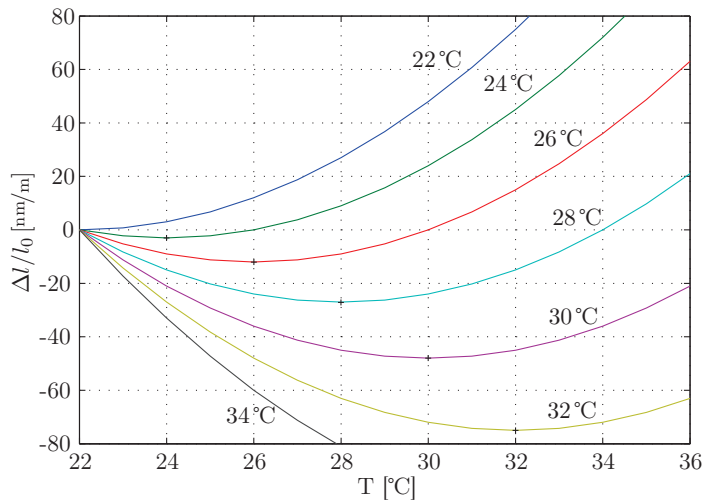


Figure A.1 / Relative elongation of ULE as function of ambient temperature for different zero crossing temperatures at reference temperature $T_{\text{ref}} = 22^\circ\text{C}$.

APPENDIX B

Joule heating

To heat the actuators, an experimental USB-powered stabilized voltage source is designed. Stabilization with various loads is done with a linear voltage regulator LM317. Using the digital I/O ports on the commercial USB-TEMP of Measurement Computing [2], several voltages are selectable: 1.25 (DIO1), 1.8 (DIO2), 2.0 (DIO3), 2.5 (DIO4) and 3.0 V (all off). The circuit's on/off state is switched with a high power transistor BD139 (DIO0). Since the USB-TEMP is also used for actuator temperature measurement, synchronization between joule heating and actuator temperature measurement is obtained using a single Matlab[®] script. Drawback of this approach is the availability of only a few discrete voltages to drive the actuators. Also the USB 2.0 current limit of 500 mA in combination with a load resistance of $13.8\ \Omega$ gives that only one actuator can be driven simultaneously. Measured voltages of the realized experimental source are 1.33, 1.84, 2.07, 2.48 and 3.0 V. Deviation to the theoretical values are caused by the 5% tolerance in resistors used and the voltage drop over the BC547 transistors.

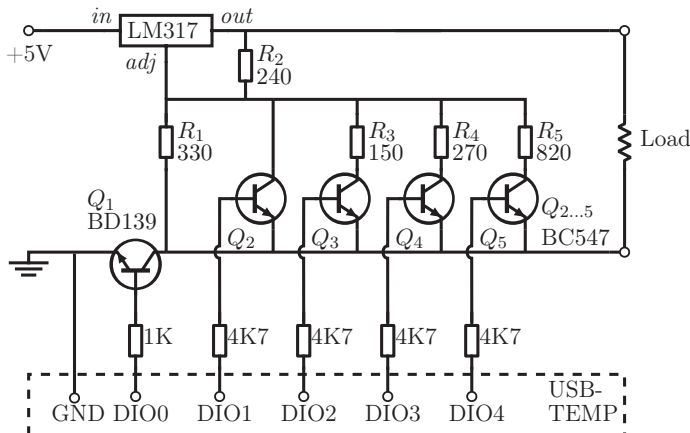


Figure B.1 / Electrical scheme used for joule heating.

To drive 19 actuators simultaneously, the above described circuit is adapted. The

voltage at the adjustment pin of the LM317 is set by a pulse width modulated value (PWM). To stabilize and tune that value, a low pass filter in combination with an op-amp is used, so that voltage adjustment between -1.25 and 0 V is obtained. Now, the voltage over the load is set between 0 and 1.25 V. For one channel, the circuit is shown in figure B.2, where on the left side the inputs, in the top the LM317 and in the middle the op-amp are visible. The resistor values around the non-inverting op-amp are chosen for a gain of 1 and a voltage divider at the $+$ input of 0.14. The combination with the $47\mu\text{F}$ capacitor gives an low-pass cut-off frequency of 0.057Hz , so the characteristic time is $\tau = 2.8\text{s}$. The reference voltage at the $-$ input of the op-amp is set by a $5\text{k}\Omega$ variable resistor.

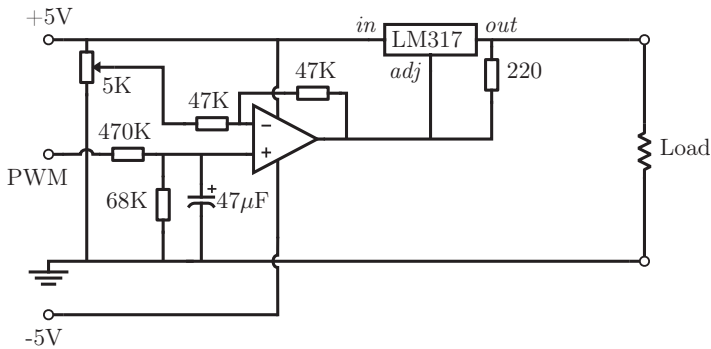


Figure B.2 / One channel out of the 19, to set a load voltage using pulse width modulation.



Figure B.3 / Electronics for 19 channel joule heating.

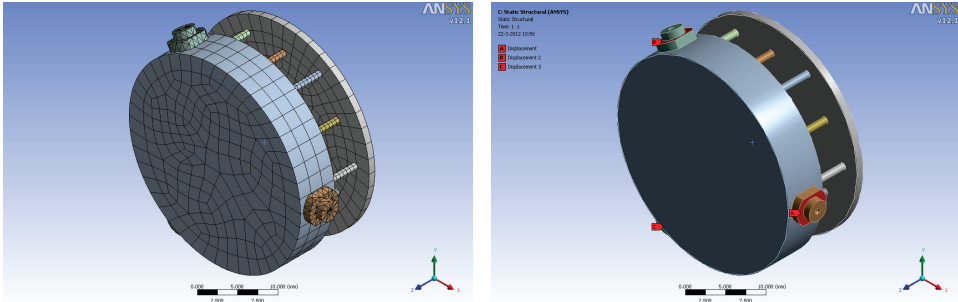
Finite element analysis using ANSYS

The Finite Element Analyzes (FEA) in this thesis are done with Ansys® 12.1, using both structural and (transient) thermal models. Material properties used are given in appendix A. The surface deflection is calculated with the static structural solver with either measured actuator temperatures as input or material temperatures from a transient thermal solution. Surface deflections are displayed and calculated using user defined surfaces and/or paths. The data is also exported to an ASCII text file to enable further processing with Matlab®.

The geometry is designed in Unigraphics and imported into Ansys via Workbench. Discretization is done by the standard finite element method (mesh), as shown in figure C.1(a). Inside a static structural analysis, the rigid body motions are constrained by defining six zero displacements: two at each mirror fixation pin. These are shown in figure C.1(b).

The solution is displayed on a user defined surface as shown in figure C.2(a) or on a path (Fig. C.2(b)).

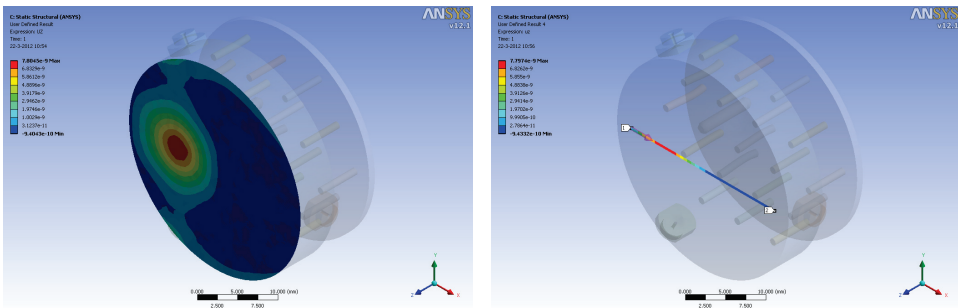
In the static and transient thermal analyzes, the convection on the different bodies is defined using a lookup table. Here the convection coefficient is set for a range of temperatures: between 22°C and 42°C, where the default initial temperature of 22°C is used. Values are calculated using the equations given in sections 2.3.5 and 3.2.1.



(a) discretization

(b) boundary conditions

Figure C.1 / FEA of the mirror with 19 actuators. In (a) the discretization of the imported geometry. In (b) the suppression of the six rigid body motions using two zero displacements on each mirror fixation pin.



(a) user defined surface

(b) user defined path

Figure C.2 / FEA of the mirror with 19 actuators. In (a) is the solution displayed on a user defined surface. In (b) the solution is shown on a path.

Bibliography

- [1] International technology roadmap for semiconductors. <http://www.itrs.net/>.
- [2] Measurement computing. <http://www.mccdaq.com/>.
- [3] Asml press release.
http://www.asml.com/doclib/press/misc/asml_20080404_CB_notprintable.pdf.
- [4] Thermocouple emf values.
http://www.thermocouple.co.uk/main_literature_download.htm.
- [5] Corning ultra low expansion glass (7972) information.
www.corning.com/specialtymaterials/products_capabilities/ULE.aspx.
- [6] Pi ceramic, the piezo ceramic division of physik instrumente (pi).
<http://www.piceramic.com>.
- [7] Boston micromachines.
http://www.bostonmicromachines.com/production_products.htm.
- [8] Iris ao. <http://www.irisao.com/products.html>.
- [9] Aplao adaptive mirrors. http://www.alpao.fr/products_deformable_mirrors.html.
- [10] Flexible optical b.v. (okotech). <http://www.okotech.com/mirrors>.
- [11] Cilas adaptive mirrors. <http://www.cilas.com/adaptative-mirrors.htm>.
- [12] Xinetics adaptive mirrors, part of the northrop grumman group.
http://www.as.northropgrumman.com/products/xinetics_deformable_mirror.
- [13] Materials for use in vacuum.
<http://www.ece.ualberta.ca/schmaus/vacf/vacmat.html>.
- [14] Outgassing data for selecting spacecraft materials. <http://outgassing.nasa.gov/>.
- [15] M. Abramowitz and I. A. Stegun. *Handbook of Mathematical Functions*. Dover Publications, 1965.
- [16] C. Atkins, H. Wang, P. Doel, D. Brooks, S. Thompson, C. Feldman, R. Willingale, T. Button, D. R. Sanmartin, D. Zhang, A. James, C. Theobald, G. Willis, A. D. Smith, R. Hudec and L. Pina. Active x-ray optics for the next generation of x-ray telescopes. In *EUUV and X-Ray Optics: Synergy between Laboratory and Space*, volume 7360, pages 736008–10, Prague, Czech Republic, May 2009. SPIE.

- [17] H. W. Babcock. The possibility of compensating astronomical seeing. *Publications of the Astronomical Society of the Pacific*, 65:229–236, Oct. 1953.
- [18] V. G. Badami. Ultrahigh-accuracy measurement of the coefficient of thermal expansion for ultralow-expansion materials. In *Proceedings of SPIE*, volume 4688, pages 469–480. SPIE, 2002.
- [19] V. Bakshi. *EUV lithography*. SPIE Press, 2009.
- [20] N. P. Bansal and R. H. Doremus. *Handbook of glass properties*. Academic Press, 1986.
- [21] G. Bianucci, G. L. Cassol, J. Kools, M. Prea, G. Salmaso, G. Valsecchi, F. E. Zocchi, D. Bolshukhin, M. Schurmann, G. Schriever, A. Mader and P. Zink. Design and fabrication considerations of EUVL collectors for HVM. In F. M. Schellenberg and B. M. La Fontaine, editors, *Alternative Lithographic Technologies*, volume 7271, pages 72710C–9, San Jose, CA, USA, Mar. 2009. SPIE.
- [22] D. C. Brandt, I. V. Fomenkov, A. I. Ershov, W. N. Partlo, D. W. Myers, R. L. Sandstrom, B. M. La Fontaine, M. J. Lercel, A. N. Bykanov, N. R. Böwering, G. O. Vaschenko, O. V. Khodykin, S. N. Srivastava, I. Ahmad, C. Rajyaguru, P. Das, V. B. Fleurov, K. Zhang, D. J. Golich, S. De Dea, R. R. Hou, W. J. Dunstan, C. J. Wittak, P. Baumgart, T. Ishihara, R. D. Simmons, R. N. Jacques and R. A. Bergstedt. LPP source system development for HVM. In *Proceedings of SPIE*, pages 79691H–79691H–8, San Jose, California, USA, 2011.
- [23] P. R. N. Childs. *Practical temperature measurement*. Butterworth-Heinemann, Oxford, Oct. 2001.
- [24] B. Crepy. Last progress concerning the design of the piezo stack m4 adaptive unit of the E-ELT. In *Adaptive Optics Systems II*, volume 7736, page 77362F, San Diego, California, USA, June 2010. SPIE.
- [25] M. A. Ealey and M. A. Ealey. Actuators: design fundamentals, key performance specifications, and parametric trades. In *Active and Adaptive Optical Components*, volume 1543, pages 346–362, San Diego, CA, USA, Jan. 1992. SPIE.
- [26] M. A. Ealey, J. A. Wellman and M. A. Ealey. Deformable mirrors: design fundamentals, key performance specifications, and parametric trades. In *Active and Adaptive Optical Components*, volume 1543, pages 36–51, San Diego, CA, USA, Jan. 1992. SPIE.
- [27] J. Gaffard, R. Ravelet, C. Boyer and M. A. Ealey. X-ray adaptive mirror: principle and state of the art. In *Active and Adaptive Optical Components and Systems II*, volume 1920, pages 121–135, Albuquerque, NM, USA, 1993. SPIE.
- [28] R. G. Gilbertson and J. D. Busch. A survey of micro-actuator technologies for future spacecraft missions. *Journal of The British Interplanetary Society*, 49:129–138, 1996.

- [29] R. Gronheid, T. R. Younkin, M. J. Leeson, C. Fonseca, J. S. Hooge, K. Nafus, J. J. Biafore and M. D. Smith. EUV secondary electron blur at the 22nm half pitch node. In *Proceedings of SPIE*, pages 796904–796904–11, San Jose, California, USA, 2011.
- [30] H. E. Hagy, R. A. Paquin and D. Vukobratovich. Review of measurement systems for evaluating thermal expansion homogeneity of corning code 7971 ULE[registered sign]. In *Optomechanics and Dimensional Stability*, volume 1533, pages 198–211, San Diego, CA, USA, Dec. 1991. SPIE.
- [31] B. Halliday. An introduction to materials for use in vacuum. *Vacuum*, 37(8-9):583–585, 1987.
- [32] R. Hamelinck. *Adaptive deformable mirror: based on electromagnetic actuators*. PhD thesis, Technische Universiteit Eindhoven, Eindhoven, The Netherlands, 2010.
- [33] R. Hamelinck, R. Ellenbroek, N. Rosielle, M. Steinbuch, M. Verhaegen and N. Doelman. Validation of a new adaptive deformable mirror concept. *Proceedings of SPIE*, 7015(1):70150Q–70150Q–12, July 2008.
- [34] J. W. Hardy. *Adaptive Optics for Astronomical Telescopes*. Oxford University Press, US, 1998.
- [35] M. Hart. Recent advances in astronomical adaptive optics. *Applied Optics*, 49(16):D17–D29, June 2010.
- [36] K. E. Hrdina. Characterization and characteristics of a ULE glass tailored for EUVL needs. In *Proceedings of SPIE*, volume 4688, pages 454–461. SPIE, 2002.
- [37] W. S. Janna. *Engineering heat transfer*. CRC Press, 2000.
- [38] S. Jeong. Actinic defect counting statistics over 1-cm² area of EUVL mask blank. In *Proceedings of SPIE*, volume 3997, pages 431–440, Santa Clara, CA, USA, 2000.
- [39] S. Kitamoto, T. Ogita, T. Shibata, E. Takenaka, N. Gotoh, Y. Shishido, D. Takei, M. Yoshida, M. Morii and H. Murakami. EUV-imaging experiments of a normal incident telescope with an adaptive optics system. In *Proceedings of SPIE*, pages 70153Y–70153Y–8, Marseille, France, 2008.
- [40] S. Kitamoto, T. Shibata, E. Takenaka, M. Yoshida, H. Murakami, Y. Shishido, N. Gotoh, K. Nagasaki, D. Takei and M. Morii. EUV imaging experiment of an adaptive optics telescope. In *Proceedings of SPIE*, pages 74371I–74371I–8, San Diego, CA, USA, 2009.
- [41] S. Kitamoto, H. Takano, H. Saitoh, N. Yamamoto, T. Kohmura, K. Suga, H. Sekiguchi and R. L. Engelstad. Development of an ultra high-precision x-ray telescope with an adaptive optics system. In *Emerging Lithographic Technologies VII*, volume 5037, pages 294–301, Santa Clara, CA, USA, June 2003. SPIE.

- [42] S. Kitamoto, N. Yamamoto, T. Kohmura, K. Suga, H. Sekiguchi, J. Sato, K. Sudo, T. Watanabe, Y. Ohkubo, A. Sekiguchi, M. Tsujimoto, O. Citterio and S. L. O'Dell. Adaptive x-ray optics with a deformable mirror. In *Optics for EUV, X-Ray, and Gamma-Ray Astronomy II*, volume 5900, pages 590019–8, San Diego, CA, USA, 2005. SPIE.
- [43] T. Legero, T. Kessler and U. Sterr. Tuning the thermal expansion properties of optical reference cavities with fused silica mirrors. *Journal of the Optical Society of America B*, 27(5):914–919, May 2010.
- [44] H. J. Levinson. *Principles of lithography*. SPIE Press, Apr. 2005.
- [45] Y. Li, K. Ota and K. Murakami. Thermal and structural deformation and its impact on optical performance of projection optics for extreme ultraviolet lithography. *Journal of Vacuum Science & Technology B: Microelectronics and Nanometer Structures*, 21(1):127–129, Jan. 2003.
- [46] V. P. Linnick. On the possibility of reducing the influence of atmospheric seeing on the image quality of stars (in russian). *Optics and Spectroscopy*, 3:401–402, 1957.
- [47] M. Lowisch, P. Kuerz, H. Mann, O. Natt and B. Thuring. Optics for EUVL production. In B. M. La Fontaine, editor, *Extreme Ultraviolet (EUV) Lithography*, volume 7636, pages 763603–11, San Jose, California, USA, Mar. 2010. SPIE.
- [48] C. Mack. *Fundamental principles of optical lithography*. Wiley-Interscience, 2007.
- [49] K. Matsunaga, G. Shiraishi, J. J. Santillan, K. Kaneyama, H. Oizumi and T. Itani. Development status of EUV resist materials and processing at selete. In *Proceedings of SPIE*, pages 796905–796905–9, San Jose, California, USA, 2011.
- [50] C. E. Max and E. Barton. The scientific impact of reaching the diffraction limit with ELTs. In B. L. Ellerbroek, M. Hart, N. Hubin and P. L. Wizinowich, editors, *Adaptive Optics Systems II*, volume 7736, pages 773602–7, San Diego, California, USA, July 2010. SPIE.
- [51] H. Meiling, V. Banine, P. Kuerz, B. D. Blum, G. J. Heerens, N. Harned and R. L. Engelstad. The EUV program at ASML: an update. In *Emerging Lithographic Technologies VII*, volume 5037, pages 24–35, Santa Clara, CA, USA, June 2003. SPIE.
- [52] L. Michalski and K. Eckersdorf. *Temperature measurement*. John Wiley and Sons, 2001.
- [53] M. F. Modest. *Radiative heat transfer*. Academic Press, 2003.
- [54] G. Moore. Cramming more components onto integrated circuits. *Electronics*, 38(8):114–117, Apr. 1965.
- [55] G. E. Moore. Lithography and the future of moore's law. *Proceedings of SPIE*, 2438(1):2–17, June 1995.

- [56] J. Mulkens, J. de Klerk, M. Leenders, F. de Jong, J. W. Cromwijk, H. J. Levinson and M. V. Dusa. Latest developments on immersion exposure systems. In *Optical Microlithography XXI*, volume 6924, pages 69241P–12, San Jose, CA, USA, Mar. 2008. SPIE.
- [57] H. Murakami, S. Kitamoto, E. Takenaka, T. Shibata, M. Yoshida, K. Higashi and D. Takei. Imaging experiment of an adaptive optics with a normal-incident EUV telescope. In *Proceedings of SPIE*, pages 78030E–78030E–6, San Diego, California, USA, 2010.
- [58] P. P. Naulleau, C. N. Anderson, L.-M. Baclea-an, P. Denham, S. George, K. A. Goldberg, G. Jones, B. McClinton, R. Miyakawa, S. Rekawa and N. Smith. Critical challenges for euv resist materials. In *Proceedings of SPIE*, volume 7972, page 797202. SPIE, 2011.
- [59] A. Norton, J. W. Evans, D. Gavel, D. Dillon, D. Palmer, B. Macintosh, K. Morzinski and S. Cornelissen. Preliminary characterization of boston micromachines’ 4096-actuator deformable mirror. In *Proceedings of SPIE*, pages 72090I–72090I–7. SPIE, 2009.
- [60] S. K. Ravensbergen, R. F. M. M. Hamelinck, P. C. J. N. Rosielle and Steinbuch. Deformable mirrors: design fundamentals for force actuation of continuous facesheets. In *Advanced Wavefront Control: Methods, Devices, and Applications VII*, volume 7466, pages 74660G–8, San Diego, CA, USA, 2009. SPIE.
- [61] P. B. Reid, S. S. Murray, S. Trolier-McKinstry, M. Freeman, M. Juda, W. Podgorski, B. Ramsey, D. Schwartz, M. J. L. Turner and K. A. Flanagan. Development of adjustable grazing incidence optics for Generation-X. In *Space Telescopes and Instrumentation 2008: Ultraviolet to Gamma Ray*, volume 7011, pages 70110V–10, Marseille, France, July 2008. SPIE.
- [62] J. Roberts, A. H. Bouchez, R. S. Burruss, R. G. Dekany, S. R. Guiwits and M. Troy. Optical characterization of the PALM-3000 3388-actuator deformable mirror. In *Proceedings of SPIE*, pages 77362E–77362E–8, 2010.
- [63] F. Roddier. *Adaptive Optics in Astronomy*. Cambridge University Press, 1999.
- [64] P. C. J. N. Rosielle. Mirror system and lithographic projection device comprising such a mirror system, May 2010.
- [65] R. Sabia, M. J. Edwards, R. VanBrocklin, B. Wells, E. Atad-Ettingui, J. Antebi and D. Lemke. Corning 7972 ULE material for segmented and large monolithic mirror blanks. In *Optomechanical Technologies for Astronomy*, volume 6273, pages 627302–8, Orlando, FL, USA, June 2006. SPIE.
- [66] D. H. Sanders. *Computers in business: an introduction*. McGraw-Hill, 1979.
- [67] J. Siquin, J. Lurcon, C. Guillemard, N. Hubin, C. E. Max and P. L. Wizinowich. Deformable mirror technologies for astronomy at CILAS. In *Adaptive Optics Systems*, volume 7015, pages 70150O–12, Marseille, France, July 2008. SPIE.

- [68] P. A. Spence, S. E. Gianoulakis, C. D. Moen, M. P. Kanouff, A. Fisher and A. K. Ray-Chaudhuri. System performance modeling of extreme ultraviolet lithographic thermal issues. In *Papers from the 43rd international conference on electron, ion, and photon beam technology and nanofabrication*, volume 17, pages 3034–3038, Marco Island, Florida (USA), Nov. 1999. AVS.
- [69] S. Tibbitts. High-output paraffin linear motors: utilization in adaptive systems. In M. A. Ealey, editor, *Active and Adaptive Optical Components*, volume 1543, pages 388–399, San Diego, CA, USA, Jan. 1992. SPIE.
- [70] S. Timoshenko and S. Woinowsky-Krieger. *Theory of Plates and Shells*. McGraw-Hill, 1959.
- [71] A. C. Tribble. *Fundamentals of contamination control*. SPIE Press, 2000.
- [72] R. K. Tyson. *Adaptive Optics Engineering Handbook*. CRC, 2000.
- [73] C. Wagner, J. Bacelar, N. Harned, E. Loopstra, S. Hendriks, I. de Jong, P. Kuerz, L. Levasier, M. van de Kerkhof, M. Lowisch, H. Meiling, D. Ockwell, R. Peeters, E. van Setten, J. Stoeldraijer, S. Young, J. Zimmerman and R. Kool. EUV lithography at chipmakers has started: performance validation of ASML’s NXE:3100. In *Proceedings of SPIE*, pages 79691F–79691F–12, San Jose, California, USA, 2011.
- [74] C. Wagner and N. Harned. EUV lithography: Lithography gets extreme. *Nat Photon*, 4(1):24–26, Jan. 2010.
- [75] M. J. Weber. *Handbook of optical materials*. CRC Press, 2003.
- [76] M. Yoshioka, Y. Teramoto, J. Jonkers, M. C. Schürmann, R. Apetz, V. Kilian and M. Corthout. Tin DPP source collector module (SoCoMo) ready for integration into beta scanner. In *Proceedings of SPIE*, pages 79691G–79691G–9, San Jose, California, USA, 2011.

Nomenclature

| Symbol | Description | Unit |
|---------------|--|--------------------|
| A | cross section | m^2 |
| c | stiffness | N/m |
| c_p | specific heat capacity | $J/(kg\ K)$ |
| D | diameter | m |
| \mathcal{D} | flexural rigidity | Nm |
| E | Young's modulus (elastic modulus) | N/m^2 |
| F | force | N |
| g | gravitational acceleration | m/s^2 |
| f | frequency | Hz |
| h | thickness | m |
| \tilde{h} | convective heat transfer coefficient | $W/(m^2\ K)$ |
| I | second moment of inertia | m^4 |
| i | current | A |
| k | thermal conductivity | $W/(m\ K)$ |
| k_1 | lithographic scaling factor | - |
| l | length | m |
| M | moment | Nm |
| m | mass | kg |
| n | number | - |
| p | pitch | m |
| P | power | W |
| q | heat flow rate | W |
| q'' | heat flow rate per area | W/m^2 |
| q''' | heat flow rate per volume | W/m^3 |
| R | resistance | Ω |
| r | distance between actuator and mirror center line | m |
| T | temperature | $^{\circ}C$ or K |
| t | time | s |
| U | voltage | V |
| u | measurement signal | V |

| Symbol | Description | Unit |
|------------------|--|------------------------------------|
| V | volume | m^3 |
| w | width | m |
| x, y, z | cartesian coordinate system | m |
| | | |
| Greek | Description | Unit |
| α | linear coefficient of thermal expansion | $\mu\text{m}/(\text{m K})$ |
| Δ | difference in e.g. temperature or displacement | |
| δ | mirror deflection | m |
| ϵ | emittance | - |
| η | Actuator coupling | - |
| κ | foundation modulus | N/m^3 |
| λ | wavelength | m |
| ν | Poisson's ratio | - |
| ν_k | kinematic viscosity | m^2/s |
| ξ | characteristic length | m |
| ρ | density | kg/m^3 |
| ϱ | electrical resistivity, specific electrical resistance | Ωm |
| σ | Stefan-Boltzmann constant 5.67×10^{-8} | $\text{W}/(\text{m}^2 \text{K}^4)$ |
| τ | characteristic time constant | s |
| | | |
| Subscript | Description | |
| A | actuator | |
| B | back-plate | |
| IA | inter-actuator | |
| M | mirror | |
| max | maximal | |
| opt | optimal | |
| P | post | |
| 0 | initial value or value at $t = 0$ | |
| ∞ | ambient or value at $t = \infty$ | |

Glossary

- ADC** analog-to-digital converter
- AO** Adaptive optics, a technology to improve the performance of optical systems by compensating wavefront distortions.
- CD** Critical Dimension
- CJC** cold junction compensation, compensation for thermocouple reference junction temperature variations.
- CST** Control Systems Technology Group, Faculty of Mechanical Engineering, TU/e
- CTE** coefficient of thermal expansion
- DAC** digital-to-analog converter
- depth of focus** The amount of image defocus which corresponds to being out of focus by one-quarter wave. This means that the optical path difference between the real wavefront leaving the exit pupil at its outer periphery and a reference wavefront centered at the nominal image plane is one-quarter of the wavelength of light.
- DM** Deformable Mirror is a mirror with at least one degree of freedom that can adapt its surface.
- EMF** electromotive force
- EMI** electromagnetic interference
- EPC** Equipment & Prototype Center at the TU/e
- EUV** Extreme Ultraviolet: 121 nm \rightarrow 10 nm (10.2 \rightarrow 124 eV)
- Soft X-ray** 10 nm \rightarrow 100 pm (0.124 \rightarrow 12.4 keV)
- Hard X-ray** 100 pm \rightarrow 10 pm (12 \rightarrow 120 keV)
- FEA** finite element analysis
- GND** ground (in electrical circuit)
- IC** integrated circuit
- Matlab®** mathematical software, registered trademark of The MathWorks Inc.
- NA** numerical aperture of an optical component is a measure of its ability to gather light and resolvable detail.
- NX** computer aided design and manufacturing software, trademark of Siemens Product Lifecycle Management Software (formerly UGS)

PCB printed circuit board

PRT platinum resistance thermometer: platinum temperature sensor whose resistance varies with temperature.

Pt100 A platinum temperature sensor where the resistance at 0°C is 100 Ω.

PV Peak to valley

RMS root mean square

Spatial frequency Resolution of a deformable mirror, in most cases the number of actuators across the diameter.

Thermocouple Any pair of dissimilar electrically conducting materials coupled at an interface

Thermoelectric junction Electric interface between dissimilar electric conductors.

TU Delft Technische Universiteit Delft

TU/e Technische Universiteit Eindhoven

ULE[®] Ultra-Low Expansion (ULE[®]) glass, registered trademark of Corning Inc.

USB universal serial bus

WFS A Wave Front Sensor measures the wave front distortions of a light beam.

Zerodur[®] low-expansion ceramic glass, registered trademark of Schott AG.

Dankwoord

Aan wat in het begin leek op een onoverzienbare hoeveelheid tijd, is dan nu toch echt een einde gekomen. Nu kan ik deze geweldige vier jaar af sluiten met dit proefschrift. Tijdens deze tijd heb ik mogen ontdekken wat het is om *echt* onderzoek te doen en heb ik veel kunnen leren, waarvoor ik zeer dankbaar ben. Graag wil ik een aantal mensen speciaal bedanken die mij hebben begeleid en ondersteund om tot dit resultaat te komen.

Nick Rosielle. Bedankt dat ik van jou het prachtige vak construeren mocht leren! Jouw onuitputtelijke bron van nieuwe ideeën en doorzettingsvermogen blijven mij verbazen. Ik vind het een eer om met jouw begeleiding alle project stadia doorlopen te hebben, beginnende bij euforie [66].

Maarten Steinbuch. Een betere promotor kan een promovendus zich niet wensen! Altijd enthousiast lukt het jou om onderzoek naar een volgende fase te sturen, en wanneer het mij alleen niet lukte, dan zette je meteen de nodige middelen in.

Graag wil ik de betrokken mensen bij de Gemeenschappelijk Technische Dienst bedanken voor de realisatie van de spiegels: Jurgen Bulsink, Meindert Janszen, Dave Bax, Harrie de Laat en Erwin Dekkers.

Ook wil ik de mensen bij TNO bedanken voor de hulp en de middelen die ik kreeg bij mijn experimenten (o.a. figuren 2.19, 2.25, 3.4, 3.7, 3.10, 4.9, 4.17): Mariët, Denise, Andries, Guido en Guus. Bob, bedankt voor het vervaardigen en aanpassen van de spiegels (figuren 2.16, 3.1).

Hierbij wil ik prof. Rob Munnig Schmidt (TU Delft), prof. Paul Urbach (TU Delft) en Marc Geers (TU/e) bedanken voor hun inspanningen om dit proefschrift van nuttige feedback te voorzien.

Dit project was niet mogelijk geweest zonder het Pieken in de Delta programma. Graag wil ik alle leden van het projectteam bedanken en in het bijzonder Niek Doelman (TNO), Anton van Dijsseldonk (ASML), Wim de Boei (ASML) en Bernhard Kneer (Zeiss). A special thanks to the other PhD students of this great project: Alessandro Polo, Rudolf

Saathof and Aleksandar Haber.

Ook vanuit de TU/e heb ik veel steun mogen ervaren, hierbij wil ik graag Marc van Maris en Bert Steegemans bedanken. En ook de mensen van het Innovation lab: Ronald van den Oetelaar, Remco Hutten, Boukje Rongen en Steef Blok. En natuurlijk de dames van het DCT secretariaat: Petra, Geertje en Lia!

Verder wil ik mijn labgenoten en collega's bedanken voor alle plezier, enthousiasme en goede (al dan niet relevante) discussies: David, Geert-Jan, Ron, Kees, Raimondo, Thijs, Roger, Rens, Linda en Lenino.

Mijn familie: Pa en ma, dank voor alle ruimte en ondersteuning die jullie mij hebben gegeven. Ik vind het super hoeveel techniek er in één familie samenkomt: Lisanne we zijn al bijna collega's, Cornee je bent zowat klaar met de studie die ik te theoretisch vond en Timo wie had ooit gedacht dat we tegelijk zouden studeren & werken bij dezelfde faculteit.

Nard: bedankt voor alles, maar vooral voor alle ttttjes!

Susan. Ja lieveling, deze laatste zinnen zijn voor jou! Dank voor al je liefde, steun, begrip en geduld die je me hebt gegeven; vooral in die momenten waarbij ik fysiek wel bij jou was, maar met mijn hoofd nog steeds bij dit onderzoek.

Simon Ravensbergen

Tilburg, maart 2012

Curriculum Vitae

Simon Ravensbergen was born in Leiden, the Netherlands, on May 24, 1983.

1995 – 1999 Secondary school, Europäische Schule München, Germany.

1999 – 2001 Secondary school, Scholengemeenschap WereDi, Valkenswaard.

2002 – 2007 Mechanical Engineering at Technische Universiteit Eindhoven.
Graduated within the Constructions & Mechanisms group.

2005 – 2007 Master thesis project at Philips Apptech, Eindhoven.

2008 – 2012 Ph.D. candidate at Technische Universiteit Eindhoven, Department of
Mechanical Engineering, Control Systems Technology group.